

Ph.D. Thesis

**Enhancement and Classification of
Cardiac SPECT Images using Pixel
Intensity Based Features**

Submitted to

COCHIN UNIVERSITY OF SCIENCE AND TECHNOLOGY

for the award of the degree of

Doctor of Philosophy

by

NEETHU M. SASI

Under the guidance of

Dr. Jayasree V. K.

Research Guide

Department of Electronics
Model Engineering College

Kochi - 682 021, India

August 2017

IMAGE PROCESSING

**Enhancement and Classification of Cardiac SPECT
Images using Pixel Intensity Based Features**

Thesis submitted to the Cochin University of Science and
Technology for the award of the degree of Doctor of
Philosophy under the Faculty of Engineering

By

NEETHU M. SASI

Supervising Guide

Dr. JAYASREE V. K.

**Department of Electronics
Govt. Model Engineering College, Thrikkakkara
Kochi-682021, Kerala, India.
August 2017**

CERTIFICATE

Certified that this thesis entitled "**Enhancement and Classification of Cardiac SPECT Images using Pixel Intensity Based Features**" is a bonafide record of the research work done by **Ms. Neethu M. Sasi** under my supervision in the Department of Electronics, Govt. Model Engineering College, Kochi, India. The contents of this thesis have not been submitted and will not be submitted to any other University or Institute for the award of any degree/diploma.

I further certify that the corrections and modifications suggested by the audience during pre-synopsis seminar and recommended by the Doctoral committee of Neethu M. Sasi are incorporated in this thesis.

Kochi-21
August 2017

Dr. Jayasree V. K
(Supervising Guide)
Professor, Principal
College of Engineering
Adoor

DECLARATION

I hereby declare that the work presented in the thesis entitled **“Enhancement and Classification of Cardiac SPECT Images using Pixel Intensity Based Features”** is based on the original research work carried out by me under the supervision and guidance of Dr. Jayasree V. K., Professor, Principal, College of Engineering, Adoor, Kerala, India for the award of degree of Doctor of Philosophy with Cochin University of Science and Technology. I further declare that the contents of this thesis in full or in parts have not been submitted to any other University or Institute for the award any degree or diploma.

Kochi-21
August 2017

Neethu M. Sasi

To my family...

Acknowledgement

Thanks to The Almighty for bestowing upon me, the blessings and strength to complete this research work.

I would express here my heartfelt gratitude to Dr. Jayasree V. K., the supervising guide, for her support, motivation and guidance throughout this research work.

Extending my sincere thankfulness to Dr. V. P. Devassia, Principal, Model Engineering College for providing all facilities for this research. I am extremely thankful to Dr. Mini M. G., Principal, College of Engineering Cherthala for her valuable suggestions and advices.

I thank Dr. Vinu Thomas for the time he had spent for fruitful discussions on the subject.

My sincere thanks to the former and current Principals of Adi Shankara Institute of Engineering and Technology, Dr. S. G. Iyer and Dr. Neelakantan P. C. for granting me leave for completing my research and being an inspiration in this endeavor.

I don't have words to thank my husband, Rajesh for his patience, support and affection in my life. His suggestions and the ideas we shared in the duration of this work always helped me to face those occasional challenging times. I am thankful to my children, Arunima and Abhiram for their understanding. The constant prayers of my parents, their love and their belief in me have always been a pillar of my strength. They have been waiting for this day to happen more than me. I remember the great support extended by my in-laws. Thanks to my sister for her help in pressing times.

I gratefully acknowledge my co-research fellows, all teaching, non-teaching and technical staff of Model Engineering College for their support.

The time, assistance and support of nuclear medicine practitioners Dr. Kuruvila Varkey (Bharat Scan Centre, Kottayam) and Dr. Shamily

George (Medical Trust Hospital, Kochi) deserves a special mention as it had an important bearing in the progress and completion of this work.

The positive influence of my colleagues in ASIET, Kalady and all other well-wishers from my life are fondly acknowledged here.

Neethu M. Sasi

Abstract

Maladies directly related to human heart condition have emerged to be the leading global cause of health related human deaths. The mortality rate due to heart functioning can be reduced through its timely diagnosis and accurate assessment. Single photon emission computed tomography perfusion images provide a reliable tool for the assessment of heart disorders. Computer aided methods for better visualization and interpretation of single photon emission computed tomography images have already been used and proven to be potentially helpful for increasing the clinical use of such imaging technique.

The primary objective of this thesis is to develop enhancement and classification techniques suitable for identifying the tracer content region in single photon emission computed tomography image slices. Image dependent methods were employed to enable an improved outcome. Mitigation of the effects of noise, blur and decreased contrast were addressed while developing enhancement algorithms. Features capable of identifying lower tracer content area were extracted for the purpose of classification.

The performances of the developed methods were evaluated using different works from current literature. The comparison results indicate

that the proposed methods are instrumental in assisting physicians to arrive at a more reliable diagnostic decision.

The images for the study were sourced from Medical trust hospital, Kochi, Kerala, India and image database of case studies published by Spectrum dynamics medical.

The work, though complete in itself, offers a take-off point for further development in its scope and this has been addressed in the end.

Keywords: Blind Deconvolution; Heart Perfusion; Image Quality Index; Morphological Processing; Single Photon Emission Computed Tomography; Structural Similarity Index Measure; Tracer.

CONTENTS

	Page No.
Abstract	i
List of Figures	ix
List of Tables	xv
Abbreviations	xvii
Chapter 1: Introduction	1
1.1 Introduction	2
1.2 Contribution of the thesis	3
1.3 Anatomy of human heart	3
1.4 Cardiac imaging modalities	6
1.4.1 X-ray	6
1.4.2 Echocardiography	7
1.4.3 Computed tomography	9
1.4.4 Cardiac magnetic resonance imaging	10
1.4.5 Nuclear imaging	11
1.4.5.1 Single photon emission computed tomography	12
1.4.5.2 Positron emission tomography	13
1.5 Organization of the thesis	16
Chapter 2: Literature review and problem formulation	19
2.1 Introduction	20
2.2 Cardiac SPECT imaging	20

2.2.1 Basic principles	21
2.2.2 Image acquisition	22
2.2.3 Image reconstruction	26
2.2.3.1 Iterative reconstruction method	26
2.2.3.2 Filtered backprojection method	28
2.2.4 Conventional slice display of cardiac SPECT images	28
2.3 Literature review and research potential in the field of enhancement of cardiac SPECT images	32
2.4 Literature review and research potential in the field of classification of cardiac SPECT images	34
2.5 Motivation	35
2.6 Scope and relevance	36
2.7 Database used	38
Chapter 3: Enhancement of contrast in cardiac SPECT images	41
3.1 Introduction	42
3.2 Literature survey	43
3.3 Preliminary concepts in morphology	45
3.4 Proposed method	47
3.4.1 Adaptive selection of the size of structuring element	48
3.4.2 Morphological processing	50
3.5 Performance measures	53
3.6 Simulation results	55
3.7 Summary	67

Chapter 4: Enhancement of cardiac SPECT images by deblurring	69
4.1 Introduction	70
4.2 Literature survey	70
4.3 Blur model in SPECT imaging	72
4.4 Deblurring methods	73
4.4.1 Blind deconvolution	73
4.4.2 Lucy Richardson algorithm	74
4.4.3 Least square filtering	75
4.5 Proposed method	76
4.5.1 Prefiltering	77
4.5.2 Maximum likelihood estimation of the PSF	77
4.5.3 Total variation regularization based deconvolution	80
4.6 Simulation results	82
4.7 Summary	94
Chapter 5: Enhancement of cardiac SPECT images by denoising	97
5.1 Introduction	98
5.2 Literature survey	98
5.3 Noise model in SPECT imaging	100
5.4 Proposed method	101
5.4.1 Variance stabilizing transformation	102
5.4.2 De-noising stage	103
5.4.3 Inverse transformation	107
5.5 Simulation results	107

5.6 Summary	116
Chapter 6: Classification	117
6.1 Introduction	118
6.2 Literature survey	119
6.3 Feature extraction	120
6.3.1 Image histogram based feature	121
6.3.1.1 Analysis of different intensity regions	121
6.3.1.2 Segmentation of brighter pixel region	123
6.3.1.3 Extraction of features	125
6.3.2 Gray level co-occurrence matrix based features	125
6.3.3 Intensity variation based feature	126
6.3.4 Fractal based feature	126
6.3.4.1 Fundamental of fractals and fractal dimension	126
6.3.4.2 Extraction of fractal based features	124
6.3.5 Standard deviation of brightness	129
6.4 Features extracted from randomly selected images	130
6.5 Classification algorithm used	137
6.5.1 Feed forward neural network	137
6.6 Experimental setup	138
6.7 Performance measures	139
6.8 Results and discussions	141
6.9 Summary	148

Chapter 7: Conclusion and future prospects	149
7.1 Concluding remarks	150
7.2 Proposals for future work	151
References	153
Publication list	187
Curriculum vitae	189

LIST OF FIGURES

Figure	Title	Page No.
1.1	Anatomy of human heart	4
1.2	Left ventricular walls	5
1.3	An example of coronary angiography	7
1.4	A cardiac ultrasound image showing all four chambers of the heart	9
1.5	A cardiac CT angiography	10
1.6	A CMR image	11
1.7	Cardiac SPECT image	13
1.8	Basic principle of ACD	14
1.9	Cardiac PET image	15
2.1	SPECT gamma camera system	23
2.2	Underlying principles of SPECT imaging	24
2.3	Basic elements of a gamma camera head	24
2.4	A parallel-hole collimator attached to scintillation crystal	25
2.5	Schematic illustration of iterative reconstruction algorithm	27
2.6	Standardized planes of cut for reconstructed SPECT slices	29
2.7	Reconstructed SPECT slices	30
2.8	An image slice with abnormal perfusion in the short axis view	31
2.9	An image slice with normal perfusion in the short axis view	31

2.10	Number of cases of heart ailments in different age groups among Indian population	37
3.1	Block diagram showing the basic stages in the proposed method	47
3.2	Steps in determining the size of structuring element	49
3.3	SPECT image slices and binary thresholded image slices	51
3.4	Morphological processing	52
3.5	Cardiac SPECT image slices (low tracer content region) and enhanced slices	56
3.6	Cardiac SPECT image slices (high tracer content region) and the corresponding enhanced slices using the proposed method	56
3.7	An abnormal perfusion SPECT image and SPECT image enhanced using the proposed method	57
3.8	A normal perfusion SPECT image and SPECT image enhanced using the proposed method	58
3.9	Images before and after enhancement using CLAHE, BHEASF and proposed method	63
3.10	Comparison of CI in images enhanced using fixed neighbourhood morphological processing and proposed adaptive neighbourhood method	64
3.11	Comparison of ED between original image and enhanced using fixed neighbourhood morphological processing and proposed adaptive neighbourhood method	65
3.12	Comparison of MSE in images enhanced using fixed neighbourhood morphological processing and proposed adaptive neighbourhood method	66
3.13	Comparison of SSIM in images enhanced using fixed neighbourhood morphological processing and proposed adaptive neighbourhood method	66
4.1	Image blurring model	72

4.2	Block diagram of the proposed method	76
4.3	Estimation of PSF and image	78
4.4	Cardiac SPECT image blurred using a Gaussian PSF with sigma=3 and image using proposed method	83
4.5	Cardiac SPECT image blurred using a Gaussian PSF with sigma=5 and image using proposed method	83
4.6	Cardiac SPECT image blurred using a Gaussian PSF with sigma=7 and image using proposed method	84
4.7	Original image, blurred image and image deblurred using blind deconvolution and proposed method	87
4.8	Performance comparison between proposed method and LR method using ML estimate of PSF in terms of PSNR	90
4.9	Performance comparison between proposed method and LR method using ML estimate of PSF in terms of SSIM	91
4.10	Performance comparison between proposed method and LR method using ML estimate of PSF in terms of BM	91
4.11	Performance comparison between proposed method and LR method using ML estimate of PSF in terms of IEF	92
4.12	Performance comparison between proposed method and least square filtering method using ML estimate of PSF in terms of PSNR	93
4.13	Performance comparison between proposed method and least square filtering method using ML estimate of PSF in terms of SSIM	93
4.14	Performance comparison between proposed method and least square filtering method using ML estimate of PSF in terms of blur metric	94

4.15	Performance comparison between proposed method and least square filtering method using ML estimate of PSF in terms IEF	94
5.1	Steps in the proposed method	102
5.2	Basic steps in the de-noising stage	104
5.3	Flowchart showing the steps for choosing the size of neighborhood	106
5.4	SPECT image slice of an abnormal case with low tracer content	108
5.5	Noisy image and image de-noised using proposed method	109
5.6	Noisy image and de-noised image for a normal cardiac case	109
5.7	MPI Spectrum Dynamics case study image with Poisson noise and the de-noised image using proposed method	110
5.8	Simulated image, noisy image and de-noised image with their image profiles	111
5.9	Comparison between the proposed method and de-noising method using fixed window Wiener filter in Anscombe domain in terms of PSNR	113
5.10	Comparison between the proposed method and de-noising method using fixed window Wiener filter in Anscombe domain in terms of SSIM	113
5.11	Comparison between the proposed method and de-noising method using fixed window Wiener filter in Anscombe domain in terms of IEF	114
5.12	Comparison between the proposed method and de-noising method using fixed window Wiener filter in Anscombe domain in terms of IQI	114
5.13	Edgemap of the original image, noisy image and image denoised using BM3D, wavelet thresholding, Wiener filter and proposed method	115

6.1	A heart slice with A, B and C showing three different regions in the image	122
6.2	Image histogram of regions A, B and C	122
6.3	A slice from the short axis view of a heart with normal perfusion and its segmented images	123
6.4	A slice from the vertical long axis view of a heart with normal perfusion and its segmented images	124
6.5	A slice from the horizontal long axis view of a heart with normal perfusion and its segmented images	124
6.6	A slice from the short axis view of a heart with abnormal perfusion and its segmented images	124
6.7	A slice from the apex region of a normal perfusion heart and its binary thresholded image	128
6.8	A slice from the apex region of an abnormal perfusion heart and its binary thresholded image	128
6.9	Binary thresholded image for the normal perfusion case and the smallest shape that builds up the entire blood flow region	129
6.10	Binary thresholded image for the normal perfusion case and the smallest shape that builds up the entire blood flow region	129
6.11	Image histogram based features	131
6.12	GLCM based feature (contrast)	131
6.13	GLCM based feature (correlation)	132
6.14	GLCM based feature (energy)	132
6.15	GLCM based feature (homogeneity)	133
6.16	GLCM based feature (contrast ratio)	133
6.17	Intensity variation based feature	134
6.18	Fractal based features	134
6.19	Standard deviation of brightness for heart slices	135

6.20	Architecture of a feed forward neural network	137
6.21	ROC curve	141
6.22	Confusion matrix for visual based classification	144
6.23	Confusion matrix for proposed classification method	144
6.24	Comparison of the performance	145
6.25	ROC comparison	146

LIST OF TABLES

Table	Title	Page No.
3.1	Performance measure values for the image enhanced using the proposed method	57
3.2	Performance comparison in terms of CI	59
3.3	Performance comparison in terms of ED	59
3.4	Performance comparison in terms of MSE	60
3.5	Performance comparison in terms of SSIM	60
3.6	Performance comparison in terms of PSNR	61
3.7	Performance comparison in terms of BM	61
4.1	PSNR, SSIM, BM and IEF values for various deblurring techniques applied on cardiac SPECT images blurred with a Gaussian PSF of sigma=3	86
4.2	PSNR, SSIM, BM and IEF values for various deblurring techniques applied on cardiac SPECT images blurred with a Gaussian PSF of sigma=5	86
4.3	PSNR, SSIM, BM and IEF values for various deblurring techniques applied on cardiac SPECT images blurred with a Gaussian PSF of sigma=7	87
4.4	PSNR, SSIM, BM and IEF values for various deblurring techniques applied on MPI Spectrum dynamics case study images blurred with a Gaussian PSF of sigma=3	88
4.5	PSNR, SSIM, BM and IEF values for various deblurring techniques applied on MPI Spectrum dynamics case study images blurred with a Gaussian PSF of sigma=5	89
4.6	PSNR, SSIM, BM and IEF values for various deblurring techniques applied on MPI Spectrum dynamics case study images blurred with a Gaussian PSF of sigma=7	89

5.1	PSNR, SSIM, IEF and IQI values for various denoising techniques applied on cardiac SPECT images	112
6.1	Comparison of different features obtained for normal and abnormal heart images	136
6.2	Comparison of correct detections by the proposed classification method and visual interpretations	145
6.3	Comparison of classifier accuracies with and without pre-processing stage	147
6.4	Comparison of the performance of proposed method with the method proposed in literature	148

ABBREVIATIONS

ACD	Annihilation coincidence detection
ART	Algebraic reconstruction technique
AUC	Area under curve
BHEASF	Bi-histogram equalization using adaptive sigmoid function
BM	Blur metric
BM3D	Block matching and three dimensional filtering
BPDFHE	Brightness preserving dynamic fuzzy histogram equalization
CAD	Coronary artery disease
CI	Contrast improvement
CLAHE	Contrast limited adaptive histogram equalization
CMR	Cardiac magnetic resonance
CTA	Computed tomography angiography
DFT	Discrete Fourier transform
ED	Entropy difference
FBP	Filtered backprojection
FN	False negatives
FNF	False negative fraction
FP	False positives
FPF	False positive fraction

GLCM	Gray level co-occurrence matrix
IEF	Image enhancement factor
IQI	Image quality index
KS	Kolmogorov-Smirnov
LR	Lucy Richardson
LV	Left ventricle
LVEF	Left ventricular ejection fraction
ML	Maximum likelihood
MLEM	Maximum likelihood expectation maximization
MPI	Myocardial perfusion images
MSE	Mean Square Error
OSEM	Ordered subsets expectation maximization
PET	Positron emission tomography
PSF	Point spread function
PSNR	Peak signal to noise ratio
QGS	Quantitative gated SPECT
ROC	Receiver operating characteristics
RV	Right ventricle
SPECT	Single photon emission computed tomography
SSIM	Structural similarity index measure
TN	True negatives

TNF	True negative fraction
TP	True positives
TPF	True positive fraction
TV	Total variation
WHO	World health organization
2D	Two dimensional
3D	Three dimensional

Chapter 1

INTRODUCTION

This chapter introduces the subject area of this research and addresses the contribution of the research work. The anatomy of the heart is described at a fundamental level. It presents a short description of different cardiac imaging modalities. The organization of chapters included in the thesis is summed up.

1.1 Introduction

The heart disease and stroke statistics update of the American Heart Association [1] issued in the year 2015 highlights disorders in heart functionality as the most significant cause of health related human deaths globally. It accounts for 17.3 million deaths per year and is expected to grow to about 23.6 million by 2030. According to World Health Organisation (WHO) heart disease deaths represent 31% of all global deaths [2] for the year 2015, demanding for a concrete action for the timely treatment [3]. The high incidence of heart failure all over the world [4] and its lifetime risk [5] has been addressed in literature. The prevalence of cardiac disorders among Asian Indians is higher than among Europeans, Americans and other Asians [6, 7]. Cardiovascular diseases cause about 40% of the deaths in urban areas and 30% in rural areas in India [8]. Studies of the past and ongoing research report the incidence of heart disorders to be a leading cause of mortality in India [9]. Cardiac ailments affect Indian population in their most productive midlife years [10, 11]. 23% of deaths due to heart disorders occur before the age of 70 in Western population whereas in India this accounts for 52% [12]. A survey conducted by Neo CarDiab Care [13] says that one fifth of the deaths in India are from coronary heart disease and it will account for one third of all deaths by the year 2020. This survey reports the early appearance of heart disorders among Indian population than their western counterparts by about 10 to 15 years.

The above statistics establishes the fact that cardiovascular diseases present a considerable challenge in maintaining human health and will burden the whole world in a few years' time. It shows the increasing need for cardiac care. The mortality rate due to heart disorders can be reduced

if proper diagnosis is done at the right time. As a natural aftermath in mitigating the risks in human cardiac condition, the past few years have witnessed an explosive expansion in the realm of cardiac imaging. New technologies capable of detailing the structure and function of heart have emerged [14]. Cardiac imaging modalities have a well-established role in the timely diagnosis of cardiac ailments. They have improved the evaluation of subjects with known or suspected heart disease.

1.2 Contribution of the thesis

The main contributions of this research to the domain of cardiac imaging includes

- Development of algorithms to improve the contrast and reduce the magnitude of noise and blur in cardiac nuclear images working on single photon emission principle.
- Development of pixel intensity based features that provide high classification accuracy for efficient classification of such images into those of normal and abnormal hearts.

1.3 Anatomy of human heart

The heart is an important organ which controls the human blood circulatory system. Right atrium, right ventricle (RV), left atrium and left ventricle (LV) constitute the four chambers of the heart. The deoxygenated blood from the body drains into the heart and is pumped to the lungs through right sided chambers (right atrium and RV). The oxygenated blood from the lungs drains into the left side of the heart and is pumped to the body parts by the LV. The deoxygenated blood from the upper and lower body parts drains into the right atrium through the

superior vena cava and inferior vena cava respectively. The left atrium receives oxygenated blood from the lungs through pulmonary veins. The RV pumps blood into pulmonary artery and the LV to the aorta. The atria are connected to the ventricles through atrioventricular valves (tricuspid valve on the right and mitral valve on the left). These valves prevent backward flowing of blood from the ventricles to the atria during cardiac pumping. Figure 1.1 shows the anatomy of human heart [15].

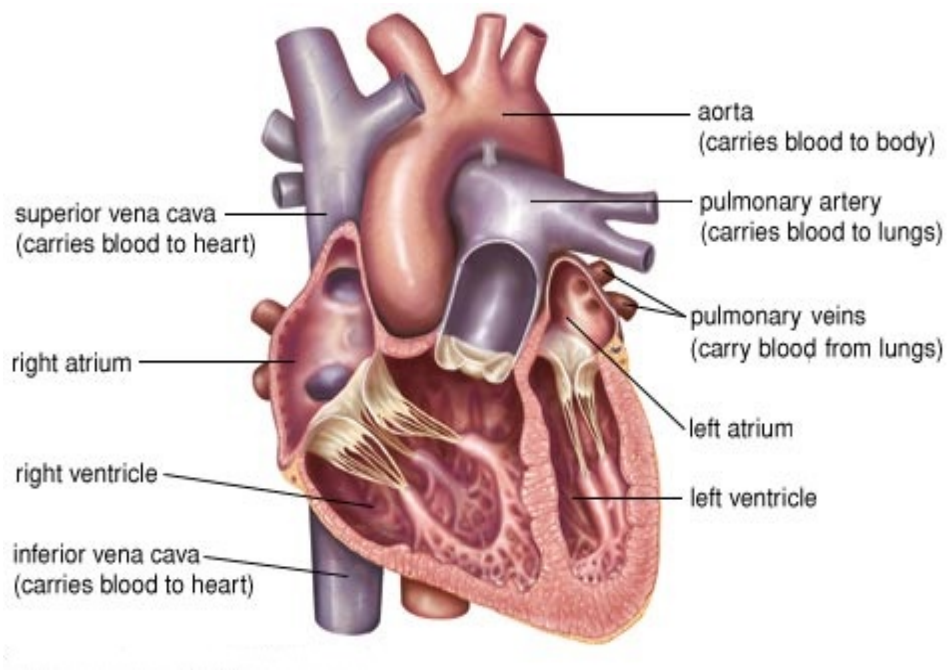


Figure 1.1 Anatomy of human heart [15]

The ventricles are cardiac chambers that collect blood from the atria and pump it out of the heart. The LV pumps oxygenated blood to the rest of the body. The monitoring of the left ventricular chamber is of primary importance in analyzing the function of heart as a pumping organ. The left ventricular walls are shown in figure 1.2. They are named

as anterior (A), septal (S), lateral (L) and inferior. IP represents the inferoposterior wall. The underside of the left ventricular region is the inferior wall.

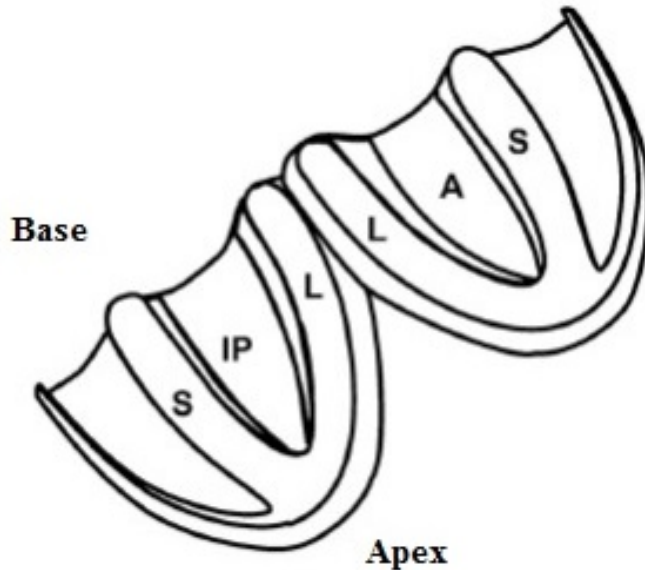


Figure 1.2 Left ventricular walls

Systole and diastole denote two fundamental periods of cardiac cycle [16]. During the ventricular systolic period of cardiac cycle the ventricles contract and during the diastolic period the ventricles relax and fill with blood. The dynamics of LV during the end systolic and end diastolic periods play a critical role in dictating the cardiac health [17]. Left ventricular ejection fraction (LVEF) represents the volumetric fraction of blood pumped out of the LV during each cardiac cycle [18]. It is computed from the end systolic and end diastolic blood volumes. LVEF is a fundamental predictor of coronary artery diseases (CAD) [19]. A low

value of LVEF is an early sign of heart failure. Low LVEF value shows that the heart is not pumping enough blood to the body parts.

1.4 Cardiac imaging modalities

CAD is a major cause of premature human deaths in modern industrialized countries. Assessment of heart functioning using cardiac images has proved valuable for diagnosis of CAD. Cardiac imaging renders a direct visualization means to see through the functioning of heart. Heart disorders are identified by analyzing cardiac images. The most common imaging modalities used to analyze cardiac vascular system are X-ray, echocardiography, computed tomography, magnetic resonance imaging and nuclear medicine imaging. Using the right imaging technique has improved the outcome of cardiac procedures substantially. A combined approach of more than one modality is also in use to give a much efficient diagnostic result than using a single modality.

1.4.1 X-ray

Angiogram is a popular test using x-ray imaging. It uses an invasive diagnostic procedure [20]. During x-ray imaging test, a special dye or a contrast material is injected into the veins or arteries through a thin, flexible tube called catheter. The catheter will be moved through the blood vessel till it reaches the heart. Then x-ray image is taken to watch its progress. The x-ray image is known as coronary angiogram. Various arteries are studied using different catheters. After completing the test the catheter will be removed from the body. Coronary angiography is done in special laboratories called ‘cath-labs’. The image provides a radiographic visualization of coronary vessels [21] and detailed information about the heart and coronary arteries. It is conducted to find out if the coronary

arteries are blocked or narrowed down and it assists the doctor to assess the degree of narrowing. In the case of patients suspected with coronary atherosclerotic or heart valve disorders, coronary angiography via left heart catheterization is used to evaluate coronary artery anatomy [22]. It is also used in planning surgical treatment of the heart and used as a research tool for the assessment of treatment results and the progression or regression of coronary atherosclerosis [23]. Figure 1.3 shows an example of coronary angiography.



Figure 1.3 An example of coronary angiography [24]

1.4.2 Echocardiography

Echocardiography uses ultrasound waves to image heart. Echocardiography makes use of the properties of sound waves to

differentiate tissues of varied density [25]. The speed of the wave depends on the density and elastic properties of the travelling medium. This property of the tissue is known as its acoustic density. The tissues comprising myocardium and blood have varied acoustic density. When a sound wave travels through an interface between two tissues of varied acoustic density, a portion of the energy is reflected backward (the reflected wave), and the rest travels forward through the next tissue (the refracted wave). The reflected wave is received by the transducer, turned back into electrical energy, amplified, and displayed [26]. The recent advances enable the acquisition of three dimensional (3D) images which provide real time 3D visualizations of the heart. A cardiac ultrasound image [27] is shown in figure 1.4. This image shows all four chambers of the heart and is very useful for detecting chamber enlargement.

There are different types of echocardiography. In transthoracic echocardiography the different heart views are obtained by moving the transducer to different chest locations [28]. Stress echocardiography is done to study blood flow to the heart before and after the heart is stressed. Doppler echocardiography [29] shows the blood flow through heart chambers and valves. In transesophageal echocardiography the probe is passed through the esophagus to get clearer heart images.

Ventricular systolic function and valvular disease can be assessed with reasonable accuracy [30]. Echocardiography is particularly useful in the evaluation of diastolic dysfunction.

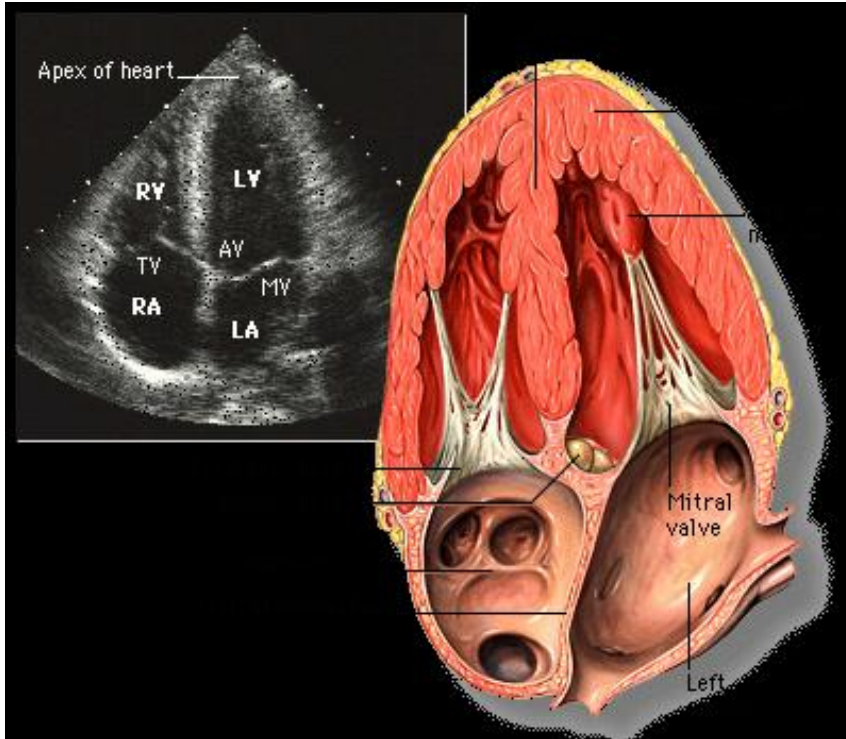


Figure 1.4 A cardiac ultrasound image showing all four chambers of the heart [27]

1.4.3 Computed tomography

Cardiac computed tomography, otherwise known as computed tomography angiography (CTA) is based on x-ray technique. It uses the concept of capturing the x-ray images of a high concentration iodinated contrast material while it flows through the coronary arteries [31]. The development of recent generation computed tomography scanners, especially those with 64 detector rows or greater, made it feasible to achieve adequate resolution to accurately image coronary artery plaque and stenosis [32]. A narrowly collimated x-ray beam is used to irradiate a slice of the body. The amount of radiation transmitted is collected by a number of photo-multiplier tubes. The tubes and detectors are rotated

around the body and different views are acquired to form the image. Ventricular systolic function, myocardial perfusion and coronary anatomy can be assessed using CTA [33]. A cross-sectional image from a cardiac CTA showing the right and left ventricles, the interventricular septum and the right coronary artery is given in figure 1.5.



Figure 1.5 A cardiac CT angiography [34]

1.4.4 Cardiac Magnetic resonance imaging

Cardiac magnetic resonance (CMR) imaging uses strong magnetic fields to image the functioning of heart. The patient is subjected to a high local magnetic field to align the protons in the body. These protons are excited by a radiofrequency pulse and detected by coils at the receiver [30]. MRI does not utilize any ionizing radiation. Radio waves redirect

alignment of hydrogen atoms that naturally exist within the body. It does not cause any chemical changes in the tissues. The hydrogen atoms after returning to their usual alignment emit energy. This emitted energy varies according to the type of body tissue from which they come. The MR scanner captures this energy and creates a picture of the tissues scanned based on this information [35]. CMR is useful for studying cardiac anatomy and function. A four chamber view from a cardiac MR image showing the left and right atria and ventricles is given in figure 1.6.

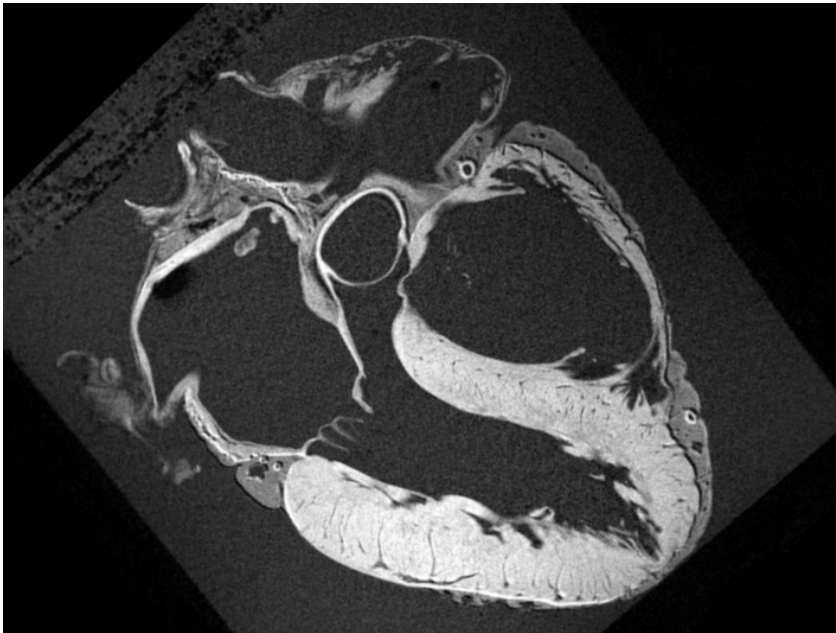


Figure 1.6 A CMR image [36]

1.4.5 Nuclear imaging

In nuclear imaging, a tracer is administered into the patient's body prior to the imaging process [37]. The tracer contains radioactive isotopes. These isotopes reach the organs to be imaged through the blood stream. Due to radioactive decay of the tracer isotope, gamma rays are emitted.

These gamma rays are detected and the image is reconstructed from the detected data. Nuclear imaging is useful in myocardial viability studies, CAD diagnosis and left ventricular function evaluation. Myocardial perfusion imaging (MPI) with induced stress improves the diagnostic accuracy [38]. The main imaging techniques under nuclear imaging use single photon emission and positron emission principles.

Echocardiography, CTA and CMR have better spatial resolution but nuclear imaging techniques have high sensitivity for tracer detection [30]. It enables the evaluation of perfusion, metabolism and neuronal function.

1.4.5.1 Single photon emission computed tomography

In single photon emission computed tomography (SPECT) imaging, the injected tracer emits radiation following radioactive decay [39, 40]. A scintillation crystal, along with multiple photomultiplier tubes, detects the radiation from the body. Since a single gamma ray is emitted per nuclear decay, a collimator is required for correct detection. The SPECT camera head is positioned at different angles around the body to acquire multiple views of the organ being imaged. The images are then reconstructed from the acquired data using different reconstruction software. Figure 1.7 shows some reconstructed slices in cardiac SPECT imaging [41].

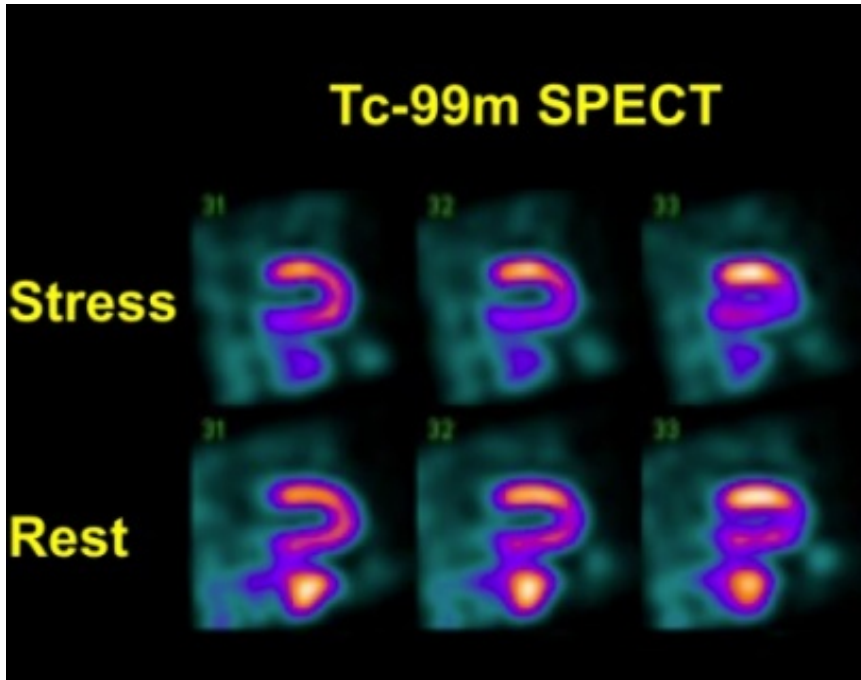


Figure 1.7 Cardiac SPECT image [41]

1.4.5.2 Positron emission tomography

Positron emission tomography (PET) imaging requires a positron-emitting radionuclide to be injected into the human body. Positrons or positively charged electrons are emitted from the radioisotopes. During positron emission, a proton is converted into a neutron in order to stabilize the nucleus. A positron comes in contact with an electron and the mass of the two particles is turned into two 511 keV gamma rays. These gamma rays emitted with 180 degree angle to each other are detected along a coincidence line. The underlying principles of PET is based on the annihilation coincidence detection (ACD) of the two 511 keV gamma rays [42]. The principle of ACD is detailed in figure 1.8. The gamma rays are detected using scintillation crystals and photo multiplier tubes. The coincidence circuit produces output when it receives two inputs

simultaneously from the gamma ray detectors. The coincidence line provides a more accurate detection method for forming images in PET [43]. PET image is reconstructed from the acquired data using reconstruction algorithms like filtered back projection or ordered-subsets expectation maximization. Figure 1.9 shows some reconstructed slices in cardiac imaging using PET.

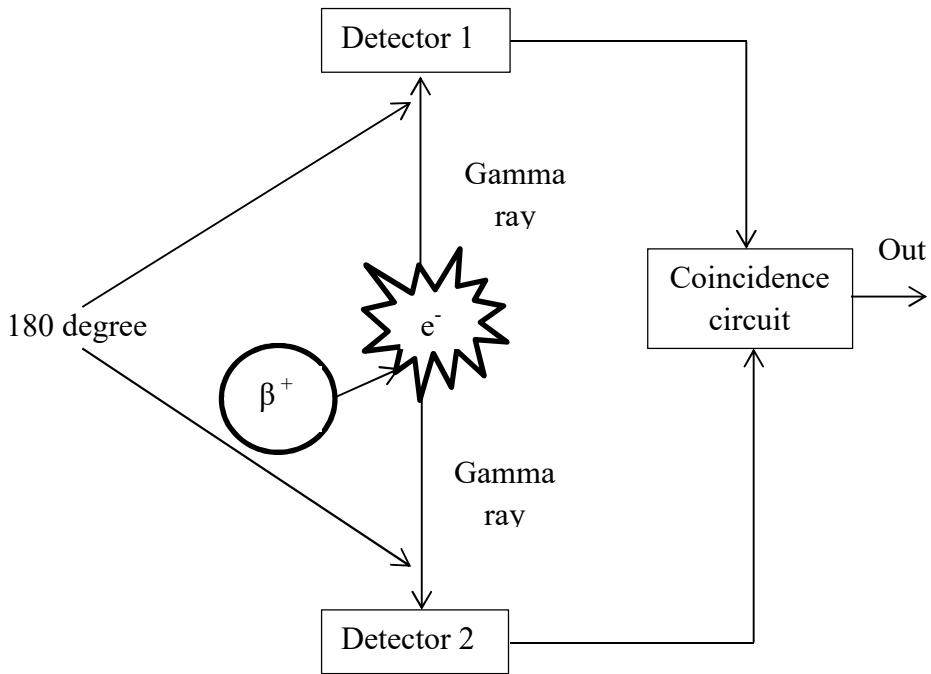


Figure 1.8 Basic principle of ACDC

PET imaging uses electronic collimation which results in better detection efficiency than SPECT imaging which uses physical collimation. The quality of PET image is better than SPECT image but the comparative cost of PET imaging is higher than that of SPECT imaging. For this reason, SPECT imaging is more popular among common population than PET imaging. The isotopes used for SPECT imaging have longer half-lives than PET imaging isotopes, allowing a lot of imaging time for performing SPECT scan. Moreover, the requirement of most currently available tracers in PET imaging makes it impractical for their widespread utilization. This limits the clinical use of PET imaging.

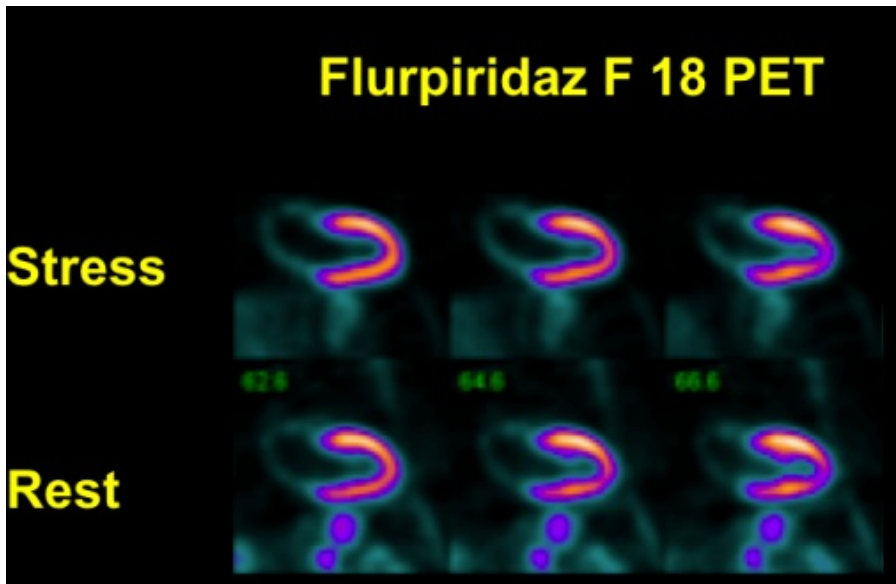


Figure 1.9 Cardiac PET image [41]

1.5 Organization of the thesis

The thesis is structured in seven chapters.

- Chapter 1 introduces the subject area including the heart anatomy, various cardiac imaging modalities, a brief summary of the thesis and its organization in various chapters.
- Chapter 2 gives a detailed explanation of the basic imaging principles of SPECT, conventional way of displaying slices in a cardiac SPECT image, a brief literature review mentioning the possibilities of research in the field of enhancement and classification of SPECT images, the motivation, scope and relevance of the proposed work.
- Chapter 3 discusses a novel method for improving the contrast features of cardiac SPECT images. The method makes use of morphological processing. The relevant theory behind morphological processing is described. Adaptive selection of the size of the structuring element is explained in detail.
- Chapter 4 describes the de-blurring technique suitable for cardiac SPECT image. The proposed blur reduction method uses total variation regularization. The chapter begins with a literature review on the available de-blurring techniques, followed by a description on the basic deconvolution techniques.

- Chapter 5 proposes a variance stabilization based noise reduction method suitable for cardiac SPECT images.
- Chapter 6 introduces an image feature based classification technique suitable for cardiac SPECT for identifying normal and abnormal heart perfusion. Different pixel intensity based features used for classification are explained in detail.
- The summary and conclusions based on the thesis are summarized in chapter 7. A brief description of the possible future work in the subject domain is also included in this chapter.

Chapter 2

LITERATURE REVIEW AND PROBLEM FORMULATION

This chapter covers the basic principles of SPECT imaging technique. Conventional way of displaying slices in SPECT image is explained. A brief literature review and the prospective research avenues in the field of enhancement and classification of SPECT images are addressed. This chapter ends with a discussion on the motivation, scope and relevance of the proposed work.

2.1 Introduction

MPI using SPECT can be used to assess the pumping ability of heart's LV [44]. It shows how well the blood streams through the heart muscle. In conventional medical practice, physicians use visual inspection of SPECT images and quantification results of images to reach the diagnosis report. Quantification results are obtained from validated software packages like Quantitative gated SPECT (QGS) [45, 46] and Emory toolbox [47]. In the existing form of diagnostic practice, the visual interpretation of SPECT images may result in inconsistent decisions. In such situations improving the visual quality of images through enhancement techniques and classification of images into normal and abnormal hearts using automated methods has been sought by the fraternity of radiological practitioners. Image enhancement intends to improve the interpretability or perception of information in images for human viewers or to provide better input for other automated image processing techniques. Evolving research in the field of enhancement and classification of SPECT images using image processing techniques also aims to overcome some of the inherent clinical limitations in improving the quality of such types of images.

2.2 Cardiac SPECT imaging

Cardiac SPECT is a nuclear imaging technique used to image the functioning of heart. It is useful in diagnosing CAD [48]. It is used as a diagnostic tool for the early detection of heart failure. It provides assessment of perfusion, function and viability of human heart. Areas of abnormal perfusion can be accurately identified from the SPECT images of heart. Both rest and stress SPECT tests are performed if required. The

images showing blood flow during rest and stress conditions are compared to identify living and irreversibly damaged heart tissues.

2.2.1 Basic principles

SPECT imaging works on the combined principle of radioactive decay and computed tomography.

Before MPI SPECT scan, a mild radioactive tracer is intravenously applied on the patient. The tracer undergoes the phenomenon of radioactive decay, whose magnitude is within the accepted limits for clinical human application. In radioactive decay the nucleus of an unstable atom loses energy by emission of ionizing radiations. Such unstable atoms which exhibit the property of radioactive decay are known as radionuclides or radioisotopes [49]. The desirable properties of an ideal tracer are [39]:

- It should distribute in the myocardium in linear proportion to blood flow.
- During scan it should provide stable retention in the myocardium.
- It should be readily available.
- It should have good imaging characteristics.

Technetium-99m is one of the most frequently used radioisotopes in nuclear imaging [50]. It is symbolized as ^{99m}Tc . It decays with a half-life of about 6 hours by emitting gamma rays [49].

The injected tracers are taken up by the heart muscles in proportion to blood flow. Areas of myocardium with impaired blood flow will have reduced tracer uptake [51]. The uptake of tracer in the heart is then assessed by imaging the patient with a gamma camera. The gamma

camera is capable of detecting small amounts of radiation emitted by the tracer. The detected radiations are converted into images using image acquisition and reconstruction algorithms. These images help the physicians to see if the blood flow is reduced due to narrowed arteries.

As an added diagnostic tool, a stress/rest myocardial perfusion imaging study [52] is performed optionally to inspect the effect of physical stress on the blood flow through myocardium. In this case the patient's heart is imaged using SPECT imaging principles before and after exercise. For the stress study the heart rate is elevated to its peak by asking the patient to run on a treadmill. A pharmacologically induced stress test is given to patients who are unable to exercise.

2.2.2 Image acquisition

Special detection hardware and reconstruction software are used to detect the emitted radiation and to reconstruct the resultant images respectively. The projection information required for SPECT image reconstruction is obtained by detecting gamma rays emitted from the radiopharmaceutical isotope injected in the body. This data acquisition can be static or dynamic. In static acquisition, data required for a single image is acquired in a predetermined time interval. In dynamic acquisition, data are acquired to reconstruct a sequence of images for a cardiac cycle to follow the flow of the radiotracer. Special gamma cameras are used for this purpose. The gamma camera is rotated around the patient to record gamma rays from different angles. Figure 2.1 shows a SPECT gamma camera system. The underlying principles of SPECT imaging is given in figure 2.2.

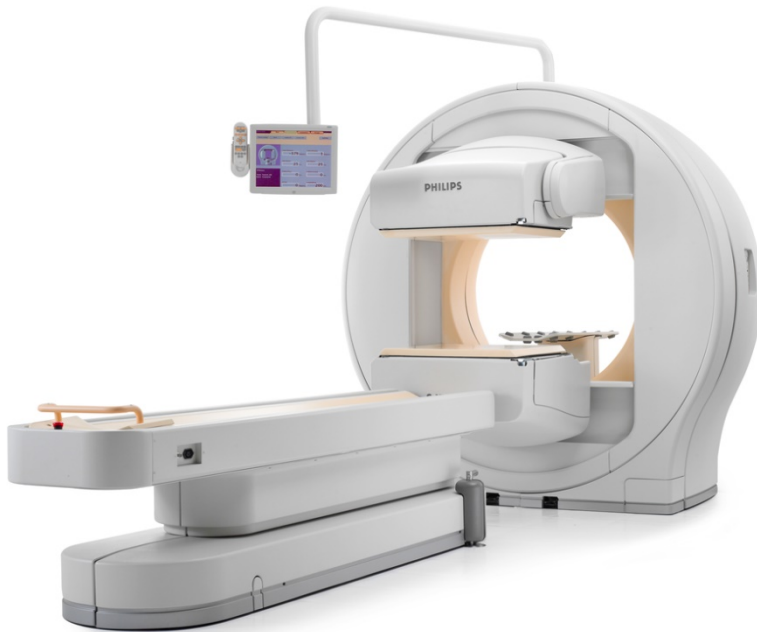


Figure 2.1 SPECT gamma camera system[53]

The basic design of a gamma camera consists of a scintillation crystal coupled to an array of photomultiplier tubes [54] as shown in figure 2.3. A collimator is attached to the front of the gamma camera head to focus gamma rays to the scintillation crystal. There are different types of collimators like parallel-hole collimator, diverging multi-hole collimator and pinhole collimator. For imaging a large object with a small camera, a diverging multi-hole collimator is used. A pinhole collimator is used for imaging small organs with high resolution. A parallel-hole collimator, which is most commonly used in nuclear imaging [55, 56] consists of a number of holes in a lead plate. The gamma rays entering along the direction of the holes reach the crystal and all other rays are absorbed by the lead as shown in figure 2.4. The collimator helps to avoid obliquely incident gamma rays which may blur the image. Low energy high resolution collimators are usually used with ^{99m}Tc tracers [57].

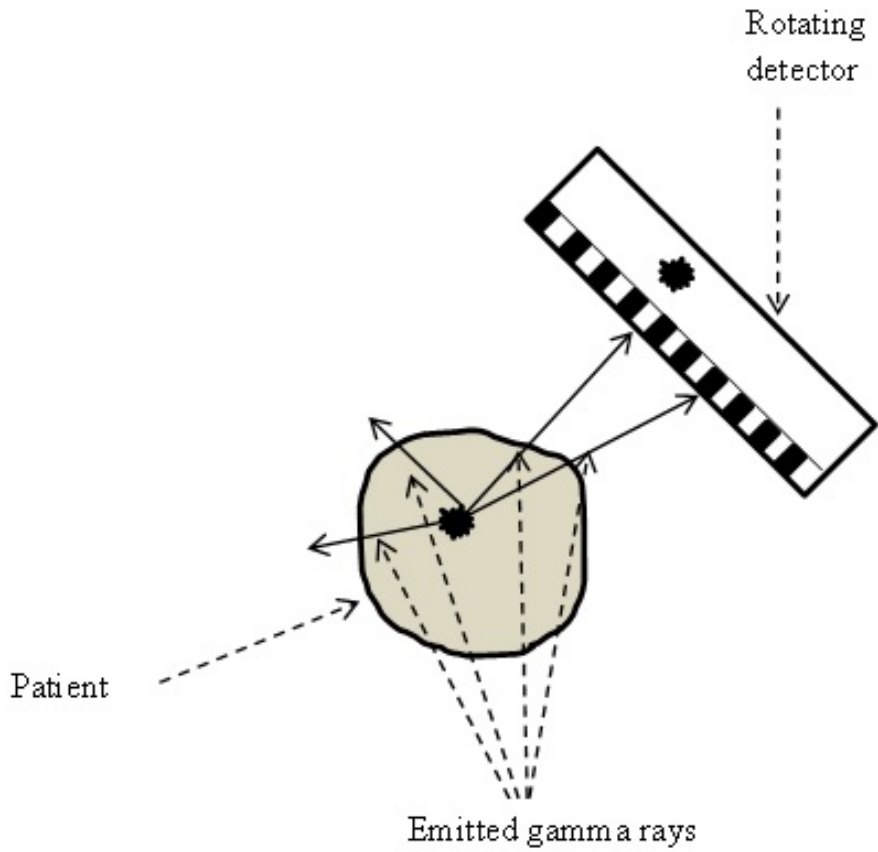


Figure 2.2 Underlying principles of SPECT imaging

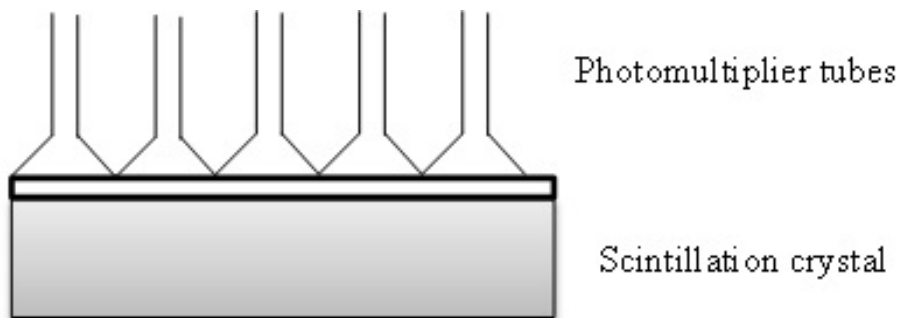


Figure 2.3 Basic elements of a gamma camera head

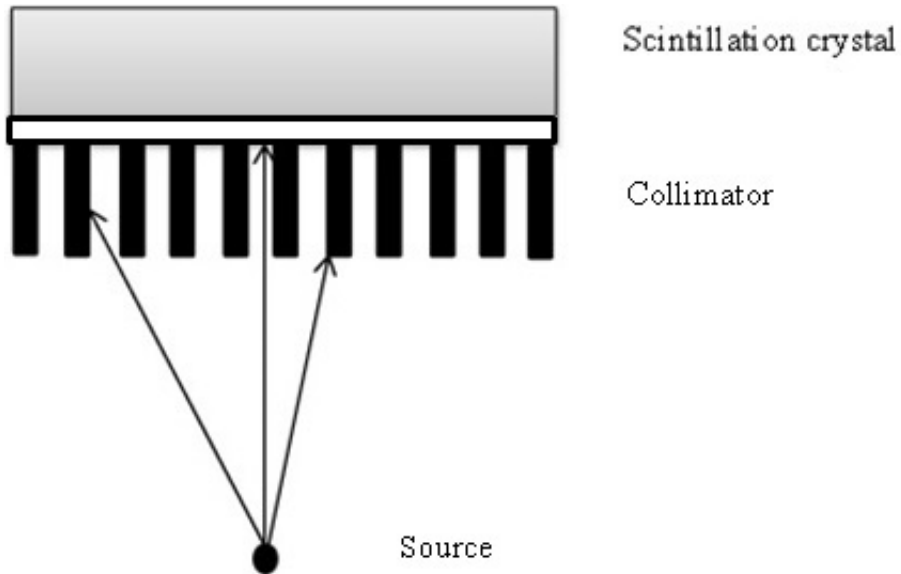


Figure 2.4 A parallel-hole collimator attached to scintillation crystal.

The spatial resolution, full width half maximum, depends on the width of the average intensity distribution from a point source placed at a distance d from the collimator. If R_s denotes the spatial resolution, c the diameter of the collimator hole, t the thickness of the collimator and b the distance from the back of the collimator to the scintillation crystal then the R_s is given by equation 2.1.

$$R_s = \frac{c(t+d+b)}{t} \quad (2.1)$$

The most commonly used acquisition mode is step-and-shoot mode. ECG-gated acquisition is also possible in this mode. The camera moves to a position, stops and acquires data and then moves to the next position. Image data is not acquired during the motion of the camera. The

projection images are usually acquired over 180° arc on a matrix of $64*64$ or $128*128$ pixels.

2.2.3 Image reconstruction

The gamma camera is orbited around the patient's body to acquire data at regularly spaced angles. The acquired data are processed and stored as two dimensional reconstructed images. The process of putting together the acquired data from different angles to form the organ's image is called image reconstruction. The reconstructed image is the discrete representation of a cross section of the isotope distribution within the organ [58]. There are reconstruction algorithms to calculate a three dimensional radioactive distribution from the acquired projection data [59]. In nuclear medicine, image reconstruction is performed using step-by-step mathematical procedures implemented in a computer. Image reconstruction can be done either by analytical algorithms or iterative algorithms. Filtered backprojection reconstruction is an example where analytical algorithm method is applied and iterative reconstruction method uses iterative algorithms.

2.2.3.1 Iterative reconstruction method

Iterative algorithms find solution by successive estimates [60]. The projection noise can be handled and the imaging physics can be modeled in an easier way in iterative reconstruction method. This makes it popular in nuclear medicine [61]. Figure 2.5 shows a schematic description of the iterative reconstruction method [62].

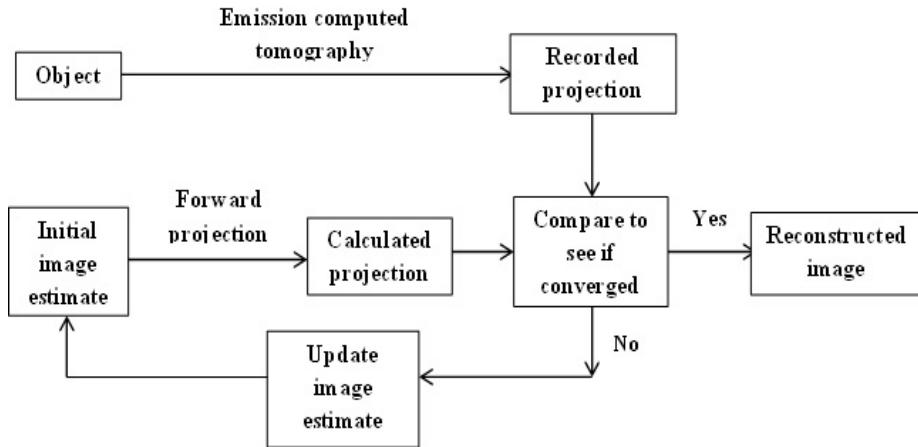


Figure 2.5 Schematic illustration of iterative reconstruction algorithm

An initial estimate of the image, usually a simple image with uniform statistical distribution, is set. Then the projections that would have been measured for the initial image estimate is computed using a mathematical process called forward projection. Computed projections are compared with recorded projections. The image estimate is updated using the comparison results. This compare-and-update process is repeated until the comparison results fall below a specified predetermined level. Statistical algorithms like maximum likelihood expectation maximization (MLEM) [63] or ordered subsets expectation maximization (OSEM) [64, 65] and algebraic methods like the algebraic reconstruction technique (ART) [66] fall under the category of iterative reconstruction methods. MLEM algorithm is most frequently used in nuclear medicine imaging. Poisson noise is assumed to be present in the projection data and

a set of linear equations are solved to obtain an image with nonnegative pixel values in MLEM algorithm.

2.2.3.2 Filtered backprojection method

In filtered backprojection (FBP) method the projection dataset is back projected and filtered to eliminate blurring [67]. A straight line through the 3D object being imaged is represented by the projection row data. The projections are run back through the image. Back projection technique redistributes the count number at each point back along a line from which they were originally detected. To eliminate the problem of blurring the projections are filtered before being back projected onto the image matrix. A ramp filter is usually used for filtering.

2.2.4 Conventional slice display of cardiac SPECT images

Three sets of image slices are reconstructed and displayed in cardiac SPECT images. The planes of cut for imaging are chosen to get a view of the heart perpendicular to the long axis of the left ventricle, a view of long axis heart slices in the horizontal plane and a view of long axis heart slices in the vertical plane. These slices are called short axis, horizontal long axis and vertical long axis slices respectively [68]. The planes are shown in figure 2.6. In the figure RV represents the right ventricle and LV represents the left ventricle.

The arrangement of different slices [68] to depict cardiac functioning is shown in figure 2.7. The short axis slices are arranged from apex to base. The display starts with the apical short axis slice in the top left corner with progression of slices toward the heart base from left to right. The vertical long axis slices are displayed with septal slices on the

left, progressing through the mid-ventricular region to the lateral wall slices towards right. The horizontal long axis slices are displayed from inferior wall to anterior wall.

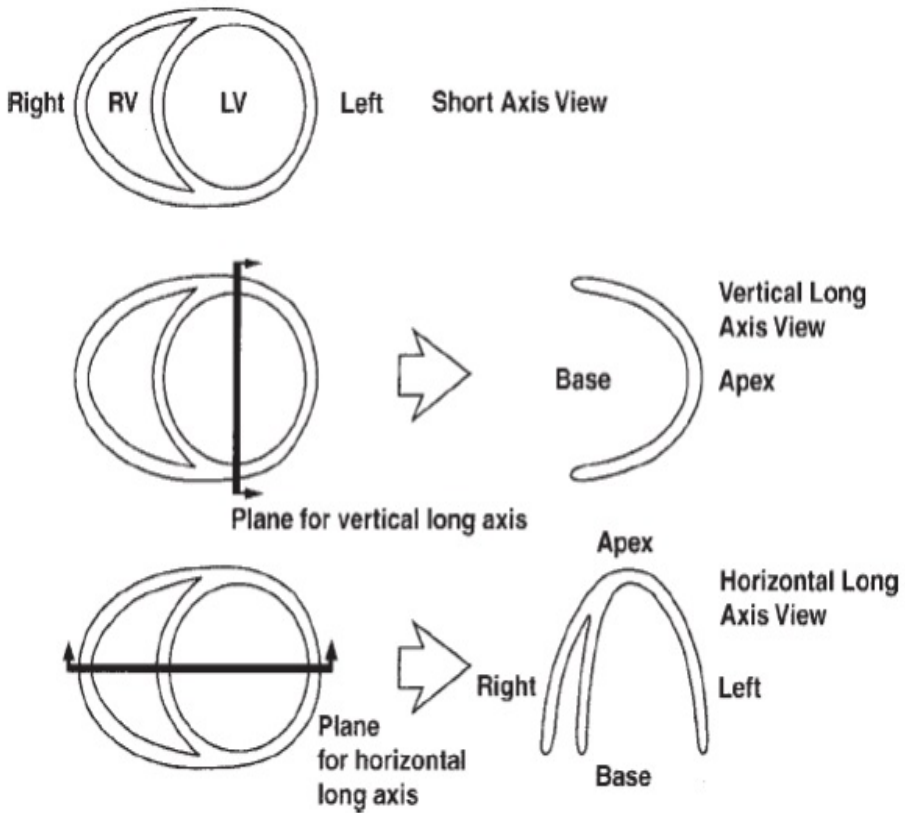


Figure 2.6 Standardized planes of cut for reconstructed SPECT slices [68]

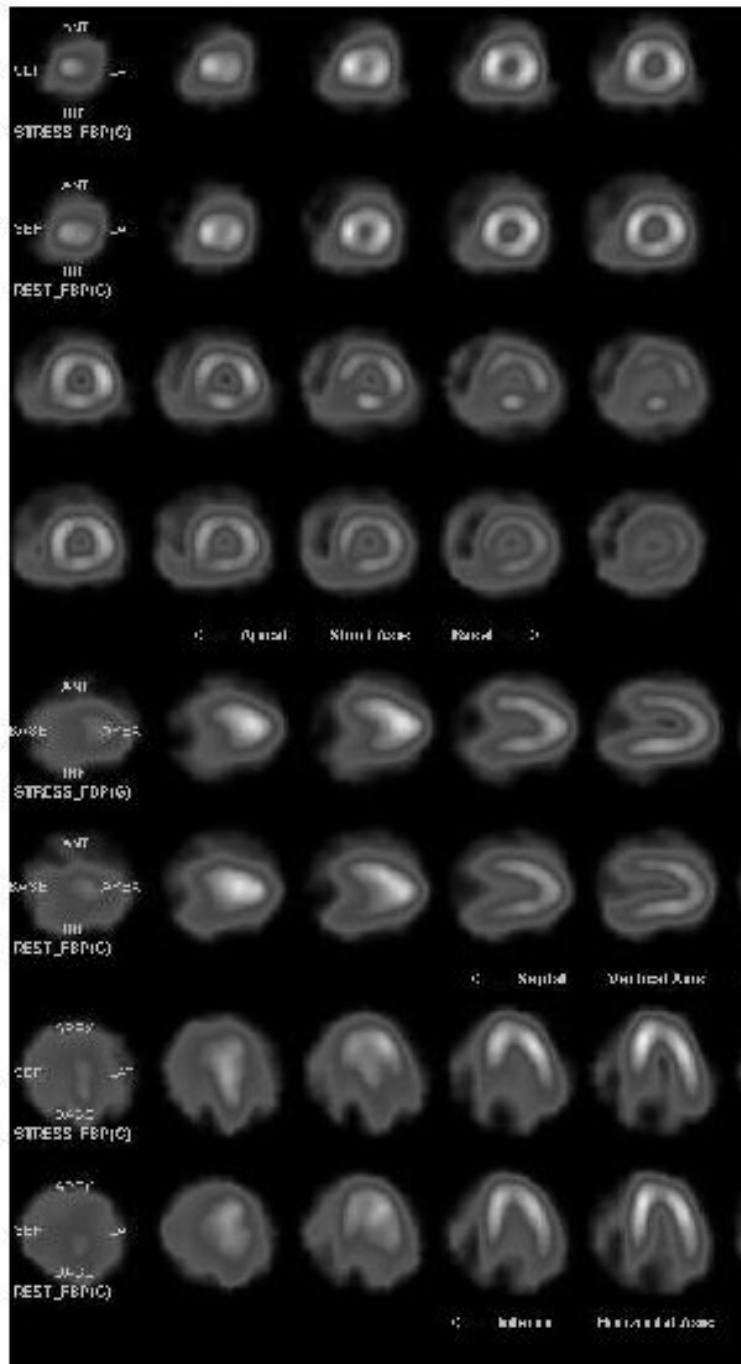


Figure 2.7 Reconstructed SPECT slices

Figure 2.8 shows a slice with abnormal perfusion in the real cardiac SPECT image in the short axis view. It is a two-dimensional (2D) image which shows the amount of tracer uptake in the corresponding plane at an instant of time in the gated heart cycle. The bright region represents the presence of tracer. A short axis view slice with normal perfusion is shown in figure 2.9.

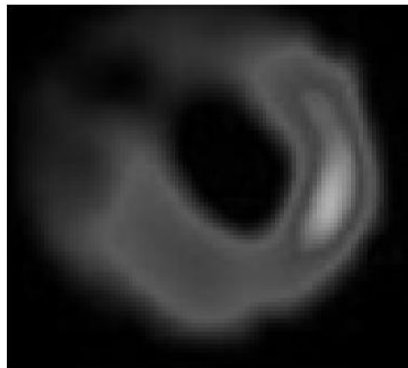


Figure 2.8 An image slice with abnormal perfusion in the short axis view



Figure 2.9 An image slice with normal perfusion in the short axis view

2.3 Literature review and research potential in the field of enhancement of SPECT images

Different imaging techniques are currently in use for a reliable assessment of heart functionality. SPECT perfusion imaging is a well-developed technique for diagnostic assessment of coronary heart diseases. The technique, though initially developed in the 1950's, has come to widespread use only for the past 35 years [69, 70]. Currently it represents about 33% of all stress perfusion imaging performed in United States and the percentage is growing. The extent and severity of coronary diseases can be assessed by the presence and extent of perfusion defects [71]. Cardiac SPECT images are very often used to study the functionality of heart. These images, notwithstanding their wide acceptance, present cases of bad contrast, high amount of noise and blur. One method before the physicians to enhance the image quality is to increase the acquisition time [72]. But the efficacy of this method is limited, as it requires the patient to remain stock-still during the acquisition period. Another method is to increase the dose of radioactive tracer. But in this case dosimetry constraints have to be carefully taken care of [73]. More powerful camera systems can also be used for better images [54], which demand for a much better financial and technical set up. These limitations present a potential challenge for a researcher in the image processing domain.

From a SPECT perfusion image a nuclear medicine expert can differentiate between a scar, a live heart muscle that doesn't have enough blood supply and a healthy heart muscle with adequate blood supply [74]. Due to the imaging techniques involved, images present low contrast, high amount of noise and blur [75, 76]. Enhancement techniques result in

improved images so that the nuclear medicine physicians can effectively distinguish areas even with low tracer content.

Considering the practical and technical constraints posed by the clinical methods, software solutions are being proposed to improve the quality of images. The literature describes different enhancement algorithms suitable for medical images, which results in modified image output with more visual information [77, 78]. Wang et al. [79] proposed a technique involving segmentation using thresholding and region growing. Falk et al. [80] developed a mean field annealing method for the enhancement of nuclear images, which demands a longer computational time. Rajabi et al [81] and Lyra et al [82] compared different filters for the enhancement of SPECT images. Many authors proposed restoration methods utilizing constrained de-convolution [83] and supervised blind de-convolution [84] in nuclear images. But this results in the introduction of noise in SPECT images. Yousif et al [85] proposed a combined approach of top-hat filtering and de-blurring for improving the quality of nuclear images. The deblurring stage introduces noise in SPECT image.

The choice of a particular method, as explored in the existing literature, is a compromise between information suppression, change in contrast and extent of noise reduction. But ideally, the enhancement technique should preserve region boundaries and should not generate artefacts. There is therefore, the need for a solution which improves the image quality from a diagnostic perspective, while retaining the trueness of its information. This, in turn, would aid the attending physician to have a more accurate visualization on how the heart functions.

2.4 Literature review and research potential in the field of classification of cardiac SPECT images

The idea of computer assisted systems in cardiac diagnosis field has gained considerable research attention in the past few years [86-89]. Different classification methods are available in literature for identifying normal and abnormal heart functioning. They include methods using perfusion images [90] and bull's eye scintigrams [91].

The first step in cardiac image interpretation includes visual analysis of the perfusion images by the nuclear medicine expert. As the manual interpretation is a difficult task, experts prefer to use adequate computer aided techniques to assist judgement. With faster computation becoming viable, accessible and cheap, research in the field of computer aided diagnosis has kept its momentum going [92, 93]. Artificial intelligence based methods have been investigated as a way to assist myocardial perfusion imaging studies over the past several years. The development of methods based on neural network principles [94-96] and case-based techniques [97] have assisted myocardial perfusion planar and SPECT studies. A systematic validation of the diagnostic performance of computer aided system for the interpretation of SPECT studies has also been carried out in literature [98]. The use of SPECT imaging for the assessment of cardiac health continues to grow at a furious pace. It still demands for efficient tools for assisting physicians in quick interpretations, pinning it as a promising research domain.

A physician uses perfusion images along with the results from quantification software to make a conclusion on whether the heart's

pumping ability is normal or abnormal. If an image processing algorithm is developed which can predict the pumping ability of the heart from the perfusion images, it could serve as a computer assisted diagnostic tool to aid the physicians for making an initial interpretation of cardiac health without using expensive quantification software.

2.5 Motivation

Accurate and timely diagnosis of heart functioning disorders can help in reducing related human mortality. Recent advances in cardiac imaging modalities allow more accurate quantification and analysis of cardiovascular system. Among these modalities nuclear imaging techniques play an important role. Both SPECT and PET come under nuclear imaging techniques. Due to the lower cost and better availability of tracers, cardiac SPECT imaging is more popular, though PET imaging provides high quality images. Methods assisting better diagnostic visualization and interpretation of SPECT images are extremely important for increasing the clinical use of SPECT imaging.

Most of the enhancement methods, described in literature, focus on one or the other quality of the image. The advantage is that the focused quality is improved but the disadvantage is that some other quality may get affected. For example the region boundaries may get affected while reducing noise or some artefacts may get generated while improving contrast. This presents itself a substantial case for the development of enhancement techniques to improve the image quality, while retaining the trueness of its information. Moreover the pixel intensity distribution is different for different slices of SPECT image depending on the tracer content. An enhancement technique which works well for a high tracer

content slice may not give satisfactory result for a low tracer content slice. In an effort to address these issues, the thesis proposes image dependent methods to enable an improved outcome in SPECT image enhancement.

Most of the classification algorithms described in literature uses the results from some quantification software even for initial diagnosis. The thesis proposes a classification method using features extracted from the reconstructed SPECT images without using any quantification software.

2.6 Scope and relevance

Heart disease is a major health issue which is constantly on the rise all over the world with a pattern of incidence dominating in certain geographical locations [99]. The current estimates by Shraddha et al. [100] indicate that mortality rate due to heart disorders tops the list in the number of deaths in India due to non-communicable diseases. Heart disorders are expected to be the fastest growing of human health maladies by 2015 [101]. Figure 2.10 shows that the incidence has gone up significantly for people in the age group 20-69 and projects the alarming situation in the Indian population.

Smoking, diabetes, hypertension, abdominal obesity, psychosocial stress, unhealthy diet, and physical inactivity contribute to the risk factors [102]. Some of the challenges that face cardiac care in India are inadequate healthcare infrastructure, lack of accessibility to modern facilities and the high price tagged for efficient and effective diagnosis and treatment.

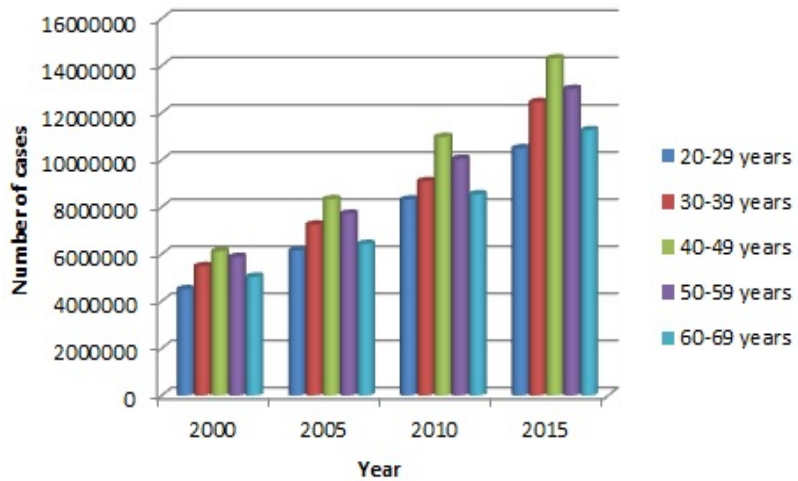


Figure 2.10 Number of cases of heart ailments in different age groups among Indian population

Cardiac SPECT is a widely used imaging technique for effective diagnosis of heart disorders. In the existing form of diagnostic practice, the visual interpretation of SPECT images may result in inconsistent decisions. In such situations, improving the visual quality of images through enhancement techniques and classification of images into normal and abnormal hearts using automated methods has been sought by the fraternity of radiological practitioners. Existing classification algorithms use some quantification software results for identifying normal and abnormal heart functioning. This demands more from the financial side of the patient. The scope of this work is to improve the quality of cardiac SPECT images by improving contrast, reducing noise and reducing blur without compromising on its information content. Separate contrast improvement, denoising and deblurring algorithms are developed so that they can be used independently or in combination, depending on the

quality need of the SPECT image. The work also aims at identifying normal and abnormal heart functioning from the images itself without using any quantification software. The images are classified into those of normal and abnormal hearts. The intent of this effort is to facilitate a more well-informed interpretation of images by the cardiologist. Application of these techniques would add value to the existing image processing techniques in medical imaging, leading to a more accurate and accomplished diagnosis of cardiac maladies and therefore contribute to the upkeep and well-being of the whole society.

The thesis proposes three independent enhancement techniques and one classification technique. The novelty of the enhancement techniques presented in the thesis is that all the three methods work equally well on all types of SPECT image slices (normal and abnormal perfusion short axis and long axis slices). The developed algorithms involve steps to analyze each slice and the parameters are chosen accordingly. The quality of the image is enhanced retaining their data integrity. The novelty of the classification phase is that the proposed features mimic the visual features that are being used by a physician to identify heart functioning. Then a neural network classifier is employed to reflect the decision of human brain.

2.7 Database used

Cardiac SPECT images were obtained from Medical Trust Hospital, Kochi, India. The images were captured using GE machine. Around 100 images were collected for experimental analysis. The results were verified by the nuclear medicine physicians, Dr. Kuruvila Varkey of

Bharat Scan centre, Kottayam, India and Dr. Shamily Goerge of Medical Trust hospital, Kochi, India.

Sample images were also sourced from the image database of case studies published by Spectrum dynamics medical [103].

For all the experiments included in the thesis grey scale images were used.

Chapter 3

ENHANCEMENT OF CONTRAST IN CARDIAC SPECT IMAGES

An image processing technique based on morphological processing has been developed for improving the contrast features of cardiac SPECT images. The method utilizes the concept of adaptive technique in morphological processing. The approach is unique in its use of adaptive neighbourhood for the processing of different image regions. Qualitative and quantitative evaluations prove the effective performance of the proposed algorithm in enhancing cardiac SPECT images.

3.1 Introduction

The application of radioactive isotopes for imaging human body parts developed into nuclear imaging technology, including SPECT and PET [104]. A cardiac SPECT image provides a visual representation of the heart functioning [105, 106]. Both gray scale and color images can be generated by cardiac SPECT systems. A nuclear medicine physician visually analyses the SPECT images and interprets them, guided by the variations in color intensity (in the case of color images) or gray scale intensity (in the case of gray scale images). Differences in intensity in image parts corresponding to various levels of radioactive uptake in the organ results in image contrast. Visual inspection and interpretation of SPECT images is a challenging task as there is random scattering of photons during the image reconstruction process which affects its contrast. The amount of radiopharmaceutical determines the major component of image contrast. Recognizing even a gradual change in gray scale intensity, aids in the interpretation of images and helps in identifying small defects and leads to better inter-observer agreement. Contrast improvement is being used in the field of medical image enhancement to improve its visual appearance so that pixel intensity changes can be easily identified [107].

The main function of contrast enhancement is to improve the interpretability of information contained in the image for a human observer. Contrast enhancement makes it easier to separate the dark and bright areas in the image. In the case of cardiac SPECT images the functioning of the heart is analyzed by looking into the pattern of bright area with respect to the dark area. So contrast improvement employing the correct methods helps in the true interpretation of SPECT images.

3.2 Literature survey

The literature describes different algorithms for medical image enhancement, which resulted in modified image output with more visual information [78]. Histogram equalization [108, 109] was a popular technique to perform contrast enhancement. The method was simple and effective in changing the brightness of the image to provide a global enhancement. But visual artefacts got introduced in the enhanced image which led to incorrect interpretation of images.

In brightness preserving bi-histogram equalization [110], the image was divided into two sub images and histogram equalization was applied individually. The mean brightness of the image was preserved, thus providing a natural enhancement effect.

Ibrahim et al. [111] proposed a brightness preserving dynamic histogram equalization method to obtain the enhanced image with mean intensity almost equal to the mean intensity of the input image. Brightness preserving dynamic fuzzy histogram equalization method developed by Sheet et al. [112] was a modification of brightness preserving dynamic histogram equalization technique which improved the brightness preserving and contrast enhancement abilities at a low computational complexity. Images were represented and processed in the fuzzy domain.

Another method to enhance the local contrast of an image is by the use of adaptive histogram equalization [113]. In contrast limited adaptive histogram equalization (CLAHE), the contrast of an image was enhanced by applying contrast limited histogram equalization on small

data regions called tiles rather than the entire image [114]. The resulting neighbouring tiles were then stitched back smoothly using bilinear interpolation. By limiting the contrast in the homogeneous region, noise amplification was avoided. Shome et al. [115] used CLAHE to enhance diabetic retinopathy images.

Ahmed et al. [116] developed a method for enhancing an image using three steps. Median filtering was employed to reduce noise, unsharp mask filtering was used to sharpen edges and CLAHE was used to enhance contrast.

Edgar et al. [117] proposed a method to overcome the problem of over enhancement produced by simple histogram equalization. With mean as threshold, the image histogram was divided into two sub-histograms and their cumulative distribution functions were replaced with two smooth sigmoids. The method performed well in terms of contrast enhancement and brightness preservation.

A technique which automatically extracted nuclear boundaries by segmentation using thresholding and region growing has been explained by Wang et al. [79]. Falk et al. proposed a method for the enhancement of noisy nuclear images using mean field annealing [80]. In both these methods, the work was accomplished on planar images. A similar method was proposed by Wang et al. [118] for the enhancement of gated cardiac nuclear images. It used a combination of mean field annealing and gradient edge detection and the work was done on images in gray scale. Mean field annealing gave good results on planar images but demands for a longer computational time when it comes to the reconstructed SPECT slices.

Hanan et al. [119] employed a method suitable for the enhancement of medical images including nuclear images. The method used median filtering for removing noise, unsharp mask filter to sharpen the edges and CLAHE for contrast improvement. The method improved the visual quality of the image.

In the histogram of a normal perfusion slice the pixel intensities corresponding to tracer content region is clearly visible and it is possible to enhance that particular region. For abnormal perfusion slices the histogram varies very much for different slices. So histogram based methods generally do not give satisfactory results for a SPECT image which contains different slices.

3.3 Preliminary concepts in morphology

Morphological image processing [120] is an important tool for image enhancement. It involves the use of mathematical morphology for describing quantitatively the geometrical information of image objects. Morphology was introduced in the late 1960s [121] and since then it has been used in the field of image processing for various applications. Mathematical morphology is expressed in terms of set theory. In mathematical morphology, the image and the objects in the image are treated as sets. An image A is represented by a two dimensional set of pixels in a rectangular format where, $A(i,j)$ is a pixel at coordinate (i, j) in the image A . In morphological image processing the image is processed by a series of morphological operations using another set known as a structuring element which exploits the geometrical information in the image. The structuring element S is also represented by a two dimensional set of pixels. The basic morphological operations are dilation, erosion,

opening and closing. The dilation of a binary image A by the structuring element S, where A and S are members of the two dimensional integer space Z_2 , is given in equation (1) and equation (2).

$$A \oplus S = \left\{ z \left[\begin{array}{c} \hat{S} \\ \hline \end{array} \right]_z \cap A \neq \phi \right\} \quad (1)$$

$$A \oplus S = \left\{ z \left[\begin{array}{c} \hat{S} \\ \hline \end{array} \right]_z \cap A \subseteq A \right\} \quad (2)$$

$$\hat{S} = \{w | w = -s, s \in S\} \quad (3)$$

$$\left[\begin{array}{c} \hat{S} \\ \hline \end{array} \right]_z = \left\{ c | c = s' + z, s' \in \hat{S} \right\} \quad (4)$$

The erosion of A by S is given in equation (5).

$$A \ominus S = \left\{ z \left[\begin{array}{c} S \\ \hline \end{array} \right]_z \subseteq A \right\} \quad (5)$$

The opening and closing of set A by the structuring element S is defined in equation (6) and equation (7) respectively.

$$A \circ S = (A \ominus S) \oplus S \quad (6)$$

$$A \bullet S = (A \oplus S) \ominus S \quad (7)$$

The dilation of the gray scale image A, with domain D_A , by the structuring element S, with domain D_S , is given in equation (8).

$$(A \oplus S)(p, q) = M_{\max} \quad (8)$$

M_{\max} is the maximum value of $f(p-x, q-y) + S(x, y) / (p-x, (q-y) \in D_A ; (x, y) \in D_S$

The erosion of the gray scale image A, with domain D_A , by the structuring element S, with domain D_S , is given in equation (9).

$$(A \ominus S)(p, q) = N_{\min} \tag{9}$$

N_{\min} is the minimum value of $f(p+x, q+y) - S(x, y) / (p+x, (q+y) \in D_A ; (x, y) \in D_S$

3.4 Proposed method

Cardiac SPECT images in gray scale were considered while developing methods for contrast improvement. The basic block diagram showing different stages in the proposed method is given in figure 3.1.

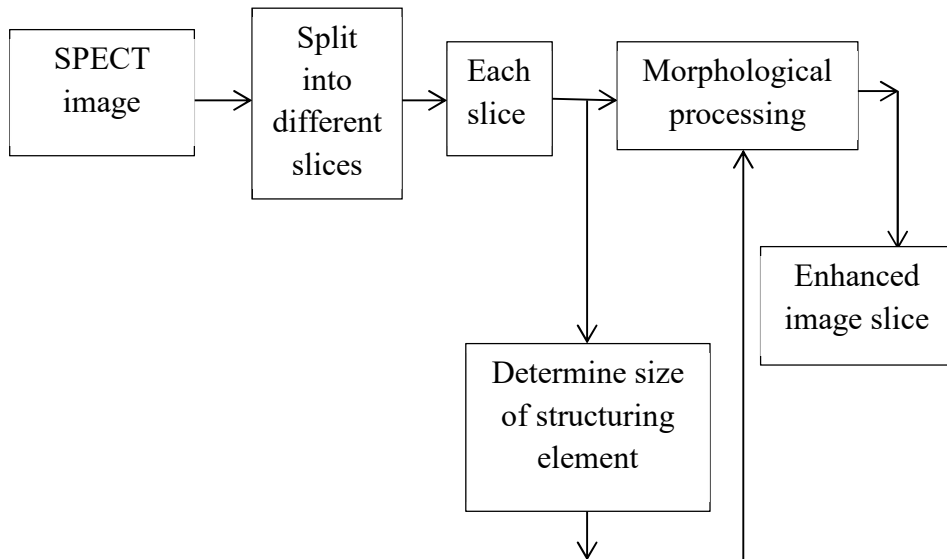


Figure 3.1 Block diagram showing the basic stages in the proposed method

The main stages in the proposed method are selection of the size of the structuring element suitable for each slice adaptively and morphological processing of each slice with the corresponding structuring element.

3.4.1 Adaptive selection of the size of structuring element

The whole image itself is divided into many slices, T_{gi} , each with lower dimension. Each slice shows the distribution of tracer in a heart region at a specific time in a given view. Each slice is then processed morphologically by using structuring elements. The structuring element keeps moving through the slice and on its way, operates on pixels in a predefined neighbourhood. If the size of this neighbourhood area is chosen as the same for every slice throughout the image, certain intricate portions may not be processed as required. Since cardiac nuclear images depict the pumping action of heart, the nature of the image slices will be different depending on the amount of tracer present. In order to prevent over enhancement and under enhancement of image regions, the size of the structuring element is chosen adaptively. The slices are processed using structuring elements whose sizes depend on their own nature. Figure 3.2 shows the steps in determining the size of structuring element.

An analysis of pixels is made for each slice to get an idea about the amount of tracer content and the size of the structuring element is chosen accordingly, to give a better result. Analysis is done using binary thresholding. Each slice is converted into a binary image. The output binary image has values of 1 (white) for all pixels in the input image with intensity greater than a given level (for representing the presence of

tracer) and 0 (black) for all other pixels. Figure 3.3 shows the original image and the image after binary thresholding.

The binary thresholded image is analyzed to get an estimate of the pixel count corresponding to the tracer content region. The size of the structuring element is chosen such that the slices with lower pixel count are processed in a bigger neighbourhood. This helps in enhancing even the smaller features in the image. At the same time over enhancement of slices with higher tracer region is taken care of by choosing smaller neighbourhood.

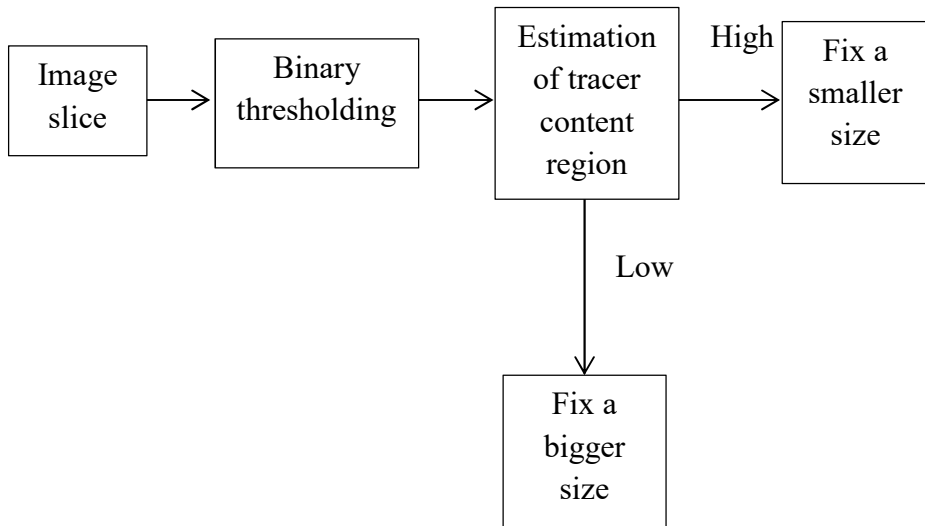


Figure 3.2 Steps in determining the size of structuring element

Algorithm:

For a grey scale image with intensity values in the range from 0 to 255, 159 is chosen as the threshold value to convert it into a binary image. To fix this threshold, short axis and long axis slices of 15 patient cases were analyzed to get the pixel values at blood flow region, myocardial region without blood flow and background. After converting those patient

case images to binary, the number of pixels in the normal and abnormal perfusion slices was analyzed to fix the number threshold.

Step 1: Read the SPECT image.

Step 2: Read the first slice.

Step 3: Check the intensity values of each pixel.

Step 4: If the intensity value is greater than the threshold, change the pixel value to 1; otherwise 0. This binary image gives the tracer content region.

Step 5: Check the number of pixels in the tracer content region.

Step 6: If the number is greater than the number threshold, fix a smaller size for the structural element; otherwise fix a bigger size.

Step 7: Read next slice and go to Step 3.

3.4.2 Morphological processing

Opening and closing are morphological operations that operate on features smaller than the size of the structuring element. Morphological processing is carried out in two stages as shown in figure 3.4.

In the first stage a morphologically opened image slice, denoted by T_{gi-o} , is subtracted from the original image slice to get pixels, denoted by T_{gi-th} , that are removed by opening, as in equation (10) and (11).

$$T_{gi-o} = (T_{gi} \ominus S) \oplus S \quad (10)$$

$$T_{gi-th} = T_{gi} - T_{gi-o} \quad (11)$$

This process extracts light features that are smaller than the structural elements. These pixels are then added to the original image slice to enhance the contrast.

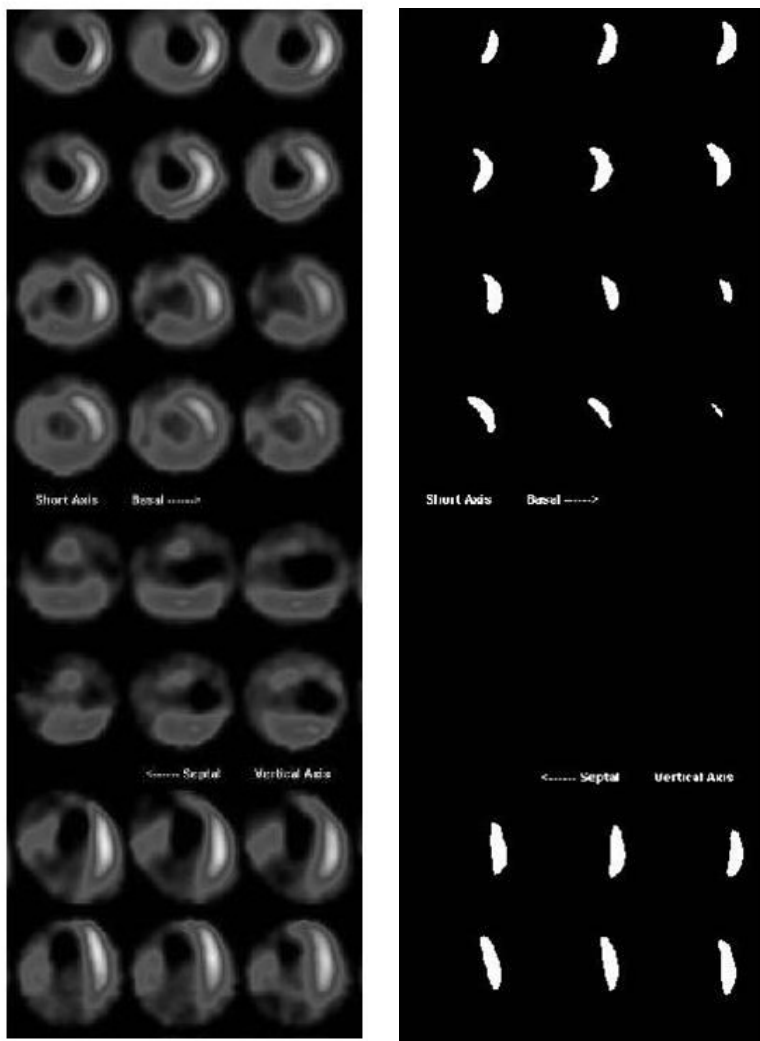


Figure 3.3 SPECT image slices and binary thresholded image slices

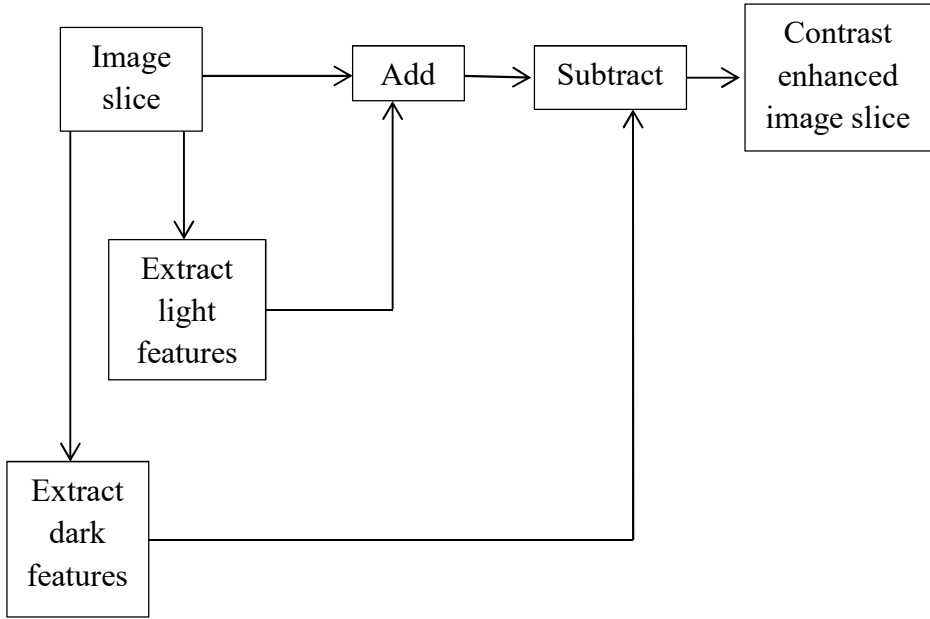


Figure 3.4 Morphological processing

In the second stage the original image slice is subtracted from a morphologically closed image, denoted by T_{gi-c} , to get pixels which represent intensity troughs in the image slice, denoted by T_{gi-bh} .

$$T_{gi-c} = (T_{gi} \oplus S) \ominus S \quad (12)$$

$$T_{gi-bh} = T_{gi-c} - T_{gi} \quad (13)$$

This process extracts dark features which are then subtracted from the contrast enhanced image, as in equations (12) and (13) above.

3.5 Performance measures

- Contrast improvement

Factors like limited number of counts and scatter of photons mainly contribute to the degradation of light features in SPECT images when compared to the dark features. Decreased contrast results in poorer visibility of fine details in the image. Contrast enhancement of such light features helps in improving the quality of images to a great extent. The increase in contrast is measured using Michelson's formula [122] which is considered the best option for the images where dark and light features take up similar fractions of area. Contrast is measured using equation (14).

$$Contrast = \frac{I_{\max} - I_{\min}}{I_{\max} + I_{\min}} \quad (14)$$

I_{\max} is the maximum intensity and I_{\min} is the minimum intensity. Contrast improvement (CI) is calculated using equation (15).

$$CI = \frac{contrast_{enhanced} - contrast_{original}}{contrast_{original}} \quad (15)$$

- Mean square error

This indicates the mean square error (MSE) in the pixel count between the original image and the enhanced image that contributes to the tracer content region. This must give a minimum value to ensure that the quantitative information is preserved.

- Entropy difference

Entropy is a statistical measure of randomness that can be used to characterize the texture of the input image [123]. In order to preserve quantitative information the entropy difference (ED) between the original image and the enhanced image must be a minimum value.

- Structural similarity index measure

Structural similarity index measure (SSIM) is used for assessing the quality of images. It is based on the property of human visual system for identifying the degradation of structural information [124]. SSIM value varies between 0 and 1. The higher the value, the more similar is the enhanced image to the original image in terms of structural information.

- Peak signal to noise ratio

Peak signal to noise ratio (PSNR) is defined as given in equation (16).

$$PSNR = 10 \log \left(\frac{Int_{\max}^2}{MeanSquareError} \right) \quad (16)$$

The maximum intensity in the image is Int_{\max} . The higher the value of PSNR, the better is the quality of the image in terms of signal to noise ratio.

- Blur metric

Blur metric (BM) gives the amounts of difference in blur between the blurred image and the de-blurred image. This measure is based on the discrimination between different levels of blur perceptible on the same image [125]. The lower the value of blur metric, the better is the quality of the image.

3.6 Simulation results

The performance of the proposed method in enhancing cardiac SPECT images has been evaluated qualitatively and quantitatively. Images from Medical trust hospital, Kochi database were used for experimental analysis.

Figure 3.5 shows the SPECT image slices corresponding to low tracer content region and the image slices enhanced using the proposed method. The high tracer content region slices and the enhanced slices are shown in figure 3.6. The resultant image has registered an improvement in terms of its contrast, without loss in information as seen in figure 3.7.

Figure 3.8 shows a cardiac SPECT image showing normal perfusion and the image enhanced using proposed method. Figure 3.7 shows a cardiac image with some abnormality and figure 3.8 shows a cardiac image with normal functioning. The difference lies in the amount of tracer content (shown by bright pixels in the image) present in the myocardium. It is observed that the visual quality of the output image has increased in both normal and abnormal perfusion cases as a result of the application of the proposed image dependent method.

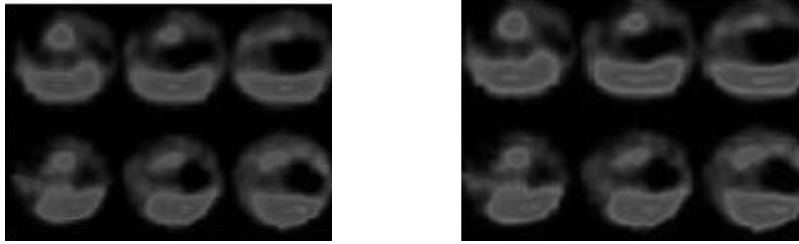


Figure 3.5 Cardiac SPECT image slices (low tracer content region) and the corresponding enhanced slices using the proposed method

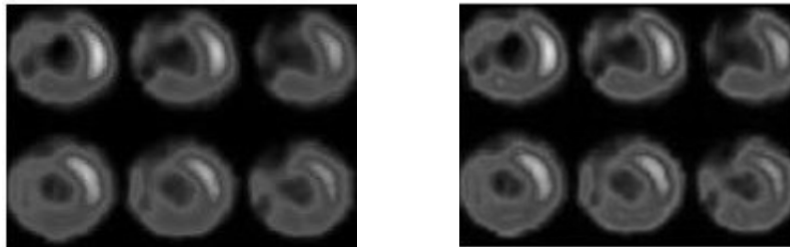


Figure 3.6 Cardiac SPECT image slices (high tracer content region) and the corresponding enhanced slices using the proposed method

Simulations were carried out to evaluate the performance of the proposed scheme quantitatively. Table 3.1 presents the performance measure values for the enhanced images shown in figure 3.7 and figure 3.8.

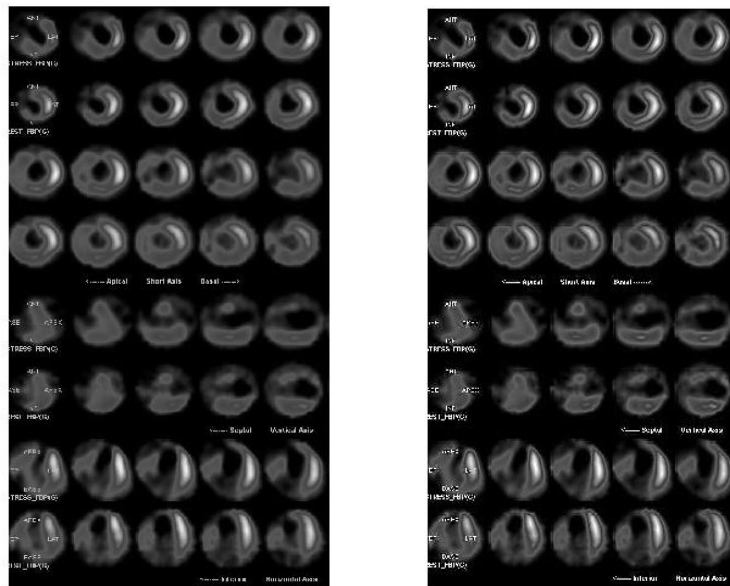


Figure 3.7 An abnormal perfusion SPECT image and SPECT image enhanced using the proposed method

Table 3.1 Performance measure values for the image enhanced using the proposed method

	Normal perfusion image	Abnormal perfusion image
CI	0.4307	0.3799
ED	0.0008	0.0180
MSE	0.0031	0.0019
SSIM	0.9558	0.9822
PSNR	29.9103	33.3124

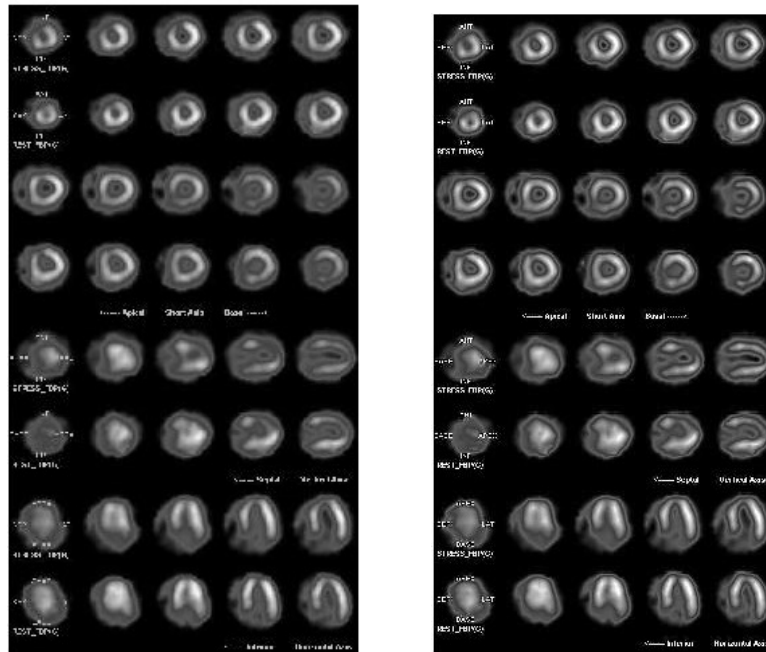


Figure 3.8 A normal perfusion SPECT image and SPECT image enhanced using the proposed method

Tables 3.2, 3.3, 3.4, 3.5, 3.6 and 3.7 show the performance comparison of the proposed method using morphology with other contrast improvement techniques in terms of CI, ED, MSE, SSIM, PSNR and BM respectively. Histogram equalization method [109], CLAHE [115], brightness preserving dynamic fuzzy histogram equalization (BPDFHE) [112], bi-histogram equalization using adaptive sigmoid function (BHEASF) [117] and CLAHE with pre-processing [119] are used for comparison. 40 real cardiac images, taken from 40 different patients under medical diagnosis in Medical trust hospital, were used to prove the efficiency of the proposed method in terms of the performance measures described in section 3.5. 17 patients had normal functioning of the heart and 23 patients had myocardial perfusion defects. 960 x 510 sized images, each with 40 slices were used for the experiments.

Table 3.2 Performance comparison in terms of CI

Method	CI
Histogram equalization	0.4281
CLAHE	0.2503
BPDFHE	0.2366
CLAHE with pre-processing	0.1334
BHEASF	0.1209
Proposed method	0.4071

Table 3.3 Performance comparison in terms of ED

Method	ED
Histogram equalization	0.8288
CLAHE	0.1770
BPDFHE	0.4759
CLAHE with pre-processing	0.0531
BHEASF	0.5441
Proposed method	0.0388

Table 3.4 Performance comparison in terms of MSE

Method	MSE
Histogram equalization	0.7689
CLAHE	0.0148
BPDFHE	0.0178
CLAHE with pre-processing	0.0075
BHEASF	0.0082
Proposed method	0.0013

Table 3.5 Performance comparison in terms of SSIM

Method	SSIM
Histogram equalization	0.1692
CLAHE	0.7485
BPDFHE	0.3861
CLAHE with pre-processing	0.8975
BHEASF	0.9841
Proposed method	0.9802

Table 3.6 Performance comparison in terms of PSNR

Method	PSNR
Histogram equalization	5.1720
CLAHE	26.3131
BPDFHE	23.8213
CLAHE with pre-processing	25.8507
BHEASF	32.9724
Proposed method	31.9325

Table 3.7 Performance comparison in terms of BM

Method	BM
Histogram equalization	0.3033
CLAHE	0.4318
BPDFHE	0.3105
CLAHE with pre-processing	0.4475
BHEASF	0.3967
Proposed method	0.3024

Histogram equalization is a popular and simple contrast improvement technique. Since the enhanced images suffer from visual

artefacts, traditional histogram equalization is unfit for application in medical images [109]. In the case of cardiac SPECT images also, the results proved the same. Even though CI was more for histogram equalization as shown by the values in table 3.2, ED, MSE, SSIM and PSNR values were not satisfactory as shown in tables 3.3, 3.4, 3.5 and 3.6. These measures show that basic information was lost by performing histogram equalization.

Table 3.3 and table 3.4 show that ED and MSE values were less for the proposed method as compared to the other methods. CLAHE with preprocessing also gave comparable values. This emphasizes the information preserving capability of the proposed method.

Even though BHEASF method gave the highest SSIM and PSNR values (0.9841 and 32.9724 respectively), ED and MSE values (0.5441 and 0.0082 respectively) show that information was less preserved by the method. The proposed method gave comparable values for SSIM and PSNR (0.9802 and 31.9325 respectively) while giving least values for ED and MSE (0.0388 and 0.0013 respectively).

The value of BM in table 3.7 reveals that a small amount of blur also got added to the image by all the methods. The proposed method added the lowest level of blur as shown by the BM values. But the added blur did not affect the visual quality of the image as observed in figure 3.9. The edges of the tracer content region were clearly visible for the images enhanced using the proposed method.

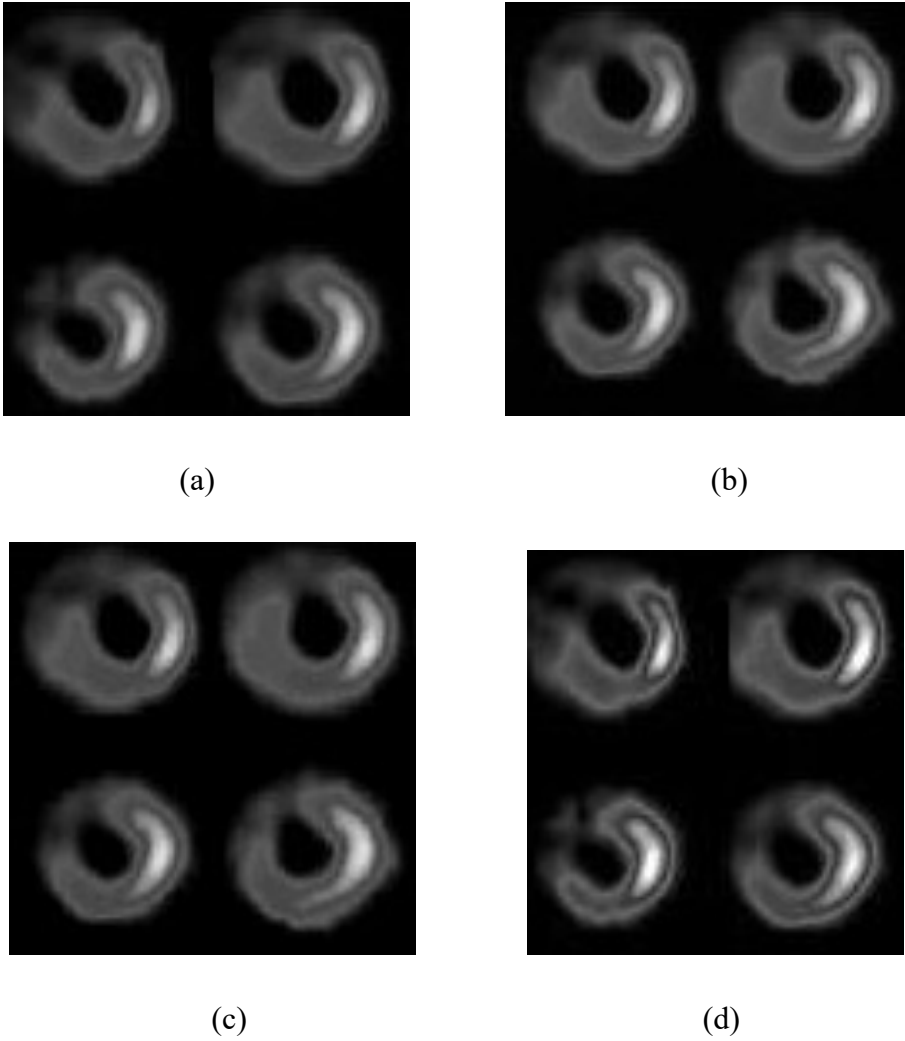


Figure 3.9 (a) Image before enhancement (b) Image enhanced using CLAHE (c) Image enhanced using BHEASF (d) Image enhanced using proposed method

The proposed method, which uses an adaptive neighbourhood for the operation of structuring element, is also compared with the method which uses the same morphological operations and a fixed neighbourhood.

For a fixed neighbourhood of smaller size the information content was preserved but the amount of contrast enhancement was very less. Figure 3.10 shows the comparison between the proposed adaptive neighbourhood method and fixed neighbourhood method in enhancing contrast. A good amount of contrast enhancement was achieved using a larger neighbourhood but with a variation in the information content. The graph is plotted between CI and nth image for 5 images.

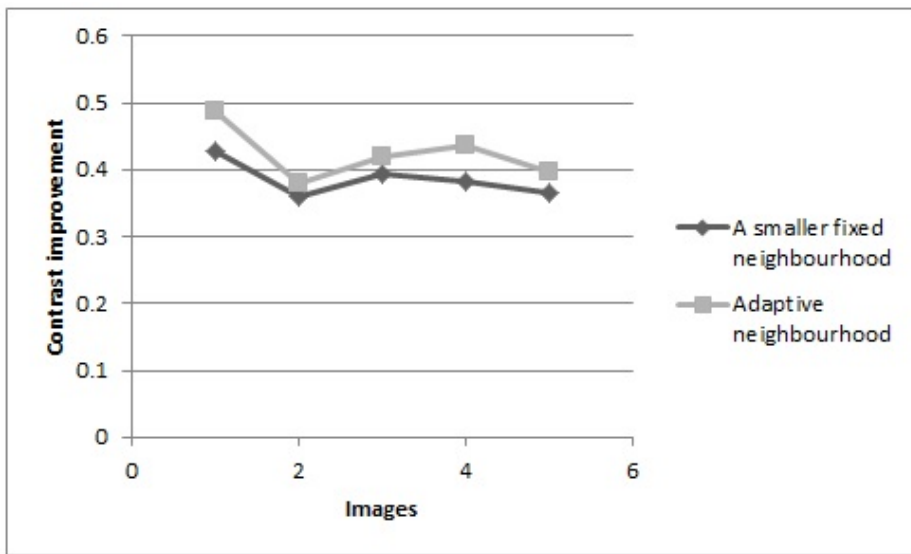


Figure 3.10 Comparison of CI in images enhanced using fixed neighbourhood morphological processing and proposed adaptive neighbourhood method

Figure 3.11, figure 3.12 and figure 3.13 show a comparison between the proposed adaptive neighbourhood method and fixed neighbourhood method in terms of ED, MSE and SSIM. The ED and MSE values were less for the proposed method as compared to the fixed neighbourhood method. The SSIM plot shows that images enhanced using

the proposed adaptive neighbourhood method were structurally more similar to the original image than the images enhanced using a larger fixed neighbourhood. Using adaptive selection of size of the structuring element, a considerably good amount of contrast enhancement was achieved while preserving the information content as indicated by the ED, MSE and SSIM values.

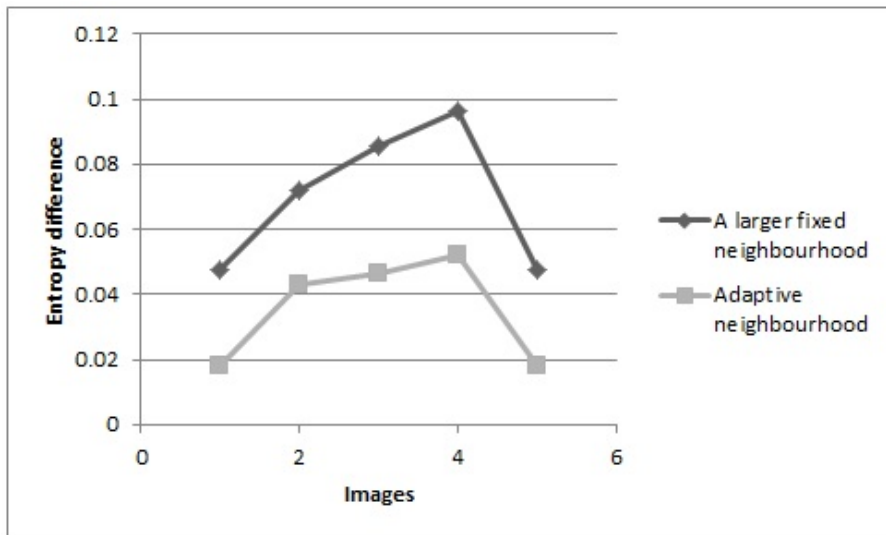


Figure 3.11 Comparison of ED between original image and enhanced using fixed neighbourhood morphological processing and proposed adaptive neighbourhood method

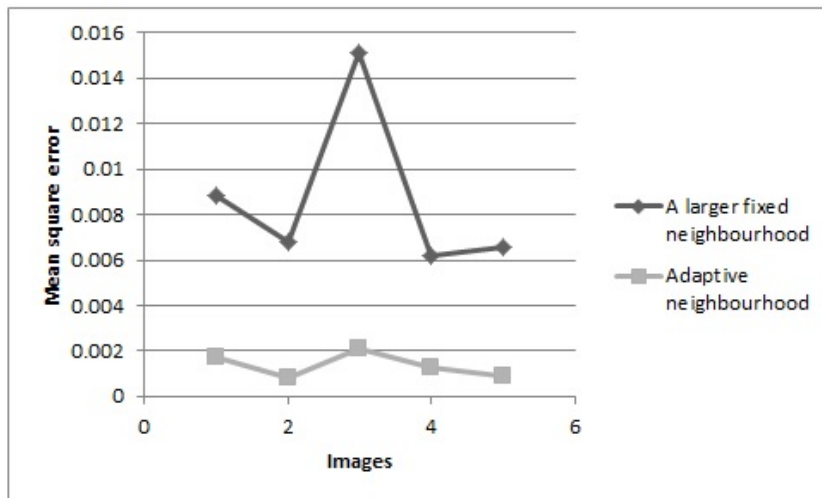


Figure 3.12 Comparison of MSE in images enhanced using fixed neighbourhood morphological processing and proposed adaptive neighbourhood method

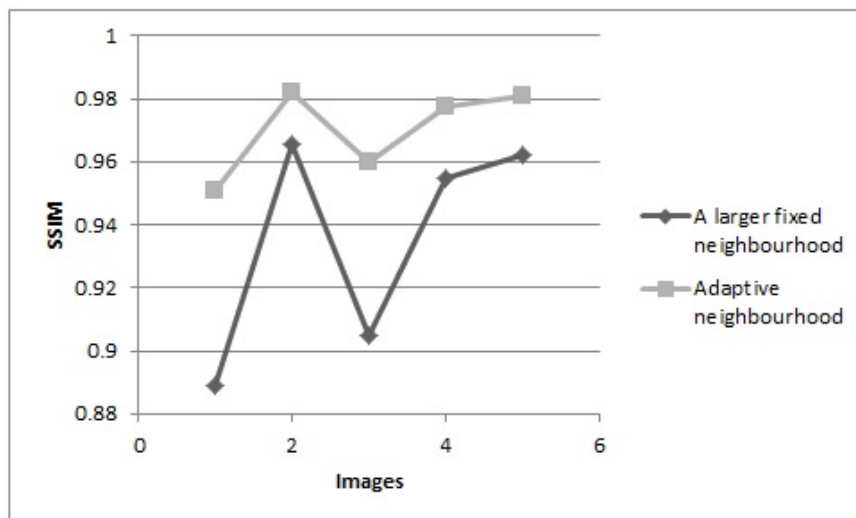


Figure 3.13 Comparison of SSIM in images enhanced using fixed neighbourhood morphological processing and proposed adaptive neighbourhood method

Being a medical image the trueness of the enhanced image is also an important issue to be taken care of. Evaluation for validation of trueness of the enhanced image with respect to the original image was also done for the proposed method. A most commonly reported quantitative measure obtained for cardiac SPECT images is LVEF. LVEF value must not change as a result of enhancement. It is calculated from the volume of blood in the LV, which in turn, is computed from the pixel counts representing tracer content region. If these pixel counts for the enhanced image, stay the same or within a statistical acceptance value the method can be validated for its trueness to the original image data. The statistical method of ‘paired samples t test’ [126] was used to validate the trueness of the enhanced image. The test gave a p value which shows that the null hypothesis can be accepted at 5% significance level. The null hypothesis states that there is no significant difference between the pixel counts corresponding to blood flow in the images before and after enhancement.

3.7 Summary

This chapter presented an image dependent contrast enhancement method for cardiac SPECT images. The type of the image region was analyzed and the size of the structuring element was selected. Morphological operation was carried out subsequently in two stages. Since the size of the structuring element is dependent on the image region, this approach helped to meet the enhancement requirements of different image regions. Performance evaluations of the proposed method with respect to improvement in contrast and retention of original image information were executed on real cardiac images. The effectiveness of the method against the existing comparable techniques was studied. The

experimental results prove that the method enhanced nuclear images retaining their data integrity with quantitative evidence of recording an improvement over other techniques used for comparison.

Chapter 4

ENHANCEMENT OF CARDIAC SPECT IMAGES BY DEBLURRING

This chapter proposes a total variation regularization based blur reduction method for the restoration of blurred cardiac SPECT images. This is achieved in two main stages. A maximum likelihood estimate of the distortion operator or the point spread function is computed from the image region. The number of iterations for maximum likelihood operation is decided by Kolmogorov-Smirnov test so that the noise added is minimal. Then total variation regularization filtering is performed. Pre-filtering is also done to avoid unwanted high frequency drops. The algorithm is tested on real cardiac SPECT images. Quantitative and qualitative evaluations of the algorithm show the potential of proposed algorithm in reducing blur while maintaining high peak signal to noise ratio.

4.1 Introduction

As a nuclear medicine imaging tool, SPECT imaging enjoys a wide acceptance amongst medical fraternity in the diagnosis of cardiac diseases [127]. The distribution of blood flow to the heart muscle can be visually analyzed from a cardiac nuclear image [128, 129]. Of the various factors affecting the diagnostic accuracy of SPECT image, the movement of the patient while image acquisition and scattering of photons during detection [130], induces blur in such type of images.

One of the important issues to be addressed in the area of nuclear medicine image enhancement is image deblurring. A degradation operator makes an original clear SPECT image a blurred one in a SPECT imaging model. The system point spread function (PSF) contributes to the cause of degradation. In the case of SPECT imaging both the PSF and the actual clear image are not known. Image deblurring algorithms are defined by inverse filtering problems which use an estimate of the original image. Blind image de-convolution aims at the reconstruction of original image without using any prior information [131, 132]. In the case of SPECT images where little prior information is available, it can turn out to be more relevant to use blind deconvolution algorithms for estimating the original image from the blurred image.

4.2 Literature survey

Literature presents many methods to improve the quality of nuclear medicine images through deblurring. There are mainly two categories of such methods: methods using restoration algorithms during

the reconstruction process, and methods where the algorithm is performed on the reconstructed images. The point spread function is modeled using the system parameters and the restoration algorithm uses this model in the first category [133]. The second category makes use of image processing techniques [134].

The performances of four widely used filters were compared for enhancing myocardial ^{99m}Tc -sestamibi SPECT perfusion images by Rajabi et al. [81]. A non-negativity support constraints recursive inverse filtering algorithm was proposed by Kundur and Hatzinakos [135] and it was extended to the 3D SPECT imaging restoration context in [134]. Bayesian tomographic reconstruction methods incorporating structural information were utilized by the authors in [136] and [137]. In [138] the blur transfer function for a SPECT image was approximated with a two dimensional symmetric Gaussian function to improve the image quality. An analysis of blind deconvolution algorithms was presented in [139]. In [140] a two-step iterative shrinkage and thresholding algorithm was proposed, exhibiting a faster convergence rate. A deconvolution method suitable for nuclear imaging was derived in [141]. The method utilized maximum likelihood estimation with expectation maximization algorithm [142]. A blind deconvolution algorithm based on Lucy Richardson algorithm [143, 144] was presented in [145].

The image before blurring and the PSF are totally unknown in the case of SPECT images. So one solution for deblurring, is to use blind deconvolution. The advantage is that it is simple. But noise will get added to the image which we cannot afford in SPECT images. The presence of noise may lead to a wrong decision in computer aided diagnosis. Regularized filtering can be a useful tool in this scenario. The proposed

method combines blind deconvolution and regularized filtering incorporating total variation denoising.

4.3 Blur model in SPECT imaging

A linear space invariant image degradation model is shown in figure 4.1. The blurred image $b(x, y)$ can be written as given in equation (1).

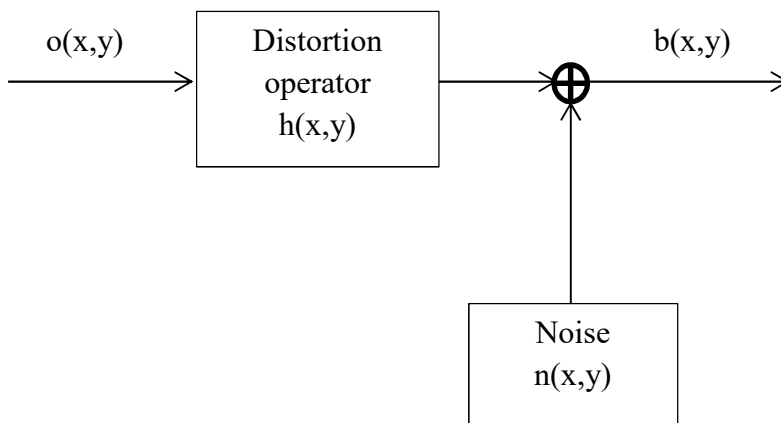


Figure 4.1 Image blurring model

The original clear image is represented by $o(x, y)$, the system transfer function or the PSF is represented by $h(x, y)$ and $n(x, y)$ represents the noise.

$$b(x, y) = o(x, y) * h(x, y) + n(x, y) \quad (1)$$

The blurred image is obtained by the convolution between the original image and the point spread function as in equation (1). In a noisy system, noise also gets added to it.

4.4 De-blurring methods

Since the blurring model involves convolution, deblurring turns out to be a de-convolution problem. Different approaches were proposed in literature in this regard including blind deconvolution, Lucy-Richardson (LR) algorithm and least squares filtering [146, 147].

4.4.1 Blind de-convolution

As figure 4.1 suggests, image deblurring is an inverse problem. It can guarantee better results if prior information about the true image and the degradation factor is available and used to obtain the true image. But practically in most cases, including medical images, the true image and the degradation factor are totally or partially unknown. The problem then becomes blind deconvolution. So the original image $f(x, y)$ can be found out by the method of blind deconvolution without using the exact degradation factor or point spread function.

It hence follows that the discrete model of equation (1) can be written as given in equation (2) below.

$$b(X) = \sum_{s \in S_h} h(X, s) o(s) + n(X); X = (x, y) \in S_o \quad (2)$$

S_o is the support of the image and S_h is the support of PSF. The problem of blind deconvolution becomes finding an estimate of the true image from an initial guess on the image and the point spread function.

If a Bayesian framework is used to define blind deconvolution, all parameters are regarded as unknown stochastic quantities with respective probability distributions. The probability of the observed blurred image is

$p(b)$. The probability of the true image is $p(o)$. The likelihood function for the random process defined by equation (1) is denoted by $p(b/o, h, n)$.

4.4.2 Lucy Richardson algorithm

A potentially better approach for image deblurring is LR algorithm proposed by Richardson [143] and Lucy [144]. LR algorithm is an iterative method that maximizes the likelihood function, assuming Poisson statistics [143, 144]. In [148] this was described as given in equation (3).

$$p(b/o) = \prod_{x,y} \frac{(h * o)^b e^{-(h * o)}}{b!} \quad (3)$$

Equation (3) is maximized by minimizing the log likelihood function given in equation (4)

$$-\log(p(b/o)) = \iint_{x,y} [(h * o) - b \log(h * o) + \log(b!)] dx dy \quad (4)$$

$\log(b!)$ is a constant relative to o . So minimizing equation (4) reduces to minimizing equation (5).

$$F(o) = \iint_{x,y} [(h * o) - b \log(h * o)] dx dy \quad (5)$$

The function given in equation (5) is minimized by setting its derivative to zero. At convergence the iteration step is defined as in equation (6).

$$\hat{o}^{p+1} = \hat{o}^p \left[\frac{h * \frac{b}{\hat{o}^p}}{h * \hat{o}^p} \right] \quad (6)$$

\hat{o}^{p+1} is the estimate of the true image at $(p+1)^{\text{th}}$ iteration, \hat{o}^p is the estimate of the true image at p^{th} iteration, and h^* represents the conjugate transpose of h . The method is effective for a known initial PSF.

4.4.3 Least square filtering

Constrained least squares filtering is a well-established linear restoration approach in image processing [149]. The linear degradation model in figure 4.1 can be expressed in vector form as in equation (7).

$$b = Ho + n \quad (7)$$

The optimality of restoration is based on a measure of smoothness. A criterion function defined by a smoothing operator is minimized subjected to the constraint as defined by equation (8).

$$\left\| b - H \hat{o} \right\|^2 = \|n\|^2 \quad (8)$$

Using Laplacian operator as smoothing operator, the criterion function is given in equation (9).

$$C = \sum_{x=0}^{M-1} \sum_{y=0}^{N-1} \nabla^2 o(x, y) \quad (9)$$

Equation (10) is the frequency domain solution to this optimization problem.

$$\hat{O}(u, v) = \left[\frac{H^*(u, v)}{|H(u, v)|^2 + \gamma |P(u, v)|^2} \right] B(u, v) \quad (10)$$

γ is a parameter that must be adjusted in order to satisfy the constraint.
 $P(u,v)$ is the regularization operator.

4.5 Proposed method

A method has been proposed for deblurring cardiac SPECT images by combining blind deconvolution and regularized filtering incorporating total variation denoising. A maximum likelihood (ML) estimate of PSF is obtained using blind deconvolution principles. A better estimate of the original image is obtained using the estimated PSF through regularized total variation based least square filtering [150]. The block diagram of the proposed method is shown in figure 4.2.

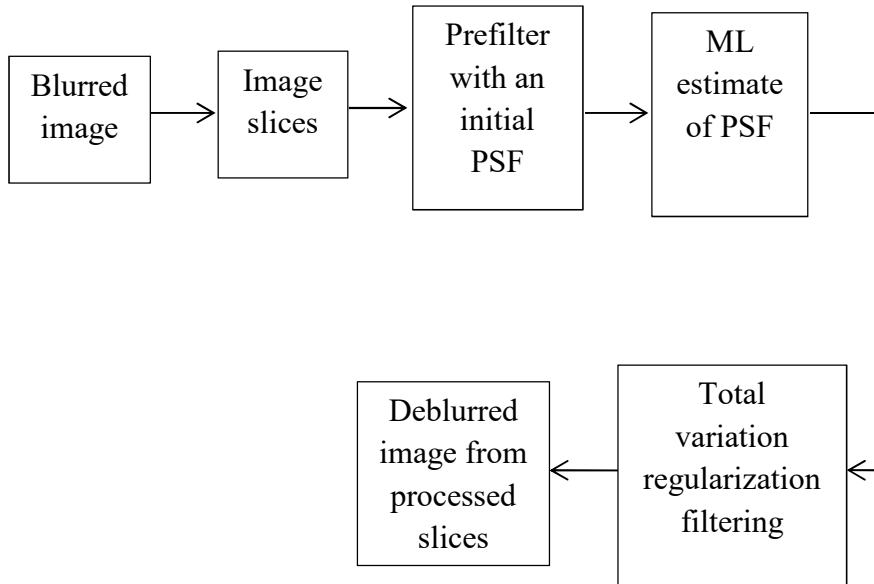


Figure 4.2 Block diagram of the proposed method

4.5.1 Prefiltering

Maximum likelihood estimation algorithm is implemented using Discrete Fourier Transform (DFT), which may introduce ringing effect. Pre-filtering is done to reduce this effect. Ringing effect is caused due to the presence of high frequency drop-off at the edges. To remove high frequency drop-off, the entire image is blurred and the pixels in the region other than edges are replaced with that of the original image. Then a weighted sum of the original image and its blurred version is taken. The autocorrelation function of the PSF is used for determining the weighting array. The prefiltered image is the same as the original image in the region without sharp intensity changes. The prefiltered image is equal to its blurred version near the edges where ringing effect can occur.

4.5.2 Maximum likelihood estimation of the PSF

Blind image deconvolution techniques differ in the assumptions made on the original image and the point spread function. One method is to compute the maximum likelihood estimate of the PSF parameters to perform blind deconvolution. Maximum likelihood estimation uses the fundamental Bayesian principle that regards all parameters as unknown stochastic quantities with assigned probability distributions. The probability of the observed blurred image is $p(b)$. The probability of the original image is $p(o)$. The likelihood function for the random process defined by figure 4.1 is denoted by $p(b/o,h,n)$. The maximum likelihood solution maximizes $p(b/o,h,n)$ over o,h,n as implied below in equation (11).

$$\{o_{ML}, h_{ML}, n_{ML}\} = \arg \max_{o,h,n} p(b/o, h, n) \quad (11)$$

o_{ML} , h_{ML} , n_{ML} denote the maximum likelihood estimate of the original image o , PSF h and noise n .

With an initial guess on PSF and the original image, the maximum likelihood estimate of the PSF is obtained. The steps are given in figure 4.3.

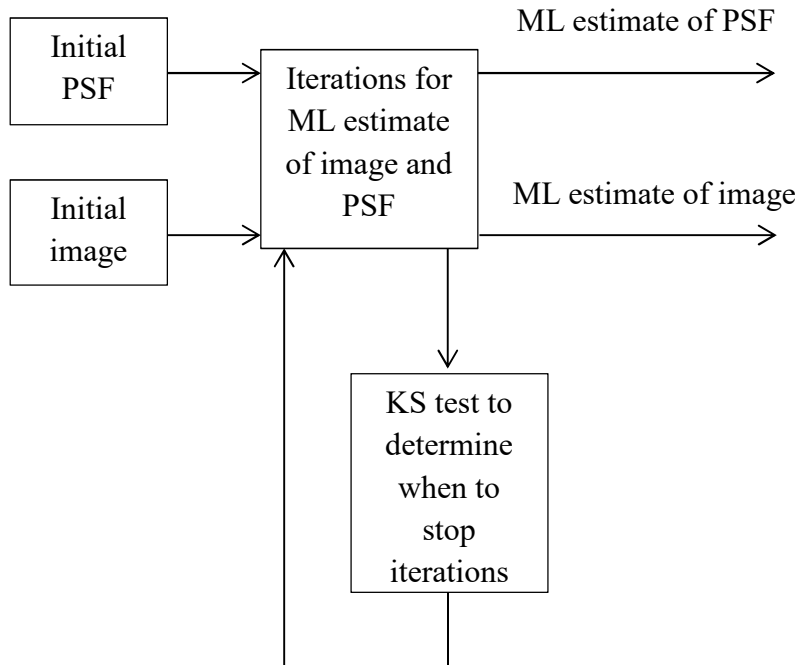


Figure 4.3 Estimation of PSF and image

- Step 1: An initial value is assigned for the PSF. For a heart slice of size 120x100, an arbitrary size of 5x5 is chosen for the initial PSF as mentioned in equation (12) below.

$$\hat{h}^{(initial)}(x, y) = \text{ones}(\text{arbitrarysize}) \quad (12)$$

- Step 2: An initial value is assigned for the original image. Usually in blind image deconvolution, the observed blurred image itself acts as the initial estimate of the original image as indicated in equation (13).

$$\hat{o}^{(initial)}(x, y) = b(x, y) \quad (13)$$

- Step 3: Maximum likelihood estimate of the PSF is computed iteratively. Estimate of the original image, $\hat{o}^{p+1}(x, y)$, and the estimate of PSF, $\hat{h}^{p+1}(x, y)$, in $(p+1)^{th}$ iteration from the estimates in p^{th} iteration is given in equations (14) and (15).

$$\hat{o}^{p+1}(x, y) = \hat{o}^p(x, y) \left[\frac{\hat{h}^p(x, y)^* * b(x, y)}{\hat{h}^p(x, y)^* * \hat{o}^p(x, y)} \right] \quad (14)$$

$$\hat{h}^{p+1}(x, y) = \hat{h}^p(x, y) \left[\frac{b(x, y)}{\hat{h}^p(x, y)^* * \hat{o}^p(x, y)} * b(x, y)^* \right] \quad (15)$$

- Non negativity constraints are applied on $\hat{o}^{p+1}(x, y)$ and $\hat{h}^{p+1}(x, y)$ in each iteration step.
- The number of iteration P is decided by performing Kolmogorov-Smirnov (KS) test. As the number of iterations increases the estimate of PSF $\hat{h}(x, y)$ becomes more similar to the original PSF $h(x, y)$. But at the same time more noise gets introduced in the estimate of original image. KS test is performed on the estimates

of original image obtained in two consecutive iterations and ensured that they remain in the same continuous distribution. This is performed in each step and the iterations are stopped when the KS test fails.

- $\hat{h}^P(x, y)$ obtained in the P^{th} iteration gives the ML estimate of the PSF.

4.5.3 Total variation regularization based deconvolution

The deconvolution algorithms discussed in section 4.4 may introduce noise into the image while performing de-blurring iterations. But total variation (TV) regularization based deconvolution is remarkably effective in removing blur from the image with minimum addition of noise [151]. TV based method is introduced by Rudin, Osher and Fatemi [152] which uses an L1 norm. The homogeneous regions are smoothed while preserving the edges.

The TV minimization problem is defined in equation (16).

$$\min_o \frac{\mu}{2} \|Ho - b\|^2 + \|o\|_{TV} \quad (16)$$

μ is the regularization parameter. $\|\cdot\|^2$ is the conventional vector 2 norm square and $\|\cdot\|_{TV}$ is the isotropic TV norm given in equation (17).

$$\|o\|_{TV} = \sum_{x=1}^M \sum_{y=1}^N \sqrt{\|D_x o\|^2 + \|D_y o\|^2} \quad (17)$$

$D_X o$ and $D_Y o$, as defined in equations (18) and (19), are the spatial difference operators along the horizontal and vertical directions.

$$D_X o = o(x+1, y) - o(x, y) \quad (18)$$

$$D_Y o = o(x, y+1) - o(x, y) \quad (19)$$

TV norm of o is approximated as norm of Do . Using an intermediate variable u equation (16) is transformed to equation (20).

$$\begin{aligned} \min_{o,u} \frac{\mu}{2} \|Ho - b\|^2 + \|u\|_2 \\ \text{subject..to..} u = Do \end{aligned} \quad (20)$$

The augmented Lagrangian of the above mentioned problem is given in equation (21).

$$L(o, u, \lambda) = \frac{\mu}{2} \|Ho - b\|^2 + \|u\|_2 - \lambda^T (u - Do) + \frac{\rho_r}{2} \|u - Do\|^2 \quad (21)$$

$\|u - Do\|^2$ is the quadratic penalty term with ρ_r as the regularization parameter. λ , defined in equation (22) is the Lagrange multiplier associated with the constraint $u=Do$. u is defined in equation (23).

$$\lambda = [\lambda_x^T \quad \lambda_y^T] \quad (22)$$

$$u = [u_x^T \quad u_y^T] \quad (23)$$

In [149] the solution to this problem is given as in equation (24).

$$\hat{o} = F^{-1} \left[\frac{F[\mu H^T b + \rho_r D^T u - D^T \lambda]}{\mu |F[H]|^2 + \rho_r (|F[D_x]|^2 + |F[D_y]|^2)} \right] \quad (24)$$

\hat{o} is the estimate of the original image o .

The variance of the blurred image and the variance of the ML estimate of the original image obtained from the method described in section 4.5.2 are computed. The difference between the computed variances is used as the initial penalty parameter for $\|Ho-b\|$. The ML estimate of PSF obtained using the method described in section 4.5.2 is used as H in equation (24). To avoid ringing effect introduced by DFT, prefiltering described in section 4.5.1 is performed prior to total variation regularization filtering.

4.6 Simulation results

This section presents the results of applying the proposed method on blurred cardiac SPECT images. The deblurring algorithm is directly applied on the blurred image, without using any denoising technique or contrast enhancement. There are many reasons for the presence of blur in cardiac SPECT images including photon scattering and movement in the patient created by his act of respiration. As implied by central limit theorem, the blurred version of an image is obtained by the convolution of original image with a Gaussian PSF. To evaluate the performance of the proposed method, cardiac SPECT images blurred using Gaussian PSF are used. Images degraded with different levels of blur are considered. The method is evaluated qualitatively by visual analysis. The performance measures used for quantitative evaluation are PSNR, BM, SSIM and image enhancement factor (IEF). The ratio of the squared difference between original image and noisy image to the squared difference between original image and de-noised image is taken as image enhancement factor. The edge preserving capability of the enhancement

method is reflected in the IEF value. The higher the value of IEF, the better is the quality of images.

Figure 4.4, figure 4.5 and figure 4.6 show four slices of the images degraded at different levels of blur and the images de-blurred using the proposed method.

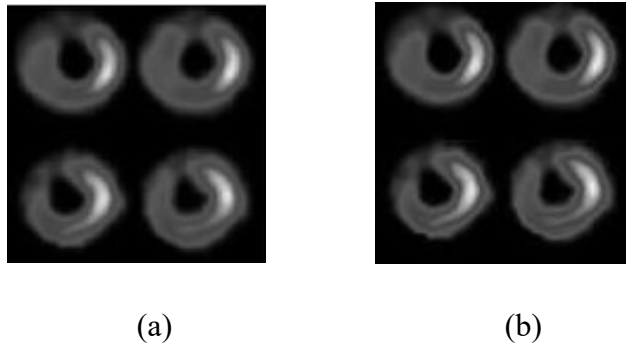


Figure 4.4 (a) Cardiac SPECT image blurred using a Gaussian PSF with $\sigma=3$ and (b) Deblurred image using the proposed method

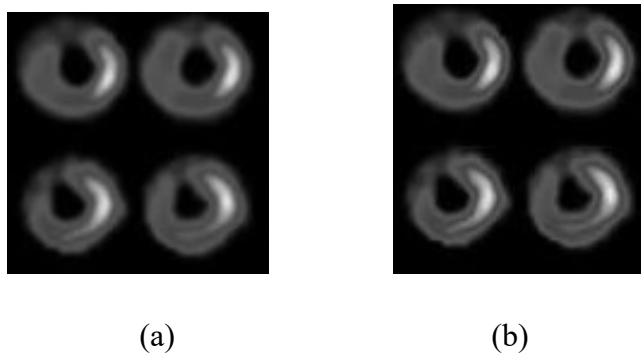


Figure 4.5 (a) Cardiac SPECT image blurred using a Gaussian PSF with $\sigma=5$ and (b) Deblurred image using the proposed method

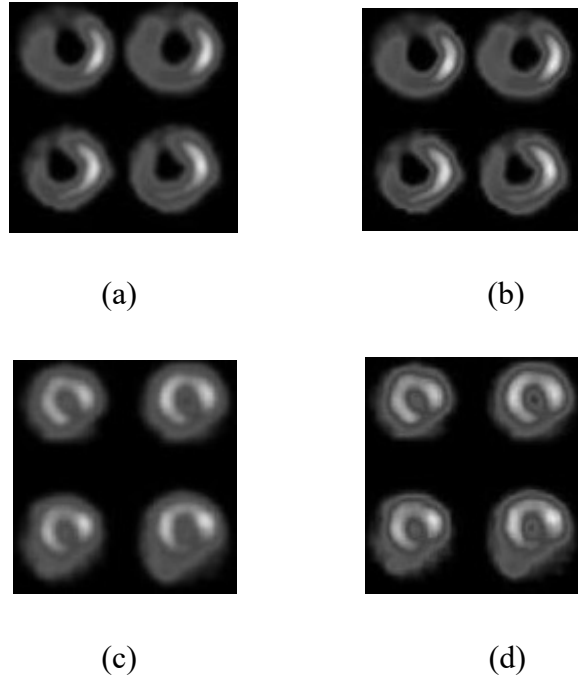


Figure 4.6 (a) Cardiac SPECT image blurred using a Gaussian PSF with $\sigma=7$ (b) Deblurred image using the proposed method (c) Normal blurred image (d) Deblurred image

In figure 4.6 both normal and abnormal case images are displayed. They differ in the amount of tracer content. The algorithm worked well in both cases. The images were taken from Medical trust hospital, Kochi database. Figure 4.7 shows the deblurred image using blind deconvolution and the proposed method.

Simulations have been carried out to evaluate the performance of the proposed deblurring technique using TV regularization. 40 real cardiac images, taken from 40 different patients under medical diagnosis in Medical trust hospital, were used to prove the efficiency of the proposed method in terms of the performance measures. 17 patients had normal functioning of the heart and 23 patients had myocardial perfusion

defects. 960 x 510 images, each with 40 slices were used for the experiments. The superior performance of the proposed method over other de-blurring techniques was also proved. Blind deconvolution, LR algorithm and TV regularization techniques were used for performance comparisons given in table 4.1, table 4.2 and table 4.3.

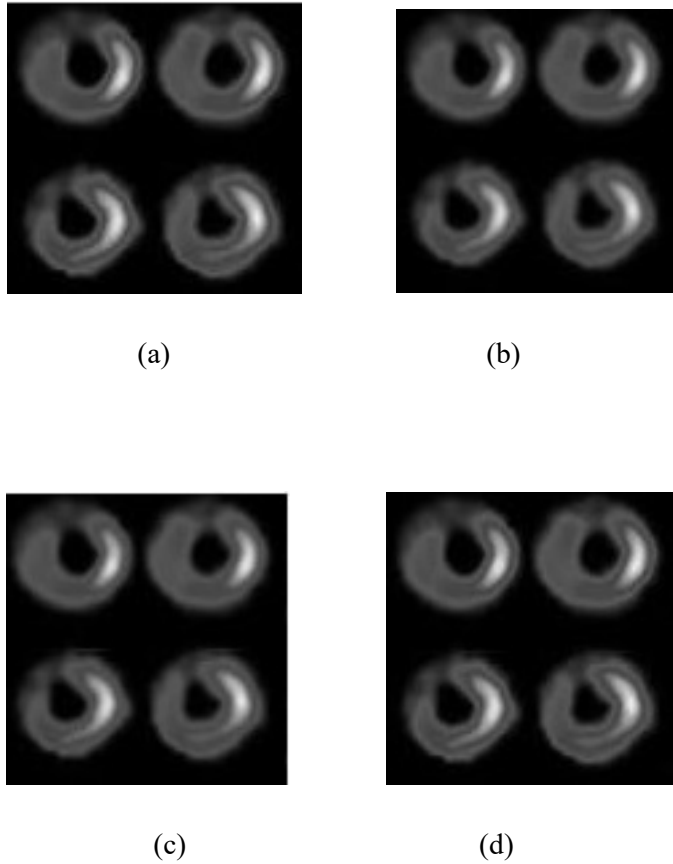


Figure 4.7 (a) Original image (b) Blurred image (c) Deblurred using blind deconvolution algorithm and (d) Deblurred using proposed method

Table 4.1 PSNR, SSIM, BM and IEF values for various deblurring techniques applied on cardiac SPECT images blurred with a Gaussian PSF of sigma=3

Performance measures	Blind deconvolution	LR	TV	Proposed method
PSNR	26.6744	5.8115	5.6433	29.3377
SSIM	0.9437	0.3582	0.3650	0.9608
BM	0.7031	0.5940	0.6702	0.5517
IEF	1.1038	0.0090	0.0087	2.0381

Table 4.2 PSNR, SSIM, BM and IEF values for various deblurring techniques applied on cardiac SPECT images blurred with a Gaussian PSF of sigma=5

Performance measures	Blind deconvolution	LR	TV	Proposed method
PSNR	26.5755	5.8040	4.7491	29.6733
SSIM	0.9416	0.3577	0.3372	0.9636
BM	0.7055	0.5956	0.6628	0.5503
IEF	1.1175	0.0094	0.0055	2.2805

Table 4.3 PSNR, SSIM, BM and IEF values for various deblurring techniques applied on cardiac SPECT images blurred with a Gaussian PSF of sigma=7

Performance measures	Blind deconvolution	LR	TV	Proposed method
PSNR	26.5484	5.8018	5.3674	29.7429
SSIM	0.9410	0.3575	0.3651	0.9641
BM	0.7061	0.5959	0.6723	0.5494
IEF	1.1213	0.0094	0.0091	2.3397

Both blind deconvolution and the proposed algorithm reduced blur present in the image and preserved the basic image information as well. The values in table 4.1, table 4.2 and table 4.3 prove the superior performance of the proposed method over blind deconvolution method.

LR algorithm and TV regularization algorithm suit well for known PSF cases. But in the case of cardiac SPECT image, PSF is totally unknown. Though these methods reduce blur present in the image as shown by BM values, the basic structural information and the overall image quality is not preserved as indicated by the PSNR, SSIM, and IEF values in Table 4.1. Table 4.2 and table 4.3 display the values of performance measures obtained for different levels of blur. The values reflect the remarkable performance of the proposed algorithm as compared to other deblurring algorithms.

MPI from Spectrum dynamics medical case studies [103] were also used for experimental analysis. The images were blurred with three different levels of Gaussian blur. Deblurring techniques using blind deconvolution and proposed method were applied. The improved performance of the proposed method over blind deconvolution in reducing blur while retaining the structural information and overall image quality for different levels of blur is shown in table 4.4, table 4.5 and table 4.6.

Table 4.4 PSNR, SSIM, BM and IEF values for various deblurring techniques applied on MPI Spectrum dynamics case study images blurred with a Gaussian PSF of $\sigma=3$

	PSNR	SSIM	BM	IEF
Blind deconvolution	39.3187	0.9815	0.5087	2.3154
Proposed method	43.6679	0.9912	0.4061	3.3030

Table 4.5 PSNR, SSIM, BM and IEF values for various deblurring techniques applied on MPI Spectrum dynamics case study images blurred with a Gaussian PSF of sigma=5

	PSNR	SSIM	BM	IEF
Blind deconvolution	38.7591	0.9792	0.5196	2.1956
Proposed method	43.5654	0.9917	0.4202	3.6403

Table 4.6 PSNR, SSIM, BM and IEF values for various deblurring techniques applied on MPI Spectrum dynamics case study images blurred with a Gaussian PSF of sigma=7

	PSNR	SSIM	BM	IEF
Blind deconvolution	38.6142	0.9786	0.5222	2.1675
Proposed method	43.5322	0.9917	0.4230	3.7260

Shepp and Vardi [141] used maximum likelihood solutions to modify LR algorithm for nuclear imaging problems. LR algorithm is

performed with the PSF estimated using the method described in section 4.5.2 and the performance was compared with that of the proposed method. Figure 4.8, figure 4.9, figure 4.10 and figure 4.11 show the performance comparison in terms of PSNR, SSIM, BM and IEF. The performance charts reveal that the proposed algorithm has improved the quality of image in comparison with LR method using ML estimate of PSF.

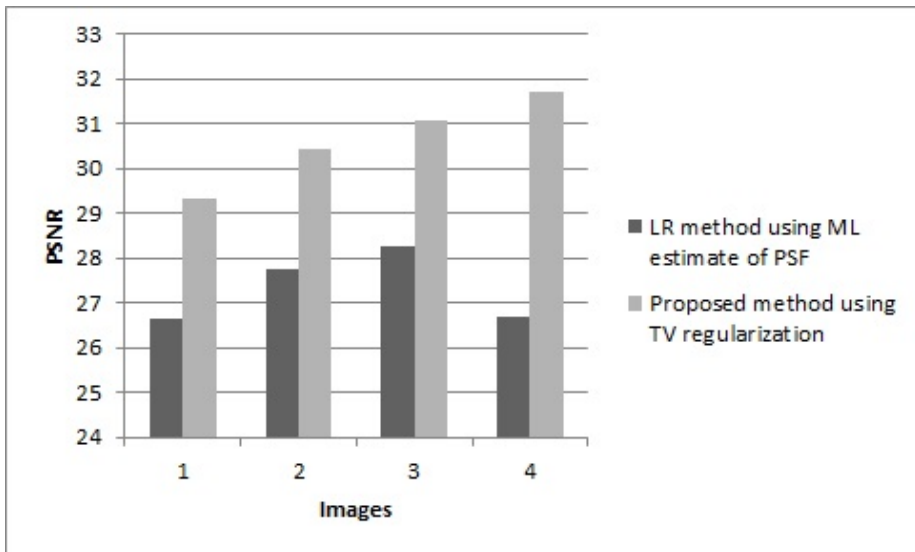


Figure 4.8 Performance comparison between proposed method and LR method using ML estimate of PSF in terms of PSNR

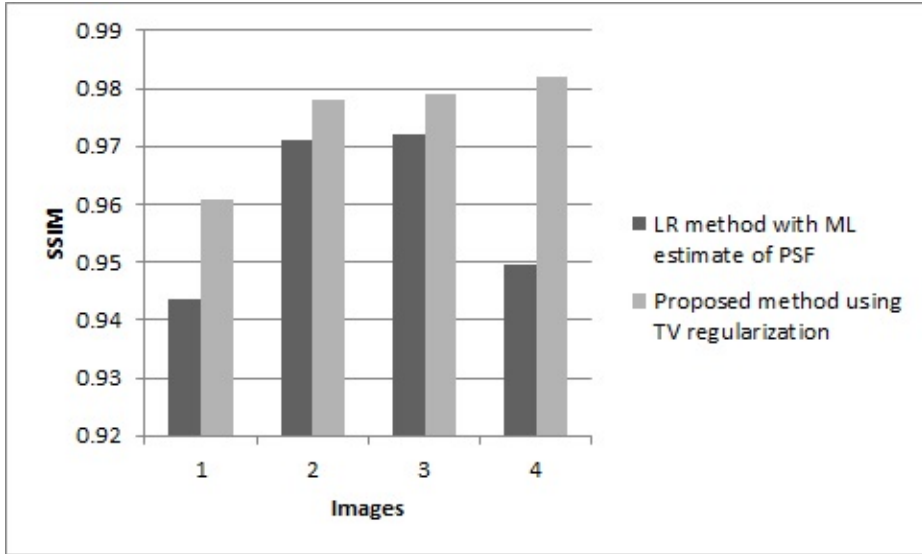


Figure 4.9 Performance comparison between proposed method and LR method using ML estimate of PSF in terms of SSIM

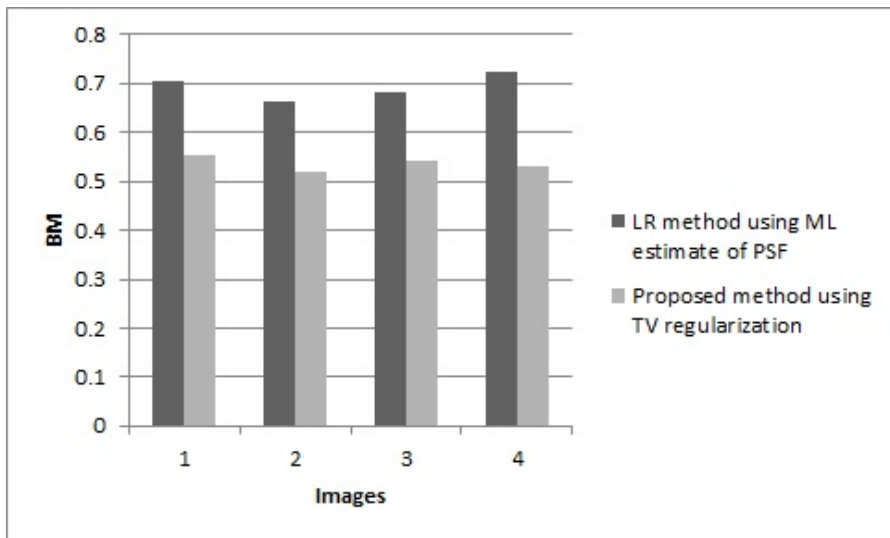


Figure 4.10 Performance comparison between proposed method and LR method using ML estimate of PSF in terms of BM

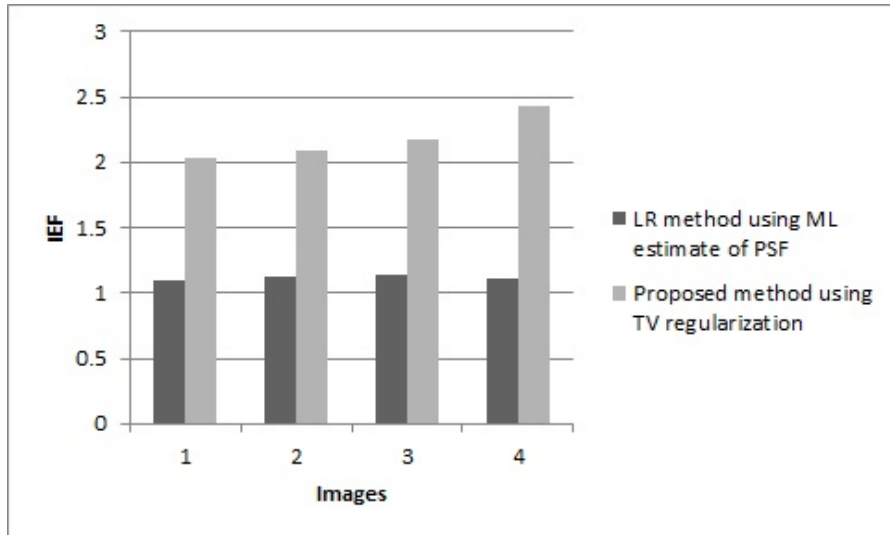


Figure 4.11 Performance comparison between proposed method and LR method using ML estimate of PSF in terms of IEF

Constrained least square filtering is another popular restoration technique used in image processing [153]. The method can be applied for blur reduction with the estimated PSF. A constrained least square filtering is performed using the ML estimate of PSF obtained in section 4.5.2 without incorporating the idea of total variation regularization. The performance comparison is given in figure 4.12, figure 4.13, figure 4.14 and figure 4.15. The results show that the proposed algorithm has achieved an improvement in image quality and blur reduction over constrained least square filtering method using estimated PSF.

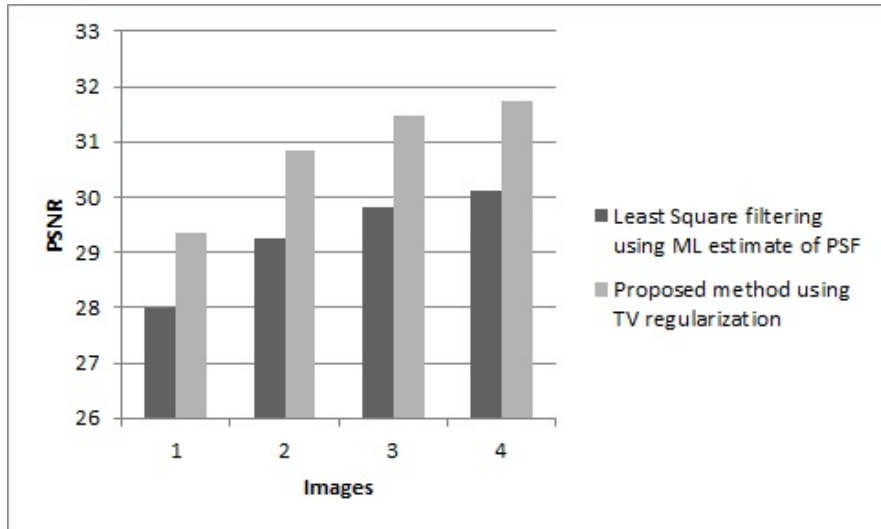


Figure 4.12 Performance comparison between proposed method and least square filtering method using ML estimate of PSF in terms of PSNR

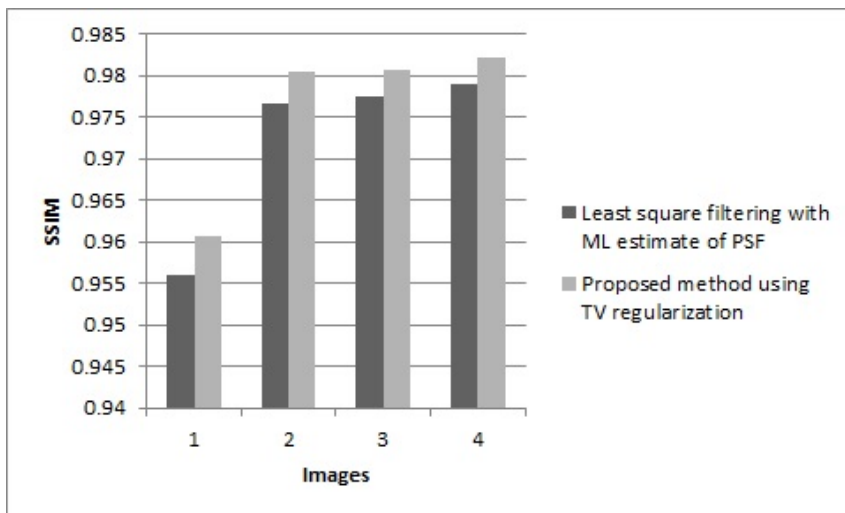


Figure 4.13 Performance comparison between proposed method and least square filtering method using ML estimate of PSF in terms of SSIM

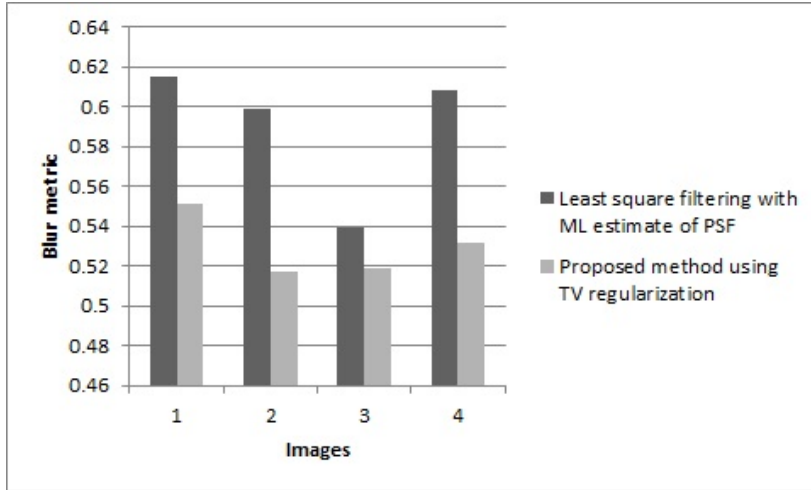


Figure 4.14 Performance comparison between proposed method and least square filtering method using ML estimate of PSF in terms of blur metric

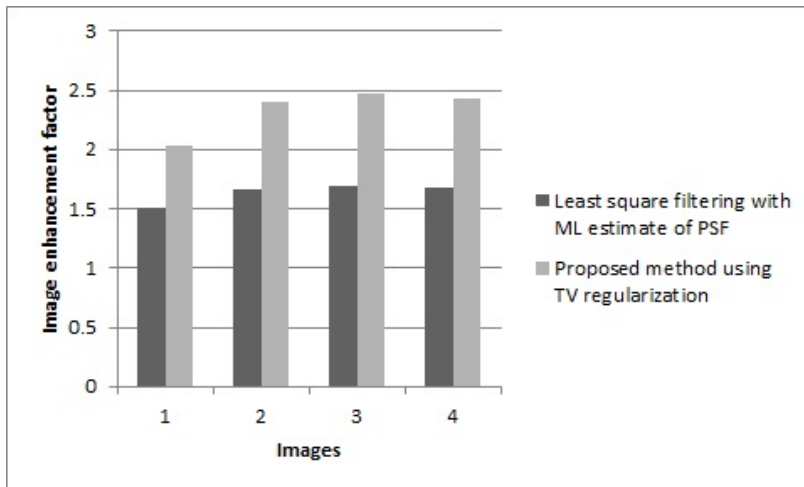


Figure 4.15 Performance comparison between proposed method and least square filtering method using ML estimate of PSF in terms IEF

4.7 Summary

This chapter described a deblurring method suitable for cardiac SPECT images. Deblurring is achieved in two steps. In the first step, a

maximum likelihood estimate of the PSF is computed from the blurred image slices using blind deconvolution principles. The total variation based regularization is performed in the next step to get a better estimate of the original image slice by making use of the ML estimate of the PSF. Contrast is reduced by an average factor of 8 percent but the visual quality is not getting affected as shown by the output images. The proposed method resulted in better output images compared to other deblurring techniques as proved by the visual analysis, PSNR, SSIM, BM and IEF values.

Chapter 5

ENHANCEMENT OF CARDIAC SPECT IMAGES BY DENOISING

This chapter deals with variance stabilization based noise reduction method suitable for cardiac SPECT images. A variance stabilizing transformation is applied on the noisy image so that Poisson noised image is converted into an approximate additive noise distributed image. De-noising is achieved in the transformed domain using the filter transfer function that is estimated based on the local image statistics in the transformed domain. The image is then converted back into the original domain using an inverse transform. The simulation results show that the proposed method gives better de-noising results in terms of qualitative and quantitative performance measures.

5.1 Introduction

In a broad area of applications including medical imaging [154], astronomical imaging [155] and fluorescence microscopy [156], the images are corrupted by Poisson noise. Poisson noise reduction rather than Gaussian noise reduction is a challenging problem. This is due to the pixel intensity dependence nature of Poisson noise. Research is in progress in designing methods to reduce Poisson noise. Various methods have been proposed to reduce Poisson noise in images but a proven algorithm for a particular type of application may fail in giving good results for another type of application, especially in medical images which require high image quality for identifying unique events.

Nuclear medicine imaging uses photons emitted by the radioactive material injected into the human body to form an image. SPECT image, that applies nuclear medicine imaging principles, is developed as a powerful tool in the diagnosis of cardiac ailments [157]. Cardiac SPECT image makes a visual inspection of cardiac blood flow possible. But due to the stochastic nature in the detection of photons these images are usually corrupted by noise. Since the process involves radioactive decay, the noise in SPECT image is modelled as Poisson noise [158].

5.2 Literature survey

Literature presents many methods to denoise images corrupted with Poisson noise. Both linear and nonlinear filters were proposed for this purpose and it is well established that many linear filters could blur the image while reducing noise [120]. Non-linear filters were also used due to their edge preserving capabilities compared to linear filters. Due to its good denoising ability and computational efficiency, the median filter

became a popular non-linear filter [159]. The median filter replaces the pixel value with the median value computed from an M-by-N neighborhood. It is particularly useful in reducing impulse noise.

Different attempts have been done by the researchers to reduce noise in nuclear images. Linear and nonlinear filters were used in the beginning but resulted in edge smoothing and contrast degradation [158]. Nonstationary filters were proposed to overcome this difficulty [160] but resulted in difference in texture from that of the original image.

Various wavelet based methods are available to achieve good noise reduction. These methods reduced the coefficients carrying noise to low values [161, 162]. An application of wavelet based de-noising methods on SPECT images was proposed by Noubari et al. [163]. They used PSNR criteria to arrive at an optimum threshold value. Simulated SPECT images were utilized to validate the performance of the algorithm. This method had a shortcoming in that the noise statistics present in the image was not considered. In the case of SPECT images the data is modeled as a Poisson process since the detection involves a counting process. Poisson noise depends on the image intensities, but Gaussian noise does not. Consequently direct application of wavelet based thresholding techniques become unsuitable in SPECT image denoising scenario.

The above problem was overcome by introducing a normalizing step which transforms the image statistics from Poisson to Gaussian [164]. Fisz transform was used as the variance normalizing stage in [165] and [166]. The method provided good results in low count setting. An adaptive Bayesian wavelet shrinkage method was performed on the

normalized data in [167]. Anscombe transform was used as the normalizing stage. The method proved well for scintigraphic images. Zhang et al. [168] also presented a variance stabilizing transformation method. Denoising techniques using total variation regularization was also in wide spread use for Poisson noised images [169].

Wiener filter was considered as a good linear filter for denoising images with Gaussian noise distribution [170] but the visual quality of the image was not satisfactory in all cases due to edge smoothing. The effect of Wiener filtering in SPECT images was examined by Links et al. [171]. The results suggest that the quantization of myocardial perfusion deficits was improved a little by the application of Wiener filter.

The noise in a SPECT image is Poisson noise. Consequently direct application of many existing denoising techniques will not give satisfactory results in SPECT images. In the proposed method denoising is done in a variance stabilized transform domain. An adaptive Wiener filter is utilized for denoising purpose. In the denoising stage, the edges may also get smoothed, which affects the quantification of tracer content region in cardiac SPECT images. Extend of smoothing depends on the size of the denoising filter. In the proposed method the size of the filter is carefully chosen according to the edge information present in the image to prevent edge smoothing, which consequently leads to better results.

5.3 Noise model in SPECT imaging

In SPECT imaging, a gamma camera detects the photons emitted by the process of radioactive decay. Due to the random nature of the detected photons, SPECT images suffer from a statistical noise. This can

be modelled by a Poisson distribution [158, 172]. Noise is a function of the number of detected counts, which in turn, depends on the image pixel intensity.

If O represents the SPECT image without noise, with $o(i,j)$ be the $(i,j)^{\text{th}}$ pixel and D represents the SPECT image degraded by noise, with $d(i,j)$ be the $(i,j)^{\text{th}}$ pixel then $d(i,j)$ is considered to be an independent Poisson random variable as noted in equation (1) with

$$E\{d(i, j) / o(i, j)\} = o(i, j) \geq 0 \quad (1)$$

The distribution is given in equation (2).

$$P(d(i, j) / o(i, j)) = \frac{o(i, j)^{d(i, j)} e^{-o(i, j)}}{d(i, j)!} \quad (2)$$

The noise is defined in equations (3), (4), and (5) as

$$n(i, j) = d(i, j) - E\{d(i, j) / o(i, j)\} \quad (3)$$

$$E\{n(i, j) / o(i, j)\} = 0 \quad (4)$$

$$\text{var}\{n(i, j) / o(i, j)\} = o(i, j) \quad (5)$$

The noise is pixel value dependent [169].

5.4 Proposed method

A method for reducing noise in SPECT image is introduced here. The image is converted into a domain with approximately stabilized variance using variance stabilizing transformation. This is done to reduce the pixel value dependency of the noise. Then a filter designed from the noisy image statistics is applied to reduce noise. The image is then

converted back to its original domain using inverse transformation. Figure 5.1 shows the basic blocks of the proposed method.

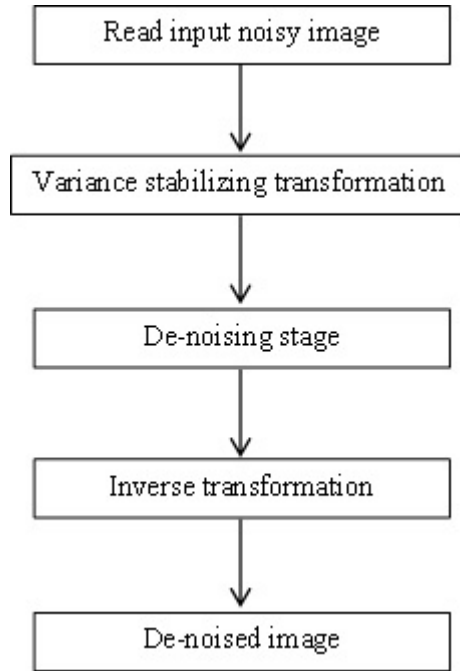


Figure 5.1 Steps in the proposed method

5.4.1 Variance stabilizing transformation

Variance stabilizing transformations help in removing the pixel value dependence nature of the noise variance [164, 165, 173]. Anscombe transform [164] is utilized in the proposed method for variance stabilization. Its expression is given in equation (6). Equation (6) converts an image with Poisson noise to an image with asymptotically additive noise. D denotes the image distorted using Poisson noise with $d(i,j)$ as the individual pixels and A denotes the Anscombe transformed image with $a(i,j)$ as the individual pixels.

$$a(i, j) = AT[d(i, j)] = 2\sqrt{d(i, j) + \frac{3}{8}} \quad (6)$$

5.4.2 De-noising stage

The pumping action of the heart is displayed in a cardiac SPECT image using different image slices. Each image slice shows the amount of tracer contained in a particular region of left ventricle at an instant of time. Each image slice will be different depending on the pixel count which represents the amount of tracer contained in the heart at that time. Based on the nature of the image slice, a de-noising stage is proposed in this section using Wiener filtering. The steps in the de-noising stage are shown in figure 5.2. Each image slice in the Anscombe domain is processed separately. A suitable operating window is fixed and a pixel wise Wiener filter is designed based on the local image statistics.

Stationary Wiener filtering is a popular method to reduce noise with known power spectra. The stationary Wiener filter is given in equation (7).

$$W = \frac{S_{oo}}{S_{oo} + S_{nn}} \quad (7)$$

S_{oo} and S_{nn} represent the power spectra of the original signal and the noise respectively. Instead of a stationary Wiener filter, a pixel wise Wiener filter is used here at the de-noising stage. The transfer function of the filter varies according to the statistics of the local neighbourhood in which filtering is applied. The size of the local neighbourhood is chosen based on the nature of the image slice.

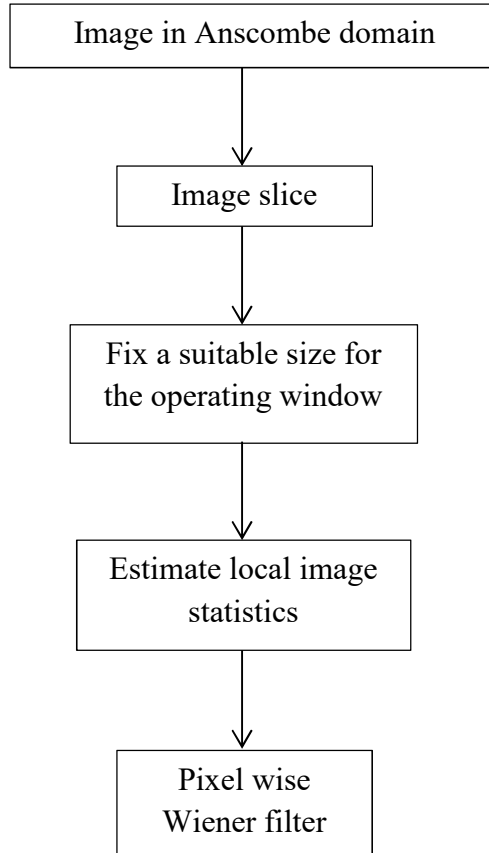


Figure 5.2 Basic steps in the de-noising stage

The nature of the image slice is analyzed in two contexts: based on the edge information and based on the tracer area information as shown in figure 5.3.

- Edge information: Pixel intensity variation is observed for the heart image slices. The greater the variation, lesser is the smoothing applied by selecting a smaller sized neighbourhood for the application of Wiener filter. This helps in preserving edges.

- Tracer area information: Each image slice is analyzed using binary thresholding to get an idea about the number of pixels representing the presence of tracer. A binary image is formed such that white pixels represent tracer content area of the image and black pixels represent myocardial region without tracer content and the background. Then an estimate of the number of pixels representing blood flow is made by counting the white pixels. The higher the pixel count, the lesser the noise [172]. For image slices with lower tracer area a bigger sized neighbourhood is chosen for better de-noising. This helps in improving the overall image signal to noise ratio.

Based on the edge information and tracer area information of each image slice, the size N by M of the local neighborhood β , is selected as shown in figure 5.3. For smaller size, N and M are chosen as 3 and for bigger size, N and M are chosen as 5.

The local statistics (mean, μ and variance, σ^2) of the selected neighbourhood is estimated using equation (8) and equation (9).

$$\mu = \frac{1}{NM} \sum_{(i,j) \in \beta} a(i,j) \quad (8)$$

$$\sigma^2 = \frac{1}{NM} \sum_{(i,j) \in \beta} (a(i,j) - \mu)^2 \quad (9)$$

Using the estimated local statistics, a pixel wise filter, $W(i, j)$, is designed as in equation (10). The average of all locally estimated variances is ν^2 .

$$W(i, j) = \mu + \frac{\sigma^2 - v^2}{\sigma^2} (a(i, j) - \mu) \quad (10)$$

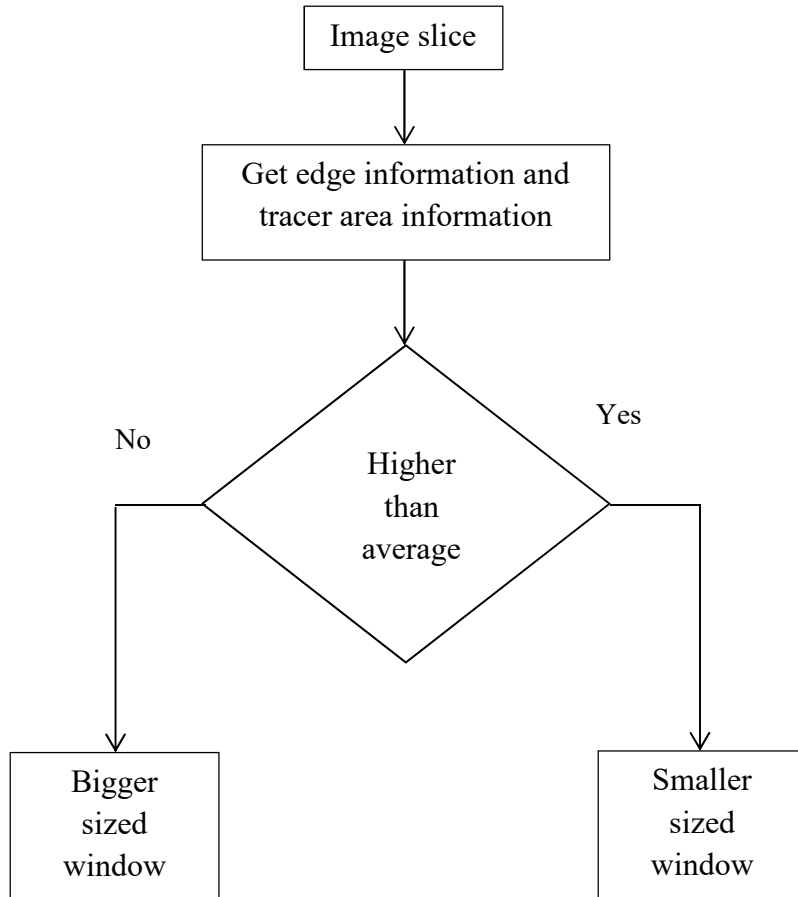


Fig. 5.3 Flowchart showing the steps for choosing the size of neighborhood

The image, A , in the Anscombe domain with pixels $a(i,j)$ is then filtered in the selected neighborhood N by M using the corresponding filter $W(i,j)$. The denoised image in the Anscombe domain is denoted by

F with $f(i,j)$ as the individual pixels which is considered as an estimate of $E\{A/O\}$.

5.4.3 Inverse transformation

The denoised image F in the Anscombe domain is converted back to the original domain using inverse transformation. Equation (11) gives the inverse of equation (6).

$$\text{Inverse } [F] = \left(\frac{F}{2}\right)^2 - \frac{3}{8} \quad (11)$$

The resulting estimate of the original image O is biased due to the nonlinearity of the transformation [164] as described by equations (12) and (13).

$$E\{A/O\} \neq \text{Transform } [E\{D/O\}] \quad (12)$$

$$\text{Inverse}[E\{A/O\}] \neq E\{D/O\} \quad (13)$$

An adjusted inverse given in equation (14) is used to provide an unbiased asymptotic value.

$$\text{Inverse } [F] = \left(\frac{F}{2}\right)^2 - \frac{1}{8} \quad (14)$$

5.5 Simulation results

The result of applying the proposed method on noisy cardiac SPECT image is presented in this section. Poisson noise was added to the image to obtain its noisy version. The denoising algorithm is directly applied on the noisy image, without using any deblurring technique or contrast enhancement. The performance of the proposed method was

evaluated qualitatively by visual analysis. PSNR, SSIM, IEF and image quality index (IQI) were the performance measures used for quantitative analysis. Image quality index is defined by modeling distortion as a combination of loss of correlation, luminance distortion, and contrast distortion [174]. The value of IQI ranges from -1 to 1. The maximum value 1 shows the case with the restored image equal to the original image.

Figure 5.4 shows the original image slice of an abnormal case with low amount of tracer content, noisy image slice and image slice denoised using proposed method.



Figure 5.4 SPECT image slice of an abnormal case with low tracer content

Figure 5.5 shows four slices of the image degraded by Poisson noise and the denoised image using proposed method. The image slices belong to an abnormal cardiac subject case taken from Medical Trust hospital database. Figure 5.6 shows noisy image of a normal cardiac case from Medical Trust hospital database and the denoised image using proposed method. The ability of the proposed method in reducing noise is also verified using MPI Spectrum dynamics case study images. The noisy

image and the image denoised using proposed method is given in figure 5.7.

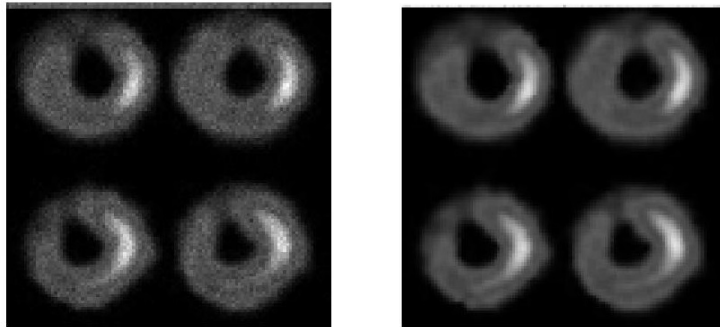


Figure 5.5 Noisy image and image de-noised using proposed method

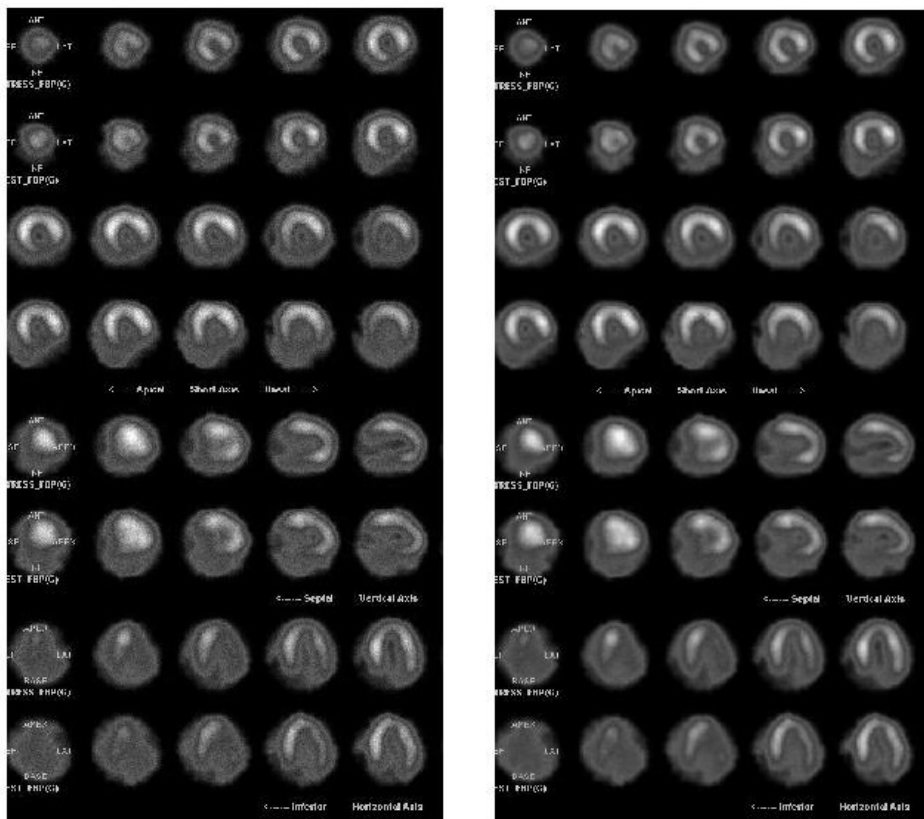


Figure 5.6 Noisy image and denoised image for a normal cardiac case

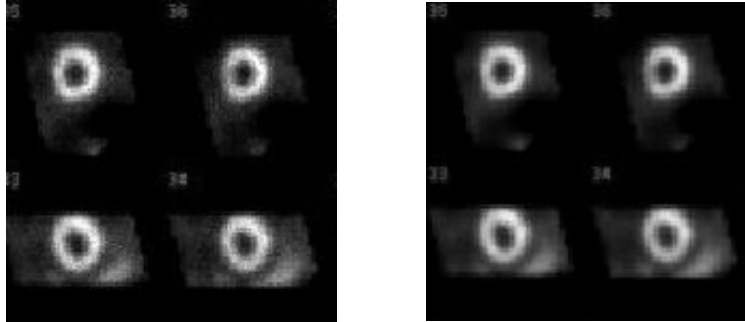


Figure 5.7 MPI Spectrum Dynamics case study image with Poisson noise and the denoised image using proposed method

The performance of the proposed method was also evaluated using simulated SPECT images using SIMIND software [163]. The reconstructed image of size 130 by 125 was used. Figure 5.8 shows the simulated image, noisy image and de-noised image and their respective image profiles. The image profile gives the set of intensity values along a straight line in the image. The obtained image profiles show that the proposed method could reduce the noise present in the noisy image.

The proposed de-noising method was evaluated quantitatively using the performance measures. The performance of the proposed method was also compared with the following state-of-the-art techniques:

- Block matching and three dimensional filtering (BM3D) based on sparse representation in transform domain proposed by Dabov et al. [175]

- Total variation de-noising proposed by Goldstein et al. [176]
- Wavelet thresholding [163].

The comparison results are given in table 5.1. The proposed method yielded the highest value of PSNR, SSIM, IEF and IQI showing that the quality of the image is improved by reducing noise and preserving the structural and edge information.

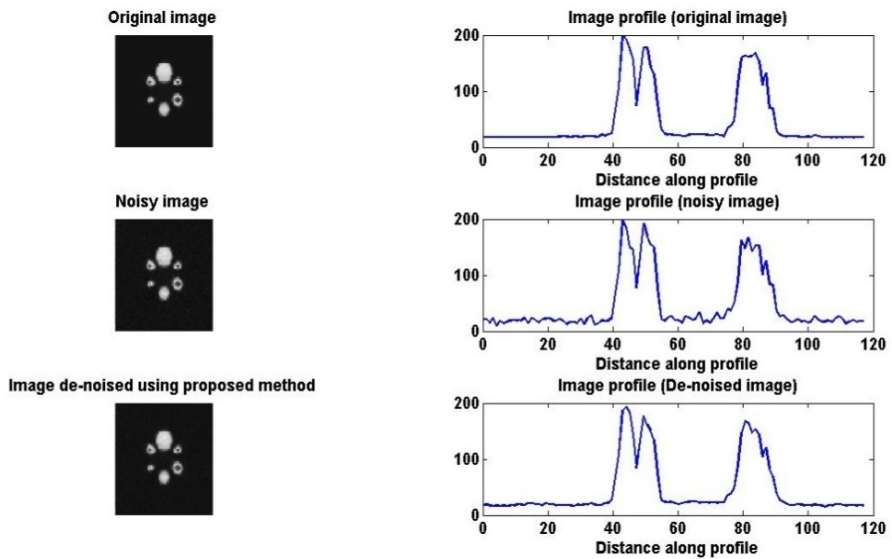


Figure 5.8 Simulated image, noisy image and de-noised image with their image profiles

Table 5.1 PSNR, SSIM, IEF and IQI values for various de-noising techniques applied on cardiac SPECT images

Performance measures	BM3D	TV de-noising	Wavelet thresholding	Proposed method
PSNR	31.2719	26.7727	33.2325	39.2309
SSIM	0.2800	0.3553	0.8471	0.9605
IEF	1.0078	0.8553	1.5828	6.1859
IQI	0.2840	0.4169	0.9109	0.9234

The performance of the proposed method was also compared with a denoising method using a fixed window Wiener filter in Anscombe domain. Figure 5.9, Figure 5.10, Figure 5.11 and Figure 5.12 show the comparison results in terms of PSNR, SSIM, IEF and IQI for 4 different patient cases. The plots show that the proposed method gave better images in terms of PSNR, SSIM, IEF and IQI.

Figure 5.13 shows the edge maps of original image, noisy image and denoised images using different denoising techniques. It can be seen that the edge map of the proposed method is closer to the edge map of the original image compared to other de-noising techniques. This shows that edge information and other finer details were preserved by the proposed method.

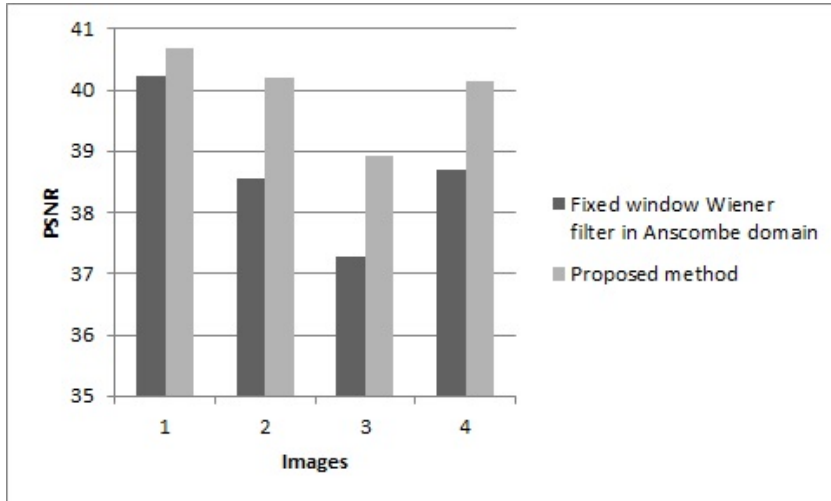


Figure 5.9 Comparison between the proposed method and denoising method using fixed window Wiener filter in Anscombe domain in terms of PSNR

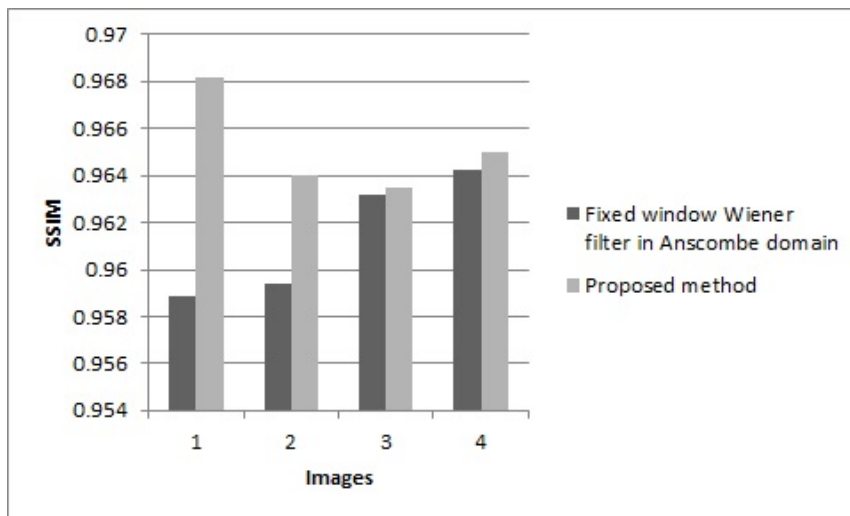


Figure 5.10 Comparison between the proposed method and denoising method using fixed window Wiener filter in Anscombe domain in terms of SSIM

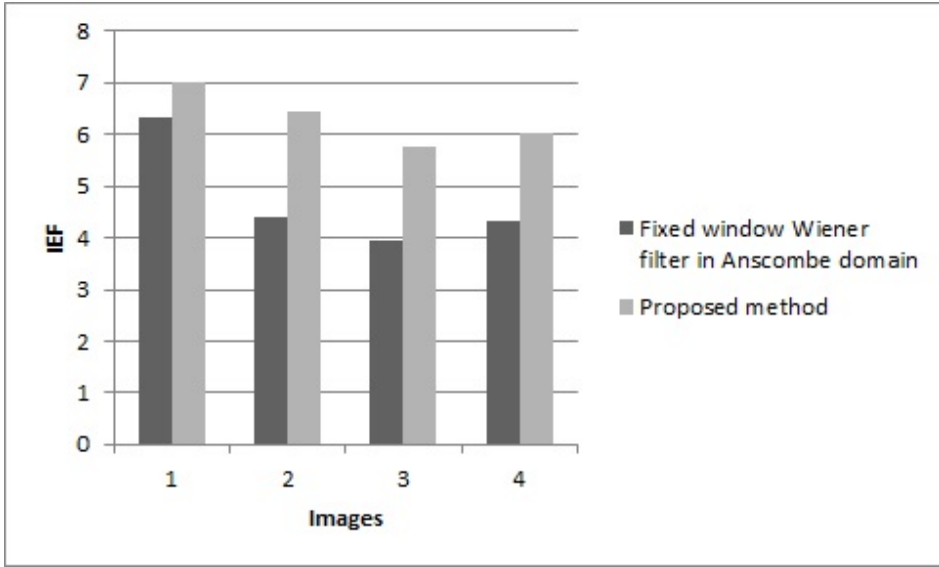


Figure 5.11 Comparison between the proposed method and denoising method using fixed window Wiener filter in Anscombe domain in terms of IEF

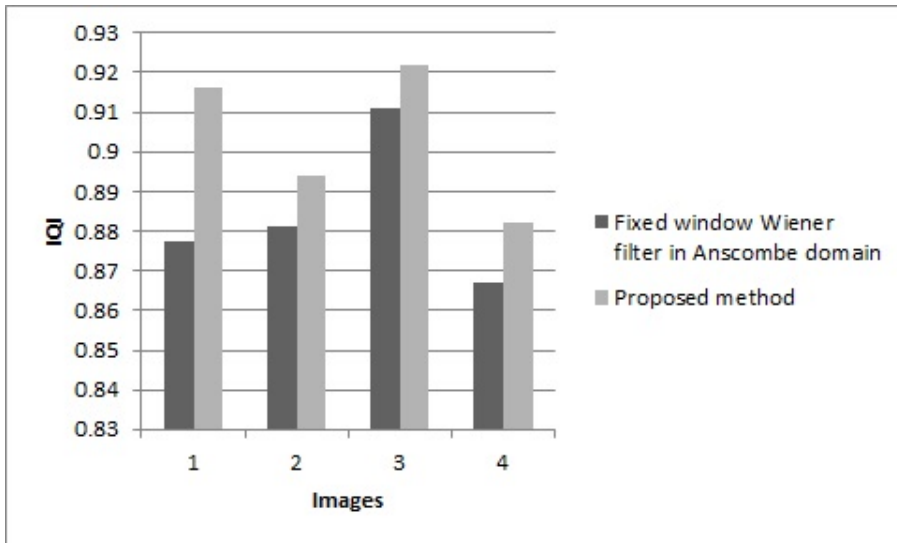


Figure 5.12 Comparison between the proposed method and denoising method using fixed window Wiener filter in Anscombe domain in terms of IQI

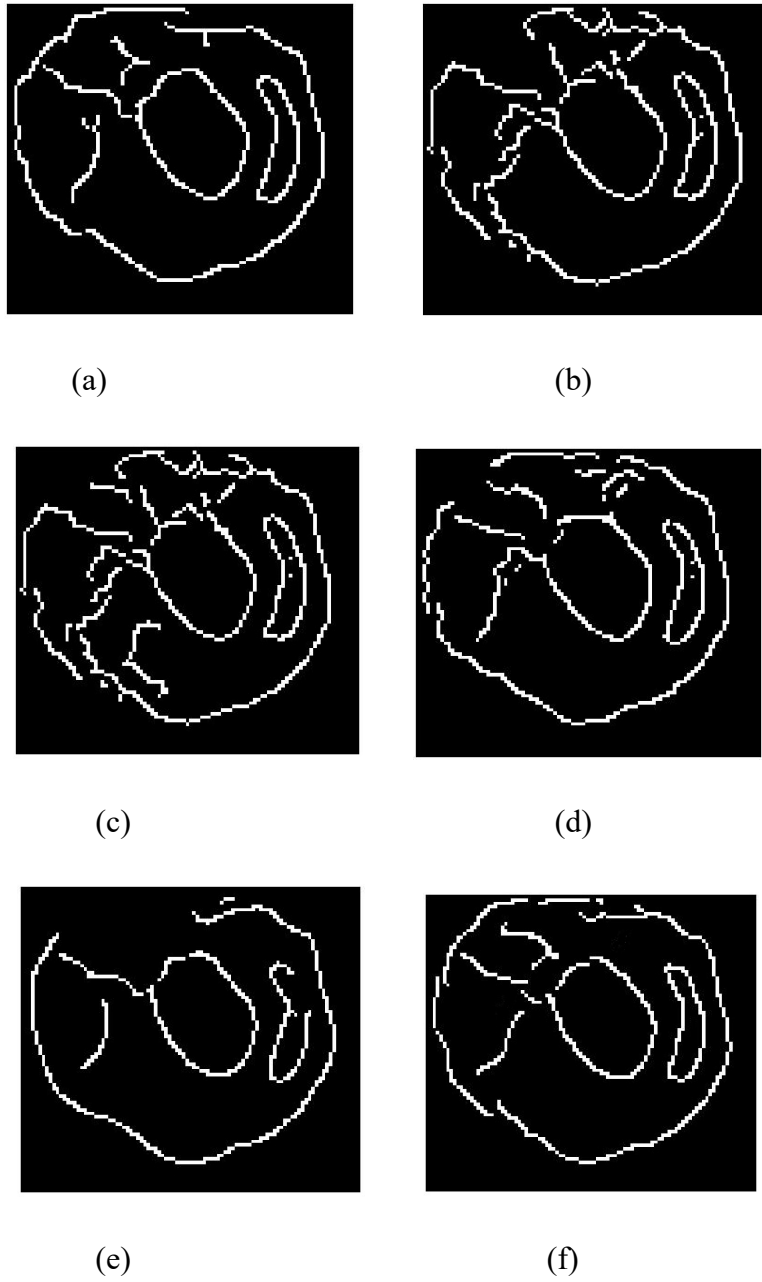


Figure 5.13 (a) Edge map of the original image, (b) edge map of the noisy image, (c)-(f) edge map of the de-noised images using BM3D, wavelet thresholding, fixed Wiener filter and proposed method respectively

5.6 Summary

This chapter described a denoising method suitable for SPECT images corrupted with Poisson noise. The proposed method demonstrated better denoising abilities for SPECT images compared to other techniques. The delivered results gave better de-noised images compared to other noise reduction techniques as proved by the visual analysis, PSNR, SSIM, IEF and IQI values. Satisfactory preservation of edge details was achieved as well, as shown by the edge maps extracted from the images.

Chapter 6

PIXEL INTENSITY BASED FEATURES FOR SPECT IMAGE CLASSIFICATION

An image feature based classification technique suitable for cardiac SPECT image has been developed for identifying normal and abnormal heart perfusion. Pixel intensities that correspond to tracer content in the left ventricular region are analyzed and novel features are extracted. Further on, a feedforward back propagation neural network algorithm is employed for classifying cardiac SPECT images into those of normal and abnormal hearts using the proposed features. Simulation studies were conducted on real cardiac SPECT images obtained from hospital. The result of classification has been verified by expert nuclear medicine physicians.

6.1 Introduction

SPECT perfusion images are very often used to visually analyze the distribution of blood flow to the heart muscles [105]. Cardiac perfusion images along with the functional parameters are usually used to study the functionality of heart. Left ventricular ejection fraction (LVEF), end diastolic volume and end systolic volume are important functional parameters that capture the effectiveness of human heart as an organ performing a pumping action [177]. These functional parameters are obtained using expensive quantification software [178]. A physician usually uses cardiac perfusion images along with the functional parameters for the diagnosis of cardiac ailments [179]. Perfusion abnormality is diagnosed visually by the appearance of relatively decreased uptake on different regions of perfusion images [180]. If the heart slices show regular blood supply throughout the heart muscles then a healthy heart condition can be surmised with high certainty [181]. Detection of disorders at the right time helps in controlling its advancement. A due recognition to this diagnostic requirement is clearly visible in the recent efforts and research in the development of software supporting medical image analysis and interpretation [182]. The nuclear imaging domain of medical diagnostics in the treatment of cardiac disorders is no exception [183]. Computer assisted diagnosis of cardiac perfusion studies is of great interest for the researchers in the image processing discipline.

6.2 Literature survey

Cios et al. [184] classified SPECT images of a human heart into normal or one of several abnormal categories. The reconstructed SPECT images were processed using boundary extraction, region of interest selection and segmentation techniques. They employed C4.5 [185] and CLIP3 [186] machine learning algorithms for classification. The authors obtained an accuracy of 94% for the system using the rules generated by C4.5 machine learning algorithm and 81% for the system using the rules generated by CLIP3 algorithm. The accuracy of CLIP3 algorithm was inferior, as compared to the accuracy of C4.5 algorithm. The results of CLIP3 algorithm got improved by incorporating fuzzy logic implementation.

Lindahl et al. [187] developed a computer based method for automatic detection of coronary artery disease in myocardial bull's eye scintigrams. A multilayer perceptron neural network architecture [188] is used as classification tool. Specificity and sensitivity results show that the networks performed similar to or better than those of human experts.

Kurgan et al. [189] processed cardiac SPECT images and extracted features useful to generate diagnostic rules. The authors used heuristic and inductive machine learning approaches. Their system provided a set of computer assisted diagnostic rules for heart SPECT cases.

A method was proposed by Cunha [190] to classify cardiac SPECT images using features extracted using multi objective evolutionary algorithms. The method was able to give solutions with some features, providing relevant information to the decision maker.

Szewczyk and Baszun [191] presented the possibility of using least squares support vector machine to the initial diagnosis of patients. K-fold Cross Validation, Grid-Search and Particle Swarm Optimization were utilized to find optimal parameters. Artificially made data and data taken from real database were used for testing the performance of the system. With particle swarm optimization they obtained a maximum classification accuracy of 93.58%.

Rafaie et al. [192] classified SPECT dataset containing the records of 267 patients using a combined rough set and neural network approach. Their method yielded an accuracy of 93% with a specificity and sensitivity of 85% and 95% respectively.

Arsanjani et al. [193] aimed to improve the diagnostic accuracy of SPECT image analysis by integrating quantitative perfusion and functional variables. They used invasive coronary angiography as the gold standard. Using support vector machine they obtained an accuracy of 86%.

Alves et al. [194] proposed a technique where image segmentation and registration are integrated to automatically extract features from cardiac SPECT images. These features are then used to classify the images into those with perfusion disorders and without perfusion disorders. The method yielded an accuracy of 87.6%.

6.3 Feature extraction

MPI using SPECT is a powerful diagnostic tool for the detection of coronary artery disease [195]. Quantitative evaluation of blood flow provides an evaluation of myocardial defects [196]. Nuclear medicine

physicians diagnose cardiac abnormalities by visually analysing the perfusion images and searching for regions with relatively decreased tracer uptake. In this thesis, pixel intensity based features which are capable of identifying lower tracer area are developed for classifying perfusion images with greater accuracy.

6.3.1 Image histogram based features

Image pixel intensity distribution is used as the basis for extracting histogram based features. End systolic and end diastolic heart slices obtained from the reconstruction software are used for extracting features.

6.3.1.1 Analysis of different intensity regions

An image slice contains three different regions as shown in figure 6.1. The three different regions are represented by A, B and C. The brighter pixels are in region A. It shows the presence of radiotracer which in turn represents the presence of blood. The medium intensity pixels are contained in region B. It shows the heart muscles with less amount of radiotracer which in turn represents myocardium with an interrupted blood flow. The darker pixels which represent the background fill up region C. The distribution of intensities among pixels in different regions is analysed using image histograms [197]. Figure 6.2 shows the image histograms for the regions A, B and C.

If the image intensities are scaled in the interval $(0, 1)$, it is observed that the pixels showing myocardium with blood flow have intensities in the range $(0.5, 1)$. All other pixels, including those showing myocardium with impaired blood flow and those representing

background, have intensities in the interval (0, 0.5). This analysis reveals the possibility of segmenting the myocardium region with blood flow.

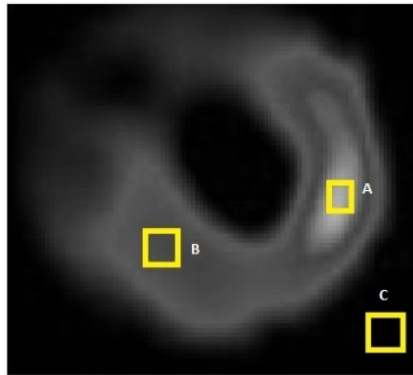


Figure 6.1 A heart slice with A, B and C showing three different regions in the image

A heart slice with regions A, B and C

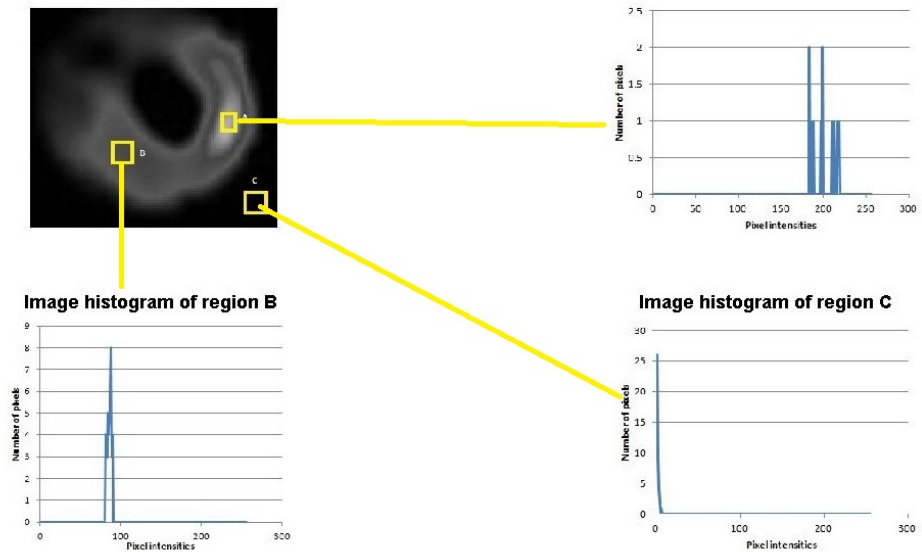


Figure 6.2 Image histogram of regions A, B and C. In each histogram x-axis represents the pixel intensities and y-axis represents the number of pixels with the corresponding pixel intensity

6.3.1.2 Segmentation of brighter pixel region

The brighter pixel region (region A) is segmented using region growing method [197, 198]. Based on the analysis made in section 6.3.1.1 a threshold level is set to identify brighter pixels. The image slice is converted into a binary image using binary thresholding with the set level. All pixels with intensities greater than the set level is given a value 1 (white pixels) and all pixels with intensities smaller than the set level is given a value 0 (dark pixels) in the binary image. The brighter pixel region is segmented from the image slice using region growing. The binary image obtained by the process of thresholding acts as seed point array for region growing process. Slices from short axis view, vertical long axis view and horizontal long axis view of a heart with normal perfusion and their corresponding segmented images are given in figure 6.3, figure 6.4 and figure 6.5 respectively. Figure 6.6 shows a short axis heart slice with abnormal perfusion and the segmented slices.

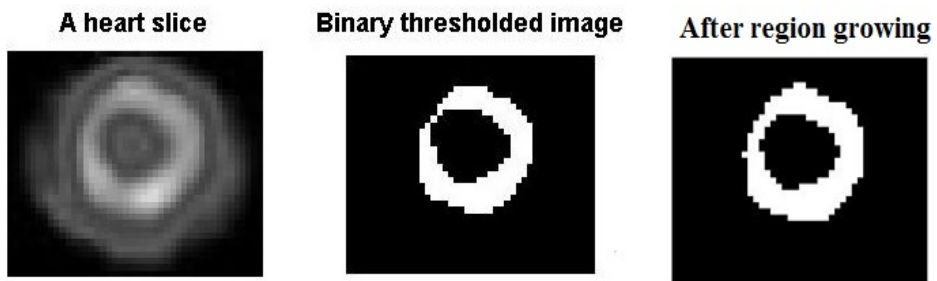


Figure 6.3 A slice from the short axis view of a heart with normal perfusion and its segmented images

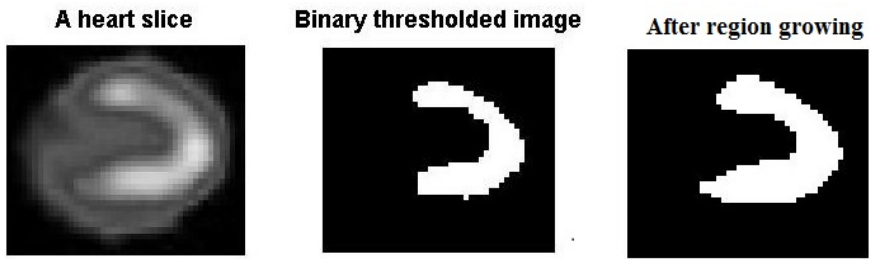


Figure 6.4 A slice from the vertical long axis view of a heart with normal perfusion and its segmented images

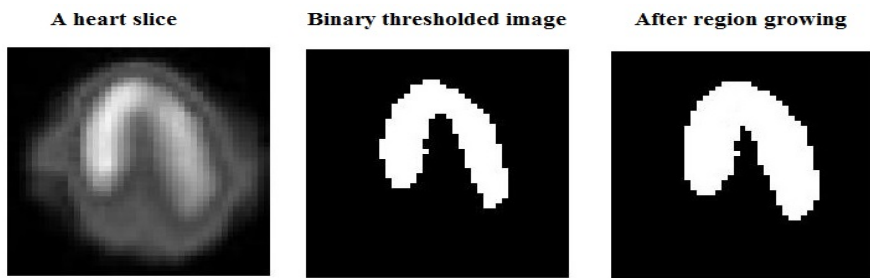


Figure 6.5 A slice from the horizontal long axis view of a heart with normal perfusion and its segmented images

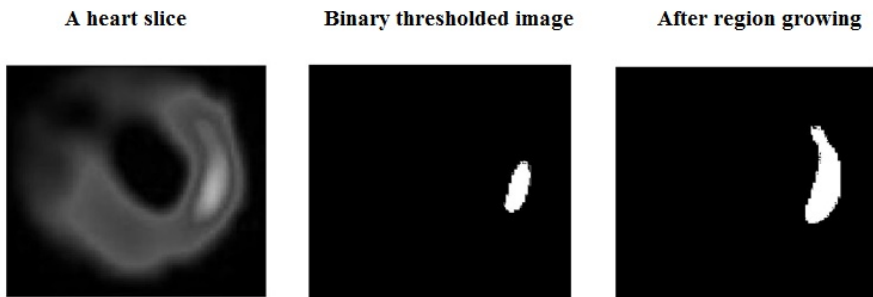


Figure 6.6 A slice from the short axis view of a heart with abnormal perfusion and its segmented images

6.3.1.3 Extraction of features

The segmented image represents the brighter pixels showing the myocardium with blood flow. Then an estimate of the number of pixels in the segmented region is made. The image histogram based features include the estimated number of pixels from the segmented systolic and diastolic short axis, vertical long axis and horizontal long axis slices.

6.3.2 Gray level co-occurrence matrix based features

The spatial relationship of the pixels in an image is depicted by its gray level co-occurrence matrix (GLCM) [199]. The matrix considers the textural features within the image. Since GLCM characterizes texture of an image there is no need to process the whole image. Instead the image is scaled down to a lower scale to simplify further processing. The number of intensity values in the systolic and diastolic image slices can be scaled down to a lower value. In the proposed method a value of 8 is chosen as a safe value without information loss. If the image contains 8 intensity levels then the size of its GLCM will be 8 by 8. The $(i, j)^{\text{th}}$ element in the GLCM matrix indicates the number of times the pixel with value i comes in a given spatial relationship to the pixel with value j . Horizontally adjacent pixel is used for analysis.

The statistical properties of the image like contrast, correlation, energy and homogeneity are derived from the GLCM. Contrast gives a measure of intensity contrast between a pixel and its neighbour as defined by the spatial relationship. Correlation shows how well a pixel is correlated to its neighbour. The sum of squared elements in the GLCM is a measure of its energy and homogeneity defines how close an element is to the GLCM diagonal.

The GLCM based features for the proposed method include the statistical properties like contrast, correlation, energy and homogeneity of the short axis perfusion image slices. The ratio between GLCM derived contrast from systolic and diastolic slices is also used as a feature.

6.3.3 Intensity variation based feature

A cardiac SPECT image slice contains different intensity regions as shown in figure 6.1. The intensity variation can be categorised as smooth in the normal perfusion region of a heart slice. The smooth variations constitute the low frequency component of the image. Smooth variations can be separated from the details of the image in many ways. One popular way is decomposition using discrete wavelet transform [200]. 10 slices from apex to base are selected from the short axis view of quantitative perfusion SPECT image. The approximation coefficients up to a single level are separated out using discrete wavelet transform. Daubechies wavelets are used. The smooth variation thus estimated from the short axis slices constitutes intensity variation based feature.

6.3.4 Fractal based feature

Fractal based feature is also visible in perfusion images. Normal and abnormal heart apex region show a difference in the tracer content in the perfusion image. This difference in physical profile is identified using fractal dimension.

6.3.4.1 Fundamentals of fractals and fractal dimension

Euclidean geometry is used in conventional mathematics to describe different shapes and patterns. But describing nature by traditional Euclidean geometry is not easy, as nature in its microcosm and many

naturally observed physical objects even at macro levels cannot be represented by idealized shapes. This difficulty led to identifying a family of shapes called fractals. Mandelbrot [201, 202] defined fractals as a fragmented geometric shape that can be subdivided in parts, each of which is a reduced copy of the whole.

Fractal dimension gives an indication of how a fractal fills a space completely, if zoomed down to finer scales [203]. Box counting method is the simplest method to compute fractal dimension. If the bounded set A contains N_r distinct copies of itself, each of which has been scaled down by the ratio r , then fractal dimension D is as follows

$$D = \lim_{r \rightarrow 0} \frac{\log(N_r)}{\log(1/r)} \quad (1)$$

6.3.4.2 Extraction of fractal based features

Short axis view slice from the heart's apex region is considered for extracting fractal based features. The blood flow region is segmented using binary thresholding. Figure 6.7 shows the short axis view slice at the apex region of a heart with normal perfusion and its binary thresholded image. Figure 6.8 depicts an abnormal perfusion heart image. The smallest shape that builds up the blood flow region is shown in figure 6.9 and 6.10.

Comparing figure 6.9 and figure 6.10 it can be concluded that normal perfusion and abnormal perfusion apex regions can be picked out by taking scaling property of the smallest unit that builds up the tracer content region. Fractal dimension measures the scaling properties of fractals and thus the complexity of the structure. It is a number that

characterizes the structure. Normal perfusion apex slices have more tracer content region, leading to a more complex structure, than abnormal perfusion slices. So naturally their fractal dimension value is more. Box counting method is employed since it is simple and suitable for finding the fractal dimension of binary images.

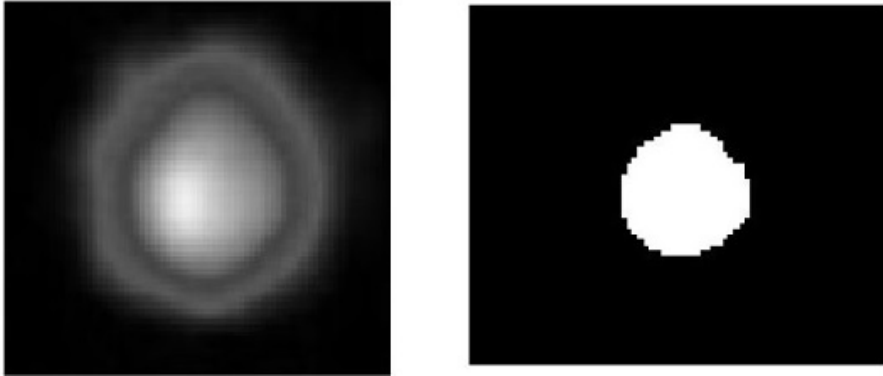


Figure 6.7 A slice from the apex region of a normal perfusion heart and its binary thresholded image

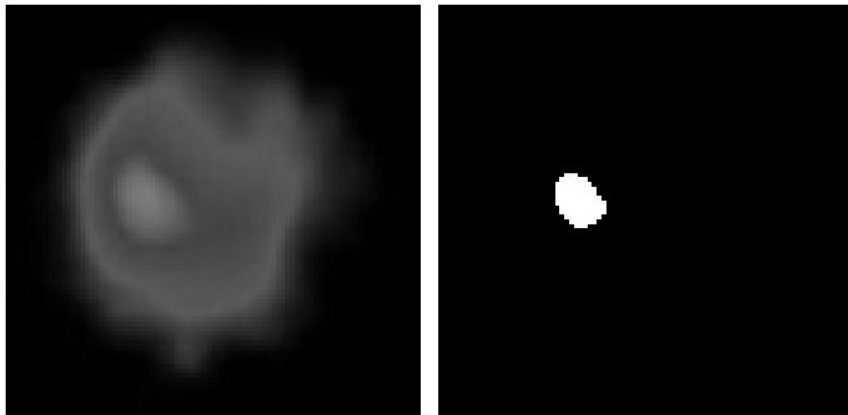


Figure 6.8 A slice from the apex region of an abnormal perfusion heart and its binary thresholded image

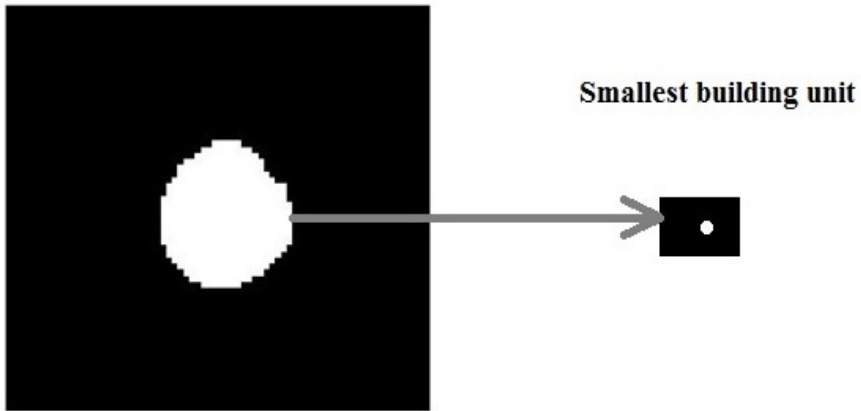


Figure 6.9 Binary thresholded image for the normal perfusion case and the smallest shape that builds up the entire blood flow region



Figure 6.10 Binary thresholded image for the abnormal perfusion case and the smallest shape that builds up the entire blood flow region

6.3.5 Standard deviation of brightness

A normal image slice has brighter tracer content region as compared to the background. In an abnormal image slice, region with lesser tracer content is represented by medium intensity pixels. The

brightness values will be almost close to the mean brightness value. So the standard deviation of brightness for an abnormal image slice will be less as compared to that of a normal image slice. Standard deviation of the brightness for short axis and long axis slices for the perfusion image is taken as a feature.

6.4 Features extracted from randomly selected images

A set of sample images are selected randomly from the database to analyse the extracted features graphically. The sample image set consists of 16 images. It includes 8 normal heart images and 8 abnormal heart images. Features defined in section 6.3 are extracted from images in the sample set. Image histogram based features proposed in section 6.3.1 are extracted from the sample set images and plotted in figure 6.11. Figure 6.12, figure 6.13, figure 6.14 and figure 6.15 depict directly derived GLCM features described in section 6.3.2. The extracted GLCM features are contrast, correlation, energy and homogeneity. For abnormal images the average values of these features are the lowest. But features for normal image class were not linearly separated from the features of abnormal image class as shown in the figures. Hence these features need a classifier which classifies data points that are not linearly separable. The ratio between GLCM derived contrast feature from systolic and diastolic slices is also mentioned as a feature in section 6.3.2. The extracted values for this ratio from the sample set images are shown in figure 6.16. The intensity variation based features explained in section 6.3.3 for 16 images are plotted in figure 6.17. Figure 6.18 shows the fractal based features explained in section 6.3.4. The standard deviation of brightness for the short axis and long axis slices is plotted in figure 6.19.

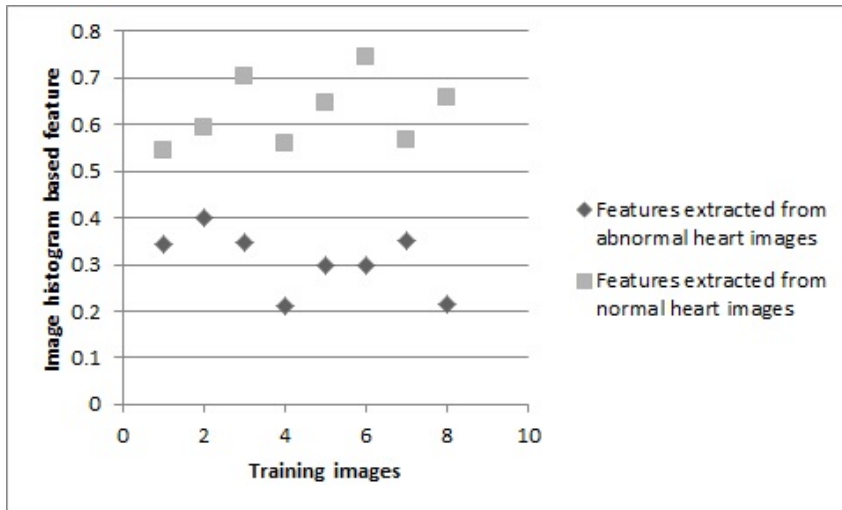


Figure 6.11 Image histogram based features

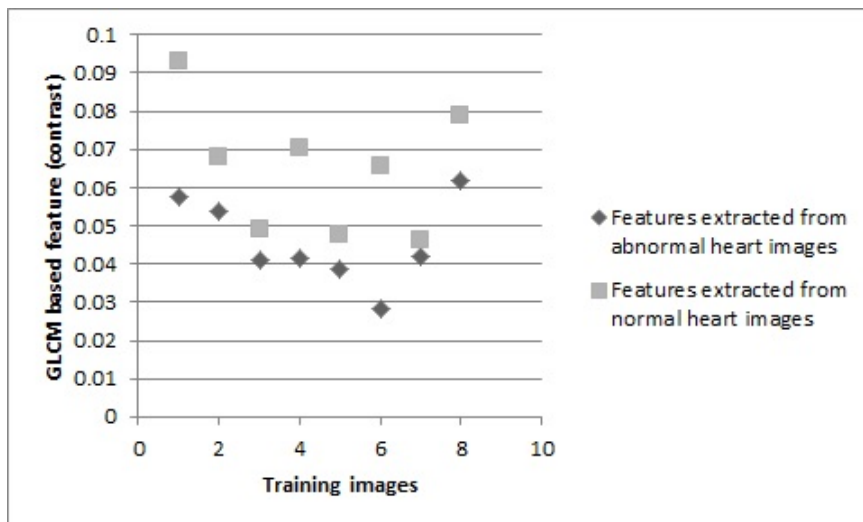


Figure 6.12 GLCM based feature (contrast)

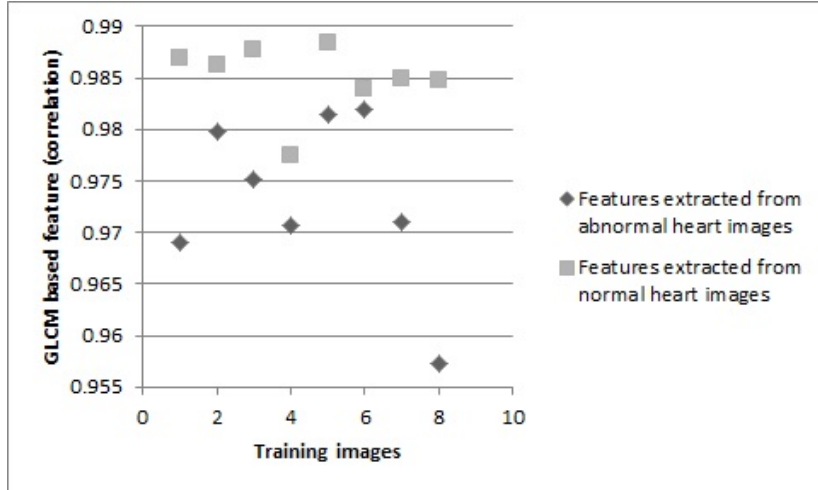


Figure 6.13 GLCM based feature (correlation)

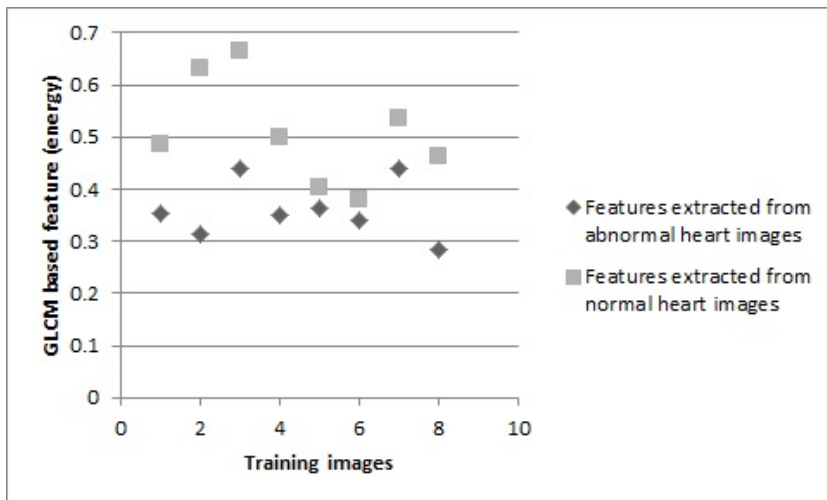


Figure 6.14 GLCM based feature (energy)

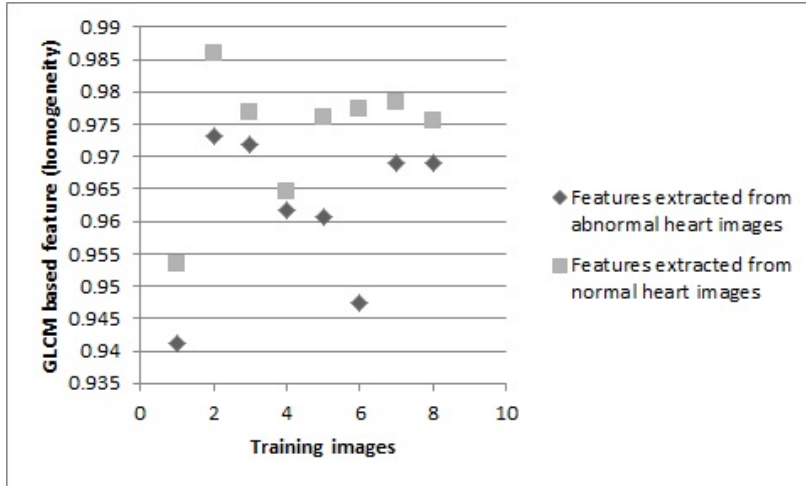


Figure 6.15 GLCM based feature (homogeneity)

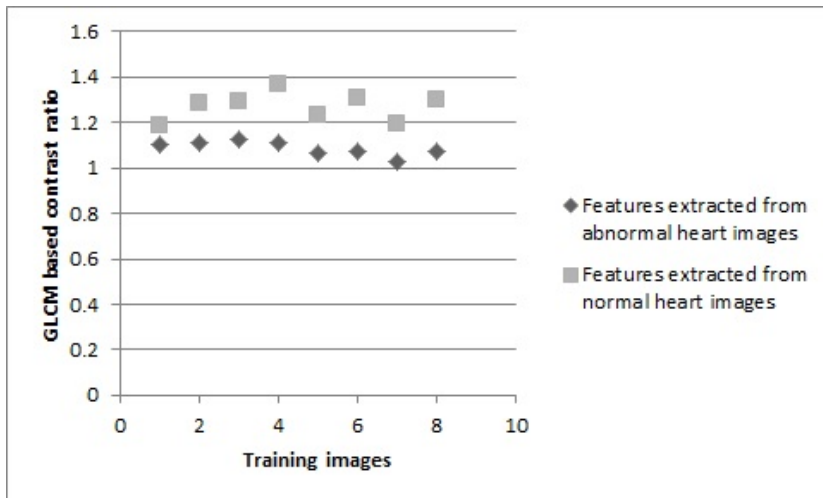


Figure 6.16 GLCM based feature (contrast ratio)

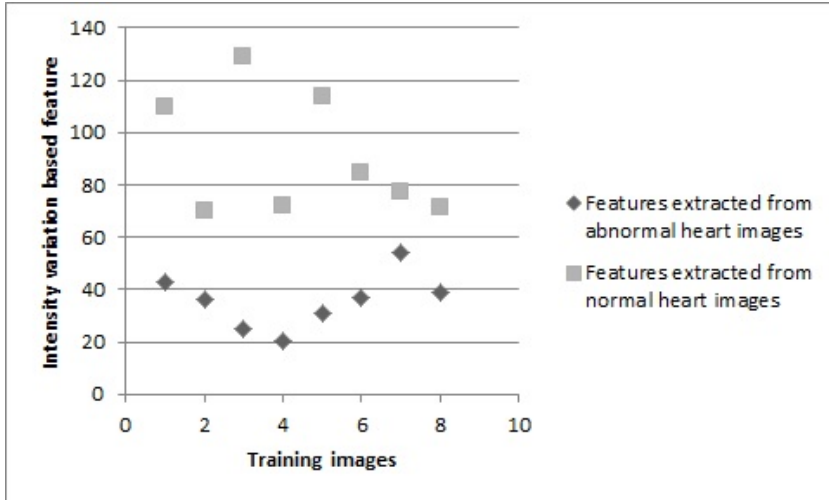


Figure 6.17 Intensity variation based feature

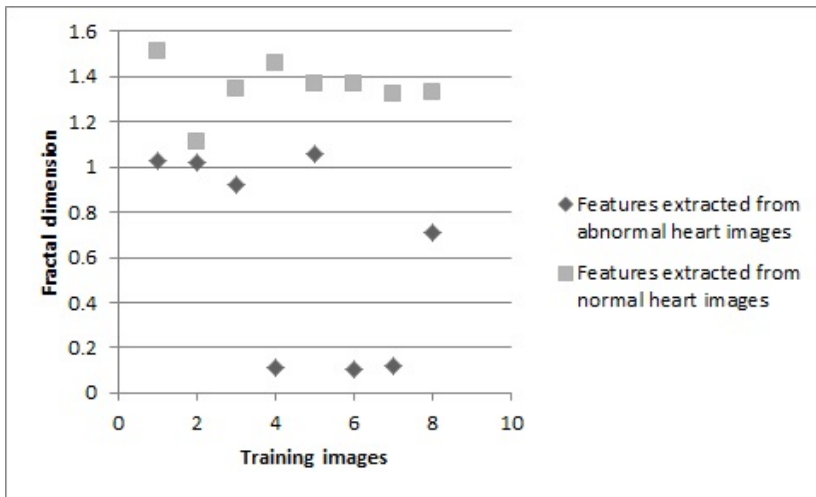


Figure 6.18 Fractal based features

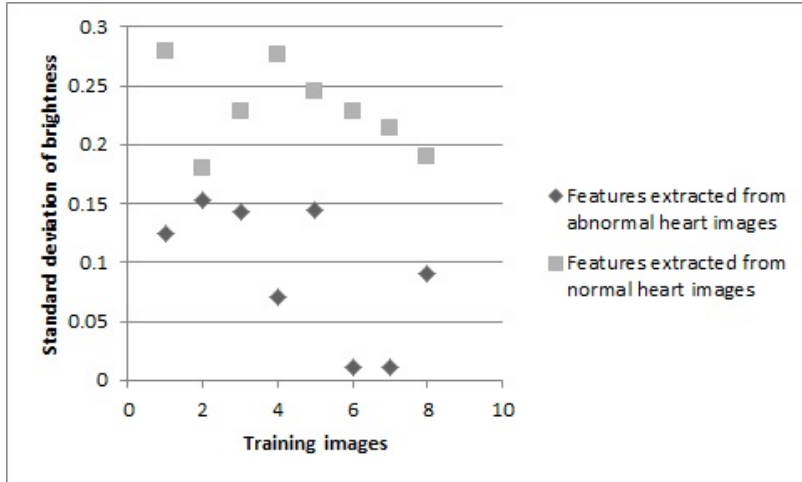


Figure 6.19 Standard deviation of brightness for heart slices

The features computed according to sections 6.3.1, 6.3.2, 6.3.3, 6.3.4 and 6.3.5 for the randomly selected images are shown in table 6.1. The ranges of feature values obtained for normal and abnormal heart images are given in the table with the mean of the feature values included. The mean of all the feature values are the lowest for abnormal images. In addition to that, the ranges of values of normal image group do not overlap with the ranges of values of abnormal image group. Hence these features can be used effectively for the classification of cardiac SPECT images into normal and abnormal heart images.

Table 6.1 Comparison of different features obtained for normal and abnormal heart images

Features		Abnormal image	Normal image
GLCM based contrast ratio	Range of values	1.0283 to 1.1274	1.1885 to 1.3655
	Mean value	1.0860	1.2696
Histogram based feature	Range of values	0.2115 to 0.4002	0.5451 to 0.7436
	Mean value	0.3081	0.6272
Intensity variation based feature	Range of values	20.0832 to 54.1392	70.1089 to 128.665
	Mean value	35.7322	91.0520
Standard deviation of brightness	Range of values	0.0111 to 0.1526	0.1802 to 0.2795
	Mean value	0.0936	0.2303
Fractal dimension	Range of values	0.1011 to 1.0564	1.1125 to 1.514
	Mean value	0.6324	1.3528

6.5 Classification algorithm used

A classification algorithm is used to separate out SPECT images into normal and abnormal perfusion heart images from the extracted features. A neural network classifier with feed forward back propagation algorithm [204] is applied. The weight values are updated using Levenberg-Marquardt method [205, 206].

6.5.1 Feed forward neural network

Artificial neural networks closely represent mathematical models of biological nervous system. The idea of neural networks emerged after describing the nets by means of propositional logic [207]. Feed forward network is an artificial neural network architecture commonly used in the field of medical image classification. Neurons are arranged in three different layers: input, hidden and output layers. The general structure of a feed forward neural network is shown in figure 6.20.

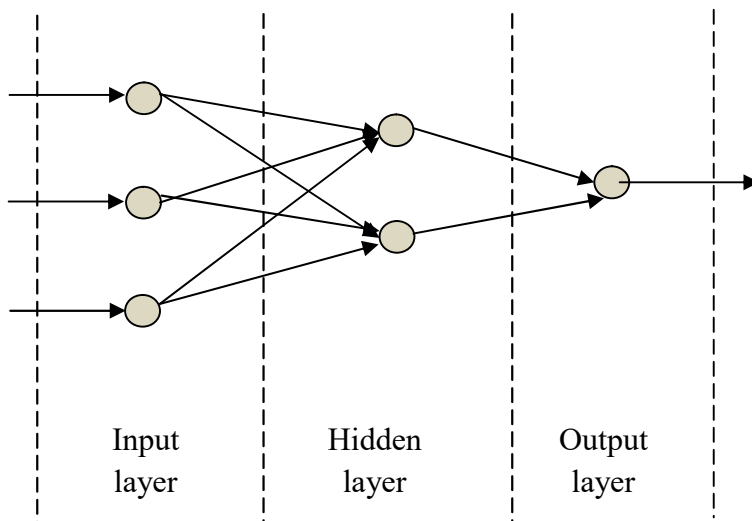


Figure 6.20 Architecture of a feed forward neural network

The classification technique consists of training and testing phases. The best weight and bias values are found out during the training phase using known input-output pairs. The unknown inputs are classified using the trained neural network at the testing phase. An iterative back propagation algorithm is used in the training phase. The training begins with random weights and the iterative algorithm adjusts the weights so that the error (difference between the actual output and the expected output) is minimal. Levenberg–Marquardt algorithm [205, 206] is used to optimize the weights. It blends the steepest descent method and Gauss-Newton algorithm [208].

6.6 Experimental setup

The experimental analyses were carried out on 100 images. The images were taken from 100 different patients under medical diagnosis in Medical Trust Hospital, Kochi, India. The database consists of reconstructed SPECT images obtained from a two collimator single photon emission computed tomography GE made device. The obtained results were verified with the gold standard provided by QGS developed by Cedars Sinai Medical Centre, Los Angeles and cross verified by the senior nuclear medicine physicians, Dr. Kuruvila Varkey of Bharat Scan Centre, Kottayam, India and Dr. Shamaly George of Medical Trust Hospital, Kochi, India.

- Specifications of Neural Network: The built-in function in Matlab was used for the experiments.
 - Number of input nodes: 9
 - Number of output nodes: 1
 - Number of hidden layers: 1

6.7 Performance measures

The ability of the algorithm to identify normal and abnormal cases was evaluated using sensitivity, specificity and accuracy. These are measured by detecting true positives (TP), true negatives (TN), false positives (FP) and false negatives (FN).

TP:

Correct classification in which abnormal perfusion case gets detected as abnormal.

TN:

Correct classification in which normal perfusion case gets detected as normal.

FP:

Incorrect classification in which normal perfusion case gets detected as abnormal.

FN:

Incorrect classification in which abnormal perfusion case gets detected as normal.

Sensitivity:

Sensitivity is the true positive fraction (TPF). It is the capability of the classification system to identify abnormal perfusion cases.

$$Sensitivity = \frac{TP}{TP + FN} \quad (2)$$

In other words, sensitivity is defined as the ratio of the number of identified abnormal perfusion cases to the total number of abnormal perfusion cases.

$$\text{False negative fraction (FNF)} = 1 - \text{sensitivity} \quad (3)$$

$$FNF = \frac{FN}{TP + FN} \quad (4)$$

Specificity:

Specificity is the true negative fraction (TNF). It is the capability of the classification system to identify normal perfusion cases.

$$Specificity = \frac{TN}{TN + FP} \quad (5)$$

Specificity is defined as the ratio of the number of identified normal perfusion cases to the total number of normal perfusion cases.

$$\text{False positive fraction (FPF)} = 1 - \text{specificity} \quad (6)$$

$$FPF = \frac{FP}{TN + FP} \quad (7)$$

Accuracy:

Accuracy is the ratio of the number of correct detection to the total number of cases.

$$Accuracy = \frac{TP + TN}{TP + TN + FP + FN} \quad (8)$$

Receiver operating characteristics (ROC) curve:

ROC curve is plotted using sensitivity and specificity values [209]. It is a graph plotted with sensitivity along y-axis and FPF (1 – specificity) along x-axis as shown in figure 6.21. ROC curve for an ideal case with 100% sensitivity and 100% specificity passes through the upper left corner [210]. AUC represents the area under the curve.

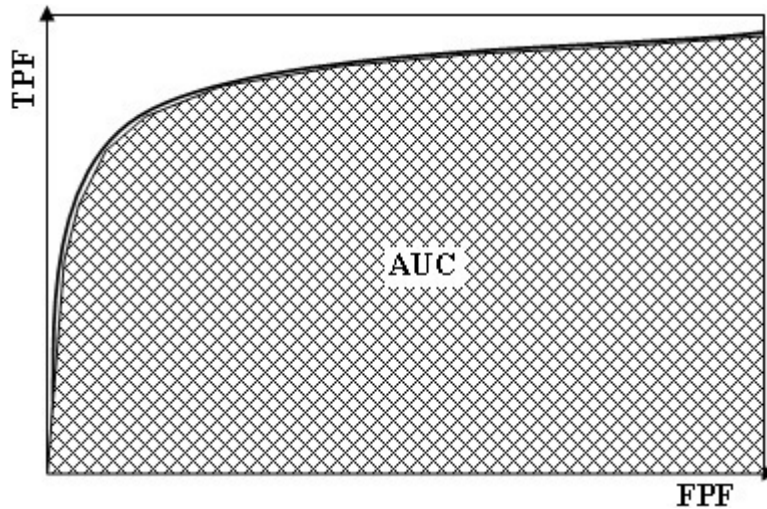


Figure 6.21 ROC curve

6.8 Results and discussions

Deciding on whether the heart is functioning normally from the SPECT images without using any quantification software is a challenging task for the physicians. The discussed method focuses on interpreting cardiac SPECT images as normal or abnormal without utilizing any quantification software.

Classification was performed on 100 images. The features extracted from 100 patients were divided randomly into training, validation and testing data sets. The algorithm was evaluated using specificity, sensitivity and accuracy.

The method yielded a sensitivity of 98.4%, specificity of 94.7% and accuracy of 97%.

The performance of the algorithm was compared with the direct interpretation of two practising nuclear medicine experts. The perfusion image slices and the end systolic and end diastolic slices were presented to the experts. Neither quantification results nor the results of classification based on the gold standard were available before the experts during the classification process. The experts classified each patient study into two categories: normal perfusion and abnormal perfusion. Classification was performed on 20 images. Then classification was performed on the same set of images using the proposed method. Table 6.2 shows a comparison of correct detections by the proposed method and visual interpretations of the expert physicians.

Figure 6.22 and Figure 6.23 respectively depict the confusion matrices obtained for one of the attending expert's visual analysis based classification and proposed classification method. Figure 6.24 compares the ROC curves obtained in both the cases. Usually, classifier with the higher area under the ROC curve is considered better. Proposed classifier ROC curve had an area of 0.9375 under it whereas visual reading based classifier had an area of 0.8333 under it, suggesting that the proposed method had a better ability to discriminate normal and abnormal heart images. In addition, the areas under the ROC curves were compared

statistically using Chi-square test. The test gave a chi-square value of 3.9543 with 1 degree of freedom with a p-value of 0.0468. This shows that there is a significant difference in the discriminating ability of the two classifiers. The higher area under the ROC curve for the proposed method suggests that it has a better ability to interpret normal and abnormal heart images. The results show that the proposed method aids the nuclear medicine physician to reach a more accurate decision on the cardiac health from the perfusion images alone.

Classification is also done on blurred and noisy images as well to examine the role of pre-processing stages discussed in chapter 4 and chapter 5. The experiment was conducted on a sample image set with 20 patient cases. Without using pre-processing stage, classification yields an accuracy of 85%. Whereas classification on the features extracted from the pre-processed image yields a classification accuracy of 95%. The accuracies are also compared statistically using Chi-square test. The test gives a Chi-square value of 4.500 with 1 degree of freedom with a p value of 0.0339 which show a significant difference between the obtained accuracies. The comparison of ROC for the classifier with and without pre-processing is depicted in figure 6.25.

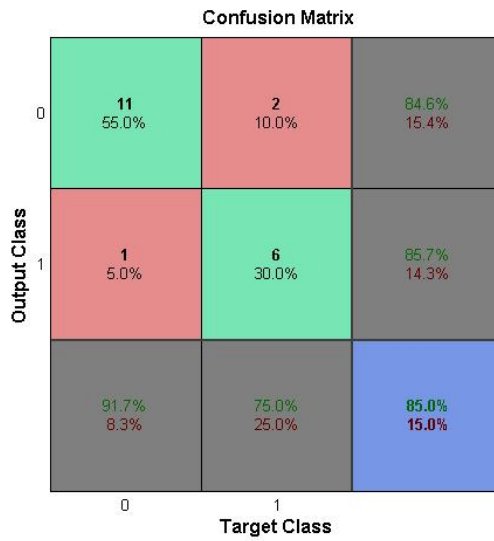


Figure 6.22 Confusion matrix obtained for one of the attending nuclear medicine experts' visual analysis based classification for 20 patient cases



Figure 6.23 Confusion matrix obtained for proposed classification method for 20 patient cases

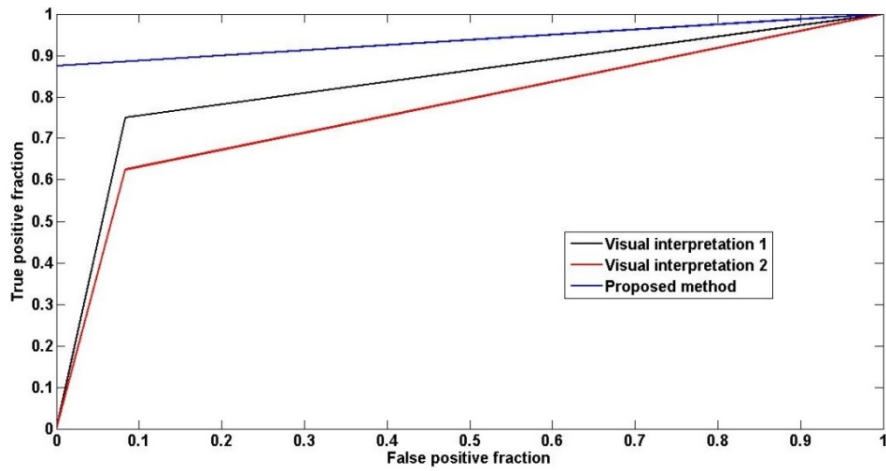


Figure 6.24 Comparison of the performance of proposed method against that of visual classification in terms of ROC curves

Table 6.2 Comparison of correct detections by the proposed classification method and visual interpretations by two attending nuclear medicine experts

	Visual interpretation 1	Visual interpretation 2	Proposed method
TP	11/12	11/12	12/12
FN	1/12	1/12	0/12
TN	6/8	5/8	7/8
FP	2/8	3/8	1/8
Correct detections	17/20	16/20	19/20

Table 6.3 compares the accuracy of the classifier with and without pre-processing stage for different number of patient cases. The accuracy of the classifier is improved with the features extracted from denoised and deblurred images. The results in table 6.3 show that the proposed pre-processing stages work well to improve the diagnostic accuracy for images by reducing noise and blur.

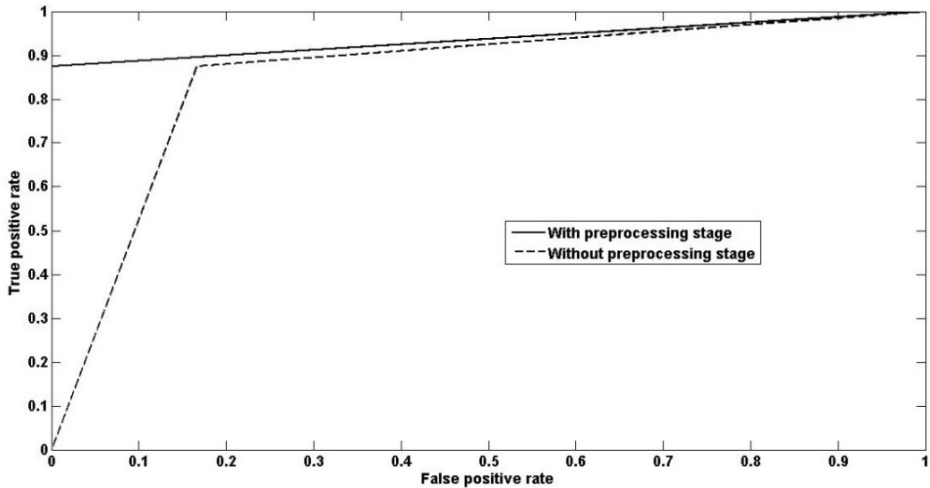


Figure 6.25 ROC comparison for classifiers with and without pre-processing stage

The performance of the method proposed in the thesis was compared with the method described in literature by Ciecholewski [211]. Tracer content region estimates for end systolic and end diastolic slices were used by its author as features. The author used support vector machine in the classifier stage. The performance comparison results are

given in table 6.4. The classification using the features proposed in the thesis yielded greater accuracy as compared to the method in literature.

Table 6.3 Comparison of classifier accuracies with and without pre-processing stage

Number of patient cases	Classifier accuracy with pre-processing stage	Classifier accuracy without pre-processing stage	Chi-square test
20	95%	85%	Statistically different (p=0.0339, Chi-square value=4.500)
50	96%	86%	Statistically different (p=0.0262, Chi-square value=4.9451)
100	97%	85%	Statistically different (p=0.0066, Chi-square value=7.3871)

Table 6.4 Comparison of the performance of proposed method with the method proposed in literature

	Features used	Classifier used	Obtained accuracy
Method proposed by Ciecholewski [211]	Tracer content region for end systolic and end diastolic slices	Support vector machine	92%
Proposed method	Proposed features	Neural network	97%

6.8 Summary

The proposed features assisted in improving the accuracy of cardiac perfusion image classification. A back propagation neural network with Levenberg-Marquardt optimization is employed for classification. The database consists of original cardiac SPECT images collected from Medical Trust Hospital, Kochi, India. The measures used to assess the performance of the proposed method are specificity, sensitivity and accuracy.

Chapter 7

CONCLUSION AND FUTURE PROSPECTS

A summary of the work discussed in earlier chapters for SPECT image enhancement and classification and the scope for future work in the subject discipline are outlined in this chapter.

7.1 Concluding remarks

The previous chapters have described the work that has been accomplished on the development of algorithms to enhance and classify cardiac SPECT images.

The developed algorithms for enhancement focused to improve contrast, reduce blur and reduce noise. Contrast enhancement, deblurring and denoising algorithms were developed independently. We can use a single algorithm or a combination of algorithms to enhance a SPECT image without any further modification. A method based on morphological processing, utilizing the advantage of adaptive window processing, was proposed for the purpose of improving the contrast features of cardiac SPECT images. Improving the contrast features helped to keep apart the dark and bright areas in the image. This improved the interpretability of tracer content information in the image. An analysis of the image quality was performed using visual analysis, CI, MSE, ED, SSIM and PSNR. A total variation regularization based method was discussed to reduce blur present in cardiac SPECT image. An estimate of the distortion operator is made for each image slice using ML approach and total variation regularization is performed using the estimated parameter. The KL test guaranteed minimal addition of noise during ML iterations. The method reduced blur while maintaining high PSNR. The performance was evaluated using visual analysis, PSNR, SSIM, BM and IEF. A Wiener filter denoising method in a variance stabilized domain was proposed in this thesis to reduce the noise present in cardiac SPECT images. The filter was designed based on the statistics of individual image slices. The quality of the denoised image was investigated using visual

analysis, PSNR, SSIM, IEF and IQI. All the three algorithms were found to be superior to the current methods in literature to which they were compared against.

Physicians identify myocardial defects by visually scanning for relatively decreased tracer content region in the cardiac SPECT image slice. The thesis explored the possibility of extracting pixel intensity based novel features to identify tracer content region in the heart image slice. Features based on image histogram, GLCM, intensity variation, fractal dimension and standard deviation of brightness were identified. The classification problem was approached by the use of a feed forward neural network algorithm with Levenberg-Marquardt optimization. Classification yielded a sensitivity of 98.4%, specificity of 94.7% and accuracy of 97%. The comparison results reveal that the classification using the proposed features aided the physicians to have a more accurate judgement on the cardiac health from the perfusion images.

7.2 Proposals for future work

Some suggestions are listed here as a possible extension of the work addressed in this thesis.

- The proposed features could be extended to rest and stress images to identify the nature of cardiac abnormality.
- Ability of the proposed features in identifying normal and abnormal heart functioning could be analysed by employing more efficient classifiers.

REFERENCES

1. National Institute of Health (2015). *Heart disease and stroke statistics update by the American Heart Association*.
2. WHO (2015). *Cardiovascular diseases (CVDs), Fact sheet*
<http://www.who.int/mediacentre/factsheets/fs317/en/index.html>
3. WHO (2011). *Global status report on non-communicable diseases* Geneva.
4. **Yusuf S. and Pitt B.** (2002) A lifetime of prevention: the case of heart failure. *Circulation*. 106(24). 2997–2998.
5. **Lloyd-Jones DM, Larson MG, Leip EP, et al.** (2002). Lifetime risk for developing congestive heart failure: the Framingham Heart Study. *Circulation*. 106(24). 3068–3072.
6. **Yogender Singh Bansal, Shatrugan Prasad Mandal, Senthil Kumar and Puneet Setia.** (2015). Prevalence of atherosclerotic coronary stenosis in asymptomatic north indian population: a post-mortem coronary angiography study. *Journal of Clinical and Diagnostic Research*. 9. HC01 - HC04.
7. **Reddy K. S.** (2007). India wakes upto the threat of cardiovascular disease, *Journal of the American College of Cardiology*. 50. 1370-1372.

8. **Gupta R.** (2008). Recent trends in Coronary heart disease epidemiology in India. *Indian Heart Journal*. 60(2B). B4-B18.
9. **Dorairaj Prabhakaran, Panniyammakal Jeemon and Ambuj Roy.** (2016). Cardiovascular Diseases in India Current Epidemiology and Future Directions. *Circulation*. April. 1605-1620, DOI: 10.1161/CIRCULATIONAHA.114.008729
10. **Joshi P, Islam S, Pais P, Reddy S, Dorairaj P, Kazmi K, Pandey MR, Haque S, Mendis S, Rangarajan S and Yusuf S.** (2007). Risk factors for early myocardial infarction in South Asians compared with individuals in other countries. *The Journal of the American Medical Association*. 297. 286–294. doi: 10.1001/jama.297.3.286
11. **Xavier D, Pais P, Devereaux PJ, Xie C, Prabhakaran D, Reddy KS, Gupta R, Joshi P, Kerkar P, Thanikachalam S, Haridas KK, Jaison TM, Naik S, Maity AK and Yusuf S.** (2008). CREATE registry investigators. Treatment and outcomes of acute coronary syndromes in India (CREATE): a prospective analysis of registry data. *Lancet*. 371. 1435–1442. doi: 10.1016/S0140-6736(08)60623-6
12. **Harikrishnan S, Leeder S, Huffman M, Jeemon P and Prabhakaran D.** (2014). *A Race against Time: The Challenge of Cardiovascular Disease in Developing Economies*, New Delhi Centre for Chronic Disease Control, 2nd edition, New Delhi.

13. Neo CarDiab Care (2015). *Alarming statistics in India*
<http://neocardiabcare.com/alarming-statistics-india.htm>
14. **Marcelo F. Di Carli, Tal Geva and Ravin Davidoff.** (2016). The Future of Cardiovascular Imaging, American heart association, *Circulation*, 133, 2640-2661, 2016, <https://doi.org/10.1161/CIRCULATIONAHA.116.023511>
15. Encyclopedia Britannica 2006.
16. **K Singh.** (2013). Systolic and Diastolic Ratio and Rate Pressure Product in Anemia. *Indian Journal of Clinical Practice*, 24(6). 521-523.
17. **Ramachandran S Vasam, Martin G Larson, Emelia J Benjamin, Jane C Evans, Craig K Reiss and Daniel Levy.** (1999). Congestive heart failure in subjects with normal versus reduced left ventricular ejection fraction: Prevalence and mortality in a population-based cohort. *Journal of the American College of Cardiology*. 33(7). 1948–1955.
18. **Hemanta Dutta, Soumitra Ghosh and Dibya Jyoti Dutta.** (2015). Left ventricular ejection fraction as a severity indicator of post myocardial infarction depression. *Delhi psychiatry journal*. 18(1). 25-31.
19. **Shah P, Pichler M, Berman D, Singh B and Swan H.** (1980). Left ventricular ejection fraction determined by radionuclide ventriculography in early stages of first

- transmural myocardial infarction. *American Journal of Cardiology*. 45. 542-546.
20. **Jasmin Caluk.** (2011). *Procedural Techniques of Coronary Angiography, Advances in the Diagnosis of Coronary Atherosclerosis*, 95-120 www.intechopen.com.
 21. **Patrick J. Scanlon and David P. Faxon,** (1999). ACC/AHA Guidelines for Coronary Angiography, A Report of the American College of Cardiology/American Heart Association Task Force on Practice Guidelines, *Journal of the American College of Cardiology*. 33(6). 1756-1824.
 22. **Spaulding C., Lefevre T., Funck F., THEbault B., Chauveau M., Ben Hamda K., et al.** (1996). Left radial approach for coronary angiography: results of a prospective study. *Catheterization and Cardiovascular Diagnosis journal*. 39(4). 365-370.
 23. **Hanley PC, Vlietstra RE, Fisher LD and Smith HC.** (1986). Indications for coronary angiography: changes in laboratory practice over a decade. *Mayo Clinic Proceedings*. 61. 248–53.
 24. Image from Mercy angiography centre <http://www.mercyangiography.co.nz/Procedures/Cardiac+Procedures/CORA.html>
 25. **Jamie L. Lohr.** (2009). *Handbook of cardiac anatomy, physiology and devices*, Edited by P. A. Iaizzo, Humana Press Inc., Totowa, NJ.

26. **Vermilion, R.P.** (1997). *Basic physical principles, in Echocardiography in Pediatric Heart Disease*. Mosby-Year Book, St. Louis, MO.
27. Echocardiography- heart images, Maine Heart Centre http://www.mainehealth.org/heart_body.cfm?id=36
28. **Susanna Price.** (2011). *Transthoracic Echocardiography: Normal Two-Dimensional and Doppler Imaging*, D. De Backer et al. (eds.), Hemodynamic Monitoring Using Echocardiography in the Critically III, Springer-Verlag Berlin Heidelberg.
29. **Nandan S. Anavekar and Jae K. Oh.** (2009). Doppler echocardiography: A contemporary review. *Journal of Cardiology*. 54. 347-358.
30. **Shah Urmil.** (2010). Evolution and present status of cardiac imaging. *Gujarat Medical Journal*. 65(2). 17-26.
31. **Filippo Cademartiri and Koen Nieman.** (2005). *Contrast Material Injection Techniques for CT Angiography of the Coronary Arteries, CT of the Heart: Principles and Applications*, Part V of the series Contemporary Cardiology, Humana Press, Inc., Totowa, NJ.
32. **Taylor AJ, Cerqueira M, Hodgson JM, et al.** (2010). ACCF/SCCT/ACR/AHA/ASE/ASNC/NASCI/SCAI/SCMR 2010 appropriate use criteria for cardiac computed tomography. A report of the American College of Cardiology

Foundation Appropriate Use Criteria Task Force, the Society of Cardiovascular Computed Tomography, the American College of Radiology, the American Heart Association, the American Society of Echocardiography, the American Society of Nuclear Cardiology, the North American Society for Cardiovascular Imaging, the Society for Cardiovascular Angiography and Interventions, and the Society for Cardiovascular Magnetic Resonance. *Journal of the American College of Cardiology*, 56. 1864-1894

33. **Nikolaos Alexopoulos, Paolo Raggi and Demosthenes Katritsis.** (2013). Myocardial Perfusion Imaging with Computed Tomography: Can It Be Used in Clinical Practice?, *Hellenic Journal of Cardiology*. 54. 1-4.
34. Medical body scans, <http://fineartamerica.com/featured/1-cardiac-ct-angiography-medical-body-scans.html>
35. Magnetic Resonance Imaging (MRI). (2016). Cardiac (Heart), Radiological Society of North America (RSNA), March, pp-1-9, <http://www.radiologyinfo.org/en/pdf/cardiacmr.pdf>
36. Heart database, Atlas of human cardiac anatomy, University of Minnesota. <http://www.vhlab.umn.edu/atlas/cardiac-mri/4-chamber/>
37. **Celler, A.** (2009). *Nuclear Medicine: SPECT and PET Imaging Principles, in Medical Imaging: Principles, Detectors, and Electronics*. John Wiley & Sons, Inc., Hoboken, NJ, USA.

38. **Elhendy A, Bax JJ and Poldermans D** (2002). Dobutamine stress myocardial perfusion imaging in coronary artery disease. *Journal of Nuclear Medicine*. 43(12). 1634–46.
39. **Kathryn Adamson**. (2009). *Principles of Myocardial SPECT Imaging, Integrating Cardiology for Nuclear Medicine Physicians, A Guide to nuclear medicine physicians part 111*, Springer Berlin Heidelberg.
40. **Oliver Lindner, Herbert Rusche, Michael Schäfers, Otmar Schober and Wolfgang Burcher**. (2007). Myocardial Perfusion SPECT: Current Concepts, *Deutsches Ärzteblatt International* 104(14). 952–958.
41. **Jamshid Maddahi and Rene R. S. Packard**, (2013). Feature in Diagnostic and interventional cardiology, July 26.
42. **Pat Zanzonico**. (2004). Positron Emission Tomography: A Review of Basic Principles, Scanner Design and Performance, and Current Systems, *Seminars in Nuclear Medicine*, XXXIV(2). 87-111.
43. **Marcelo F. Di Carli, Sharmila Dorbala, Jolene Meserve, Georges El Fakhri, Arkadiusz Sitek, and Stephen C. Moore**. (2007). Clinical Myocardial Perfusion PET/CT. *The journal of nuclear medicine*. 48(5). 783-793.
44. **Camici P G and Rimoldi O E** (2009), The clinical value of myocardial blood flow measurement. *The Journal of Nuclear Medicine*. 50(7). 1076-1087.

45. **Germano G, Kavanagh P B and Berman D S.** (1994). An automatic approach to the analysis, quantitation and review of perfusion and function from myocardial perfusion SPECT images. *International Journal of Cardiac Imaging.* 13. 337-346.
46. **Germano G, Kiat H, Kavanagh P B, Moriel M, Mazzanti M, Su H T, Van Train K F and Berman D S** (1995). Automatic quantification of ejection fraction from gated myocardial perfusion SPECT. *Journal of Nuclear Medicine.* 36. 2138-2147.
47. **Faber T L, Cooke C D, Folks R D, Vansant J P, Nichols K J, DePuey E G, Pettigrew R I and Garcia E V.** (1999). Left ventricular function and perfusion from gated SPECT perfusion images: an integrated method. *Journal of Nuclear Medicine.* 40. 650- 659.
48. **Clark A. N. and Beller G. A.** (2005). The present role of nuclear cardiology in clinical practice. *The Quarterly Journal of Nuclear Medicine and Molecular Imaging.* 49(1). 43-58.
49. **Lefteris Livieratos.** (2012). *Basic Principles of SPECT and PET imaging, Radionuclide and hybrid bone imaging,* Springer Berlin Heidelberg.
50. **Berman DS, Kiat H and Maddahi,** (1991). The new 99m.Tc myocardial perfusion imaging agents: 99m-Tc-sestamibi and 99m.Tc-teboroxime. *Circulation.* 84. 17-21.

51. **Ahmed Fathala** (2011). Myocardial Perfusion Scintigraphy: Techniques, Interpretation, Indications and Reporting. *Annals of Saudi Medicine*. 31(6). 625–634.
52. **H. William Strauss, D. Douglas Miller, Mark D. Wittry, Manuel D. Cerqueira, Ernest V. Garcia, Abdulmassi S. Iskandrian, Heinrich R. Schelbert, Frans J. Wackers, Helena R. Balon, Otto Lang, and Josef Machac** (2008). Procedure Guideline for Myocardial Perfusion Imaging 3.3, *Journal of nuclear medicine technology*, 36(3). 155-161.
53. SPECT gamma camera tomography system, Philips healthcare, <http://www.medicalexpo.com/prod/philips-healthcare/product-70721-429297.html>
54. **Todd E. Peterson and Lars R. Furenlid** (2011). SPECT detectors: the Anger Camera and beyond. *Physics in medicine and biology*. 56(17). R145–R182.
55. **Shung, K. Kirk, Smith, Michael B. and Tsui, Benjamin.** (1992). *Principles of Medical Imaging*, Academic Press, USA.
56. **Farr RF and Allisy-Roberts PJ.** (1999). *Physics for Medical Imaging*, Saunders.
57. **Frans J.Th.Wackers, Wendy Bruni and Barry L.Zaret.** (2004). *Nuclear cardiology: the basics*, Humana Press, New Jersey.
58. **A. Lopez, R. Molina, A.K. Katsaggelos and J. Mateos,** (2001). SPECT image reconstruction using compound models,

IEEE International Conference on Acoustics, Speech, and Signal Processing, May 7-11, Salt Lake City, UT, USA.

59. **George Sgounos, Stephen Chiu, Keith S. Pentlow, Linda J. Brewster, Hovanes Kalaigian, Bernard Bald Win, Farhad Daghighian, Martin C. Graham, Steven M. Larson and Radhe Mohan.** (1993). Three-Dimensional Dosimetry for Radio immunotherapy Treatment Planning. *The Journal of Nuclear Medicine*. 34(9). 1595-1601.
60. **P.P.Bruyant.** (2002). Analytic and iterative reconstruction algorithms in SPECT. *Journal of Nuclear Medicine*, 45(10). 1343–1358.
61. **G. L. Zeng,** (2001). Image reconstruction-a tutorial. *Computerized Medical Imaging and Graphics*. 25. 97-103.
62. **S. R. Cherry, J. A. Sorenson, and M. E. Phelps,** (2003). *Physics in Nuclear Medicine*, Saunders, Philadelphia, Pa, USA, 3rd edition.
63. **Todd K. Moon.** (1996). The expectation maximization algorithm. *IEEE signal processing magazine*. November. 47-60.
64. **A. Krol, D.H. Feiglin, W. Lee, V.R. Kunniyur, R.B. Salgado, I.L. Coman, E.D. Lipson, D.A. Karczewski and F.D. Thomas.** (2004). Application of ordered-subsets expectation-maximization (OSEM) algorithm to cone-beam

- SPECT for accelerated 3D reconstruction. *IEEE nuclear science symposium conference*, October 16-22, Rome, Italy.
65. **Huafu Chen, Xu Lei and Dezhong Yao.** (2007). An improved ordered subsets expectation maximization positron emission computerized tomography reconstruction. *Computers in biology and medicine.* 37(12). 1780–1785.
 66. **Richard Gordon,** (1974). A tutorial on art (algebraic reconstruction techniques). *IEEE Transactions on Nuclear Science.* 21(3). 78-93.
 67. **M. W. Groch and W. D. Erwin.** (2000). SPECT in the year 2000: basic principles. *Journal of Nuclear Medicine Technology.* 28(4). 233–244.
 68. American Heart Association (1992). American College of Cardiology and Society of Nuclear Medicine Standardization of cardiac tomographic imaging. 86. 338-339.
 69. **J D Schuijf, L J Shaw, W Wijns, H J Lamb, D Poldermans, A de Roos, E E van der Wall and J J Bax.** (2005). Cardiac imaging in coronary artery disease: differing modalities. *Heart.* 91(8) 1110–1117.
 70. **Hossein Jadvar, H. William Strauss and George M. Segall,** (1999.) SPECT and PET in the Evaluation of Coronary Artery Disease. *Radiographics.* 19. 915-926.
 71. **W Cheng, M Zeng, C Arellano, W Mafori, J Goldin, M Krishnam and S G Ruehm.** (2010). Detection of myocardial

- perfusion abnormalities: standard dual-source coronary computed tomography angiography versus rest/stress technetium-99m single-photo emission CT. *The British Journal of Radiology*. 83(992). 652–660.
72. **Dustin R. Osborne and Derek W. Austin.** (2015). Feasibility and Initial Performance of Simultaneous SPECT-CT Imaging Using a Commercial Multi-Modality Preclinical Imaging System. *International Journal of Molecular Imaging*. Article ID 134768, 11 pages, doi:10.1155/2015/134768
73. **Dave Fornell.** (2015). Managing Dose in PET and SPECT Myocardial Perfusion Imaging, Diagnostic and interventional cardiology, *Feature- April 20*. pp. 1-1.
74. **Robert C. Hendel.** (2012). Interpretation and Reporting of SPECT Myocardial Perfusion Imaging, Handbook of Nuclear Cardiology, Springer London Heidelberg New York, June.
75. **S. C. Kheruka, U. C. Naithani, A. K. Maurya, N. K. Painuly, L. M. Aggarwal and S. Gambhir.** (2011). A study to improve the image quality in low-dose computed tomography (SPECT) using filtration. *Indian Journal of Nuclear Medicine*. 26(1). 14–21.
76. **Jennifer Prekeges,** (2012). *Nuclear Medicine Instrumentation*, Jones & Bartlett Publishers, USA.

77. **Mostafa Analoui, Joseph D. Bronzino and Donald R. Peterson**, (2012). *Medical imaging: principles and practices*, CRC Press, USA.
78. **Monali Panchal**, (2016). Contrast enhancement techniques to improve the quality of medical images. *International Journal of Advance Research and Innovative Ideas in Education*. 2(3). 568-572.
79. **H. Wang and S. Ong**. (1998). Automated extraction of nuclear boundaries. *Proceedings of 2nd International Conference Biomedical Engineering Days*, May 20-22, Istanbul, Turkey.
80. **D. Falk, D. M. Rubin, and T. Marwala**,. (2006). Enhancement of noisy planar nuclear medicine images using mean field annealing. *International Federation for Medical and Biological Engineering proceedings, World congress on medical physics and biomedical engineering*. 4(14). 2415–2418.
81. **H. Rajabi, A. Bitarafan Rajabi, N. Yaghoobi, H. Firouzabad, and F. Rustgou**. (2005). Determination of the optimum filter function for Tc99m-sastamibi myocardial perfusion SPECT imaging. *Indian Journal of Nuclear Medicine*. 20(3). 77–82.
82. **Maria Lyra and Agapi Ploussi**. (2011). Filtering in SPECT Image Reconstruction. *International Journal of Biomedical*

Imaging, Hindawi Publishing Corporation, Article ID 693795, 14 pages, doi:10.1155/2011/693795

83. **S. Webb, A. P. Long, R. J. Ott, M. O. Leach, and M. A. Flower.** (1985). Constrained deconvolution of SPECT liver tomograms by direct digital image restoration. *Medical Physics.* 12(1). 53–58.
84. **M. Mignotte and J. Meunier.** (1999). A comparison of supervised and blind deconvolution techniques applied in SPECT imagery. *Département d'informatique et de recherche opérationnelle (DIOR), Université de Montréal, Montréal, PQ, Canada.* Tech. Rep. April.
85. **Yousif Mohamed Y. Abdallah and Eltayeb Wagiallah.** (2014). Enhancement of Nuclear Medicine Images using Filtering Technique. *International Journal of Science and Research.* 3(8). 916-921.
86. **Frederick L. Datz, Frank V. Gabor, Paul E. Christian, Grant T. Gullberg, Carol E. Menzel, and Kathryn A. Morton.** (1993). The Use of Computer-Assisted Diagnosis in Cardiac Perfusion Nuclear Medicine Studies: A Review (Part 2). *Journal of Digital Imaging.* 6(1). pp 1-15.
87. **Frederick L. Datz, Charles Rosenberg, Frank V. Gabor, Paul E. Christian, Grant T. Gullberg, Raj Ahluwalia, and Kathryn A. Morton.** (1993). The Use of Computer-Assisted Diagnosis in Cardiac Perfusion Nuclear Medicine Studies: A Review (Part 3). *Journal of Digital Imaging.* 6(2). 67-80.

88. **C. Noel Bairey Merz and Dnel S. Berman.** (1997). Imaging Techniques for Coronary Artery Disease: Current Status and Future Directions. *Clinical Cardiology*. 20. 526-532.
89. **Rabinowich M.** (2011). Nuclear imaging: diagnostic nuclear stress test. *The Online Journal of Cardiology, February 21*. <http://sprojects.mmi.mcgill.ca/heart/nuc990626r2.html>.
90. **Magdalena Kostkiewicz.** (2015). Myocardial perfusion imaging in coronary artery disease, Review article – Special issue: *Imaging in Coronary Artery Disease, Cor et vasa*, 57. e446 – e452.
91. **Yusuf S and Pitt B.** (2002). A Lifetime of Prevention: The Case of Heart Failure. *Circulation*. 106. 2997–2998.
92. **Richard J. Merschen, Allyson Wilson and Christina Truluck.** (2011). Non-Invasive Tests and Imaging Modalities: Role in the Management of CCL Patients. *Cath Lab Digest*. 19(5).
93. **Lodwick GS, Turner AHJ, Lusted LB, et al,** (1966). Computer-aided analysis of radiographic images. *Journal of Chronic Diseases*. 19. 485-496.
94. **Fujita H, Katafuchi T, Uehara T and Nishimura T.** (1992). Application of neural network to computer-aided diagnosis of coronary artery disease in myocardial SPECT bull's eye images. *Journal of Nuclear Medicine*. 33. 272–276.

95. **Porenta G, Dorffner G, Kundrat S, Petta P, Duit-Schedlmayer J and Sochor H.** (1994). Automated interpretation of planar thallium-201-dipyridamole stress-redistribution scintigrams using artificial neural networks. *Journal of Nuclear Medicine.* 35. 2041– 2047.
96. **Hamilton D, Riley PJ, Miola UJ and Amro AA.** (1995). A feed forward neural network for classification of bull’s-eye myocardial perfusion images. *European Journal of Nuclear Medicine.* 22. 108–115.
97. **Haddad M, Adlassnig KP, Porenta G.** (1997). Feasibility analysis of a case-based reasoning system for automated detection of coronary heart disease from myocardial scintigrams. *Artificial Intelligence in Medicine.* 9. 61–78.
98. **Garcia EV, Cooke CD, Folks RD, et al,** (2001). Diagnostic performance of an expert system for the interpretation of myocardial perfusion SPECT studies. *Journal of Nuclear Medicine.* 42. 1185- 1191.
99. Non Communicable Diseases Country Profiles (2011). [Internet]. World Health Organization; [cited 2013 Apr 18]. Available from: http://www.who.int/nmh/countries/ind_en.pdf
100. **Shraddha Chauhan and Bani T. Aeri.** (2015). The rising incidence of cardiovascular diseases in India: Assessing its economic impact. *Journal of Preventive Cardiology.* 4(4). 735-740.

101. **Rajeev Gupta, Indu Mohan and Jagat Narula.** (2016). Trends in Coronary Heart Disease Epidemiology in India. *Annals of global health.* 82(2). 307-315.
102. **Bradley J. Erickson and Brian Bartholmai.** (2002). Computer-Aided Detection and Diagnosis at the Start of the Third Millennium. *Journal of Digital Imaging.* 15(2). 59-68.
103. MPI case studies, Spectrum dynamics medical, <http://www.spectrum-dynamics.com/case-studies/mpi/>
104. **L. Koller.** (2011). The evolution of medical imaging technologies: Electric meat and the physicians shifting gaze. *Ea Journal of Medical Humanities and Social Studies of Science and Technology.* 2(3). 1–22.
105. **Shoukat H. Khan.** (2003). SPECT-Myocardial perfusion scintigraphy. *JK Science.* 5(2). 50-57.
106. **Brindis R G, Douglas P S, Hendel R C, Peterson E D, Wolk M J, Allen J M, Patel M R and Raskin I E.** (2005). ACCF/ASNC appropriateness criteria for single photon emission computed tomography myocardial perfusion imaging (SPECT MPI): a report of the American College of Cardiology Foundation Quality Strategic Directions Committee Appropriateness Criteria Working Group and the American Society of Nuclear Cardiology. *Journal of American College of Cardiology.* 46. 1587-1605.

107. **Nedhal A. Al-Saiyd and Sameera M. Talafha.** (2015). Mammographic Image Enhancement Techniques-A Survey, *International Journal of Computer Science and Information Technology & Security*. 5(1). 200-206.
108. **Rafael C. Gonzalez.** (2009). *Digital Image Processing*, Pearson Education India.
109. **R. Garg, B. Mittal and S. Garg.** (2011). Histogram Equalization Techniques for Image Enhancement. *International Journal of Electronics and Communication Technology*, 2(1). 107-111.
110. **Kotkar, Vijay A., and Sanjay S. Gharde.** (2013). Review of various image contrast enhancement techniques. *International Journal of Innovative Research in Science, Engineering and Technology* 2(7). 2786 – 2793.
111. **Haidi Ibrahim and Nicholas Sia Pik Kong** (2007). Brightness Preserving Dynamic Histogram Equalization for Image Contrast Enhancement. *IEEE Transactions on Consumer Electronics*. 53(4). 1752-1758.
112. **D. Sheet, H. Garud, A. Suveer, J. Chatterjee and M. Mahadevappa.** (2010). Brightness Preserving Dynamic Fuzzy Histogram Equalization. *IEEE Transactions on Consumer Electronics*. 56(4). 2475 – 2480.

113. **S. Srinivasan and N. Balram.** (2006). Adaptive Contrast Enhancement Using Local Region Stretching. *Proceedings of ASID '06*, New Delhi, 8-12 October. pp. 152-155.
114. **Sargun and Shashi B. Rana.** (2015). A Review of Medical Image Enhancement Techniques for Image Processing. *International Journal of Current Engineering and Technology.* 5(2). 1282-1286.
115. **S. K. Shome and S. R. K. Vadali.** (2011). Enhancement of Diabetic Retinopathy Imagery Using Contrast Limited Adaptive Histogram Equalization. *International Journal of Computer Science and Information Technologies*, 2(6). 2694-2699.
116. **Hanan Saleh S. Ahmed and Md Jan Nordin.** (2011). Improving Diagnostic Viewing of Medical Images using Enhancement Algorithms. *Journal of Computer Science.* 7(12). 1831-1838.
117. **Edgar F. Arriaga-Garcia, Raul E. Sanchez-Yanez and M. G. Garcia-Hernandez.** (2014). Image enhancement using Bi-Histogram Equalization with adaptive sigmoid functions. *International Conference on Electronics, Communications and Computers*, Mexico, 26-28 February.
118. **C. X. Wang, L. Small, W. E. Snyder, and R. Williams.** (1994). Edge detection in gated cardiac nuclear medicine images. *IEEE 7th Symposium on Computer Based Medical Systems Proceedings*, North Carolina, June 11-12. 28–33.

119. **Hanan Saleh S. Ahmed and Md Jan Nordin.** (2011). Improving Diagnostic Viewing of Medical Images using Enhancement Algorithms. *Journal of Computer Science.* 7(12). 1831-1838.
120. **Gonzalez and Woods.** (2008). *Digital Image Processing,* Third edition, Pearson Prentice Hall, NJ.
121. **J. Serra.** (1988). *Image Analysis and Mathematical Morphology Volume 1 and 2: Theoretical Advances.* New York: Academic Press.
122. **A. Michelson.** (1927). *Studies in Optics.* U. of Chicago Press.
123. **Y. L. Du-Yih Tsai and E. Matsuyama.** (2008). Information entropy measure for evaluation of image quality. *Journal of Digital Imaging.* 21(3). 338–347.
124. **Z. Wang, A. C. Bovik, H. R. Sheikh, and E. P. Simoncelli.** (2004). Image quality assessment: From error visibility to structural similarity *IEEE Transactions on Image Processing,* 13(4). 600-612.
125. **Crete, F., Dolmiere, T., Ladret, P. and Nicolas, M.** (2007). The Blur Effect: Perception and Estimation with a New No-Reference Perceptual Blur Metric. *SPIE Electronic Imaging Symposium Conference on Human Vision and Electronic Imaging,* January, San Jose, United States. EI 6492-16.
126. **Rosie Shier.** (2004). Paired t tests, Statistics tutorial, *Mathematics learning support centre.* 1-3.

127. **Arman Rahmim and Habib Zaidi.** (2008). PET versus SPECT: strengths, limitations and challenges. *Nuclear Medicine Communications*. 29. 193–207.
128. **Andres Santos and Maria J. Ledesma-Carbayo.** (2006). Cardiac imaging, *Wiley Encyclopedia of Biomedical Engineering*. 14, 1-12. DOI: 10.1002/9780471740360.ebs0221
129. **S. Synefia, M. Sotiropoulos, M. Argyrou, M. Bella, I. Floros, A. Valasi and M. Lyra.** (2014). 3D Spect Myocardial Volume Estimation Increases the Reliability of Perfusion Diagnosis. *e-Journal of Science & Technology*. 3 (9). 35-41.
130. **Eric C. Frey, John L. Humm and Michael Ljungberg.** (2012). Accuracy and Precision of Radioactivity Quantification in Nuclear Medicine Images. *Seminars in Nuclear Medicine May*. 42(3). 208–218. doi:10.1053/j.semnuclmed.2011.11.003
131. **G. R. Ayers and J. C. Dainty.** (1988). Iterative blind deconvolution method and its applications. *Optics Letters*. 13(7). 547–549.
132. **R. G. Lane.** (1992). Blind deconvolution of speckle images. *Journal of the Optical Society of America A*. 9(9). 1508–1514.
133. **Mikhno, A., Elsa, D., Angelini, Bing Bai, Laine, A.,F.** (2013). Locally weighted total variation denoising for ringing artifact suppression in pet reconstruction using PSF modeling. *IEEE 10th International Symposium on Biomedical Imaging:*

From Nano to Macro, April 7-11, San Francisco, CA, USA.
1240-1243.

134. **Mignotte M., and Meunier, J.** (2000). Three-dimensional blind deconvolution of SPECT images. *IEEE Transactions on Biomedical Engineering*. 4(2). 274-281.
135. **D. Kundur and D. Hatzinakos.** (1996). Blind image restoration via recursive filtering using deterministic constraints. Proceedings of the *International Conference on Acoustics Speech, and Signal Processing*, Czech Republic, May 7-10. 547–549.
136. **G. Gindi, M. Lee, A. Rangarajan, and I. G. Zubal.** (1993). Bayesian reconstruction of functional images using anatomical information as priors. *IEEE Transactions on Medical Imaging*. 12(4). 670–680.
137. **X. Ouyang, W. H. Wong, V. E. Johnson, X. Hu, and C. T. Chen.** (1994). Incorporation of correlated structural images in PET image reconstruction. *IEEE Transactions on Medical Imaging*. 13(4). 627–640.
138. **Madsen, M.T. and Park, C.H.** (1979). Enhancement of SPECT images by Fourier filtering the projection set. *Journal of Nuclear Science*, vol. 26, pp. 2687-2690.
139. **Levin, A., Weiss, Y., Durand, F. and Freeman W.T.** (2011). Understanding blind deconvolution algorithms. *IEEE*

Transactions on Pattern Analysis and Machine Intelligence
33(12). 2354-2367.

140. **Bioucas-Dias, J.M. and Figueiredo, M.A.T.** (2007). A new TwIST: Two-step iterative shrinkage/thresholding algorithms for image restoration. *IEEE Transactions on Image Processing*. 16. 2992 – 3004.
141. **L. A. Shepp and Y. Vardi.** (1982). Maximum likelihood reconstructions for emission tomography. *IEEE Transactions on Medical Imaging*. MI-1. 113–122.
142. **A. P. Dempster, N. M. Laird, and D. B. Rubin.** (1977). “Maximum likelihood from incomplete data via the EM algorithm,” *J. R. Stat. Soc.* 39, 1–38.
143. **W. H. Richardson.** (1972). Bayesian-based iterative method of image restoration. *Journal of Optical Society of America*. 62. 55–59.
144. **L. B. Lucy.** (1974). An iterative method for the rectification of observed distributions. *The Astronomical Journal*. 79. 745–754.
145. **D. A. Fish, A. M. Brinicombe, E. R. Pike and J. G. Walker.** (1995). Blind deconvolution by means of the Richardson–Lucy algorithm. *Journal of Optical Society of America A*. 12(1). 58-65.

146. **Minu Poullose.** (2013). Literature Survey on Image Deblurring Techniques. *International Journal of Computer Applications Technology and Research.* 2(3). 286 – 288.
147. **Dejee Singh and R. K. Sahu.** (2013). A Survey on Various Image Deblurring Techniques. *International Journal of Advanced Research in Computer and Communication Engineering.* 2(12). 4736-4739.
148. **T. Hebert and R. Leahy.** (1989). A generalized EM algorithm for 3-d bayesian reconstruction from poisson data using gibbs priors. *IEEE Transactions on Medical Imaging.* 8(2). 194 –202.
149. **Gonzalez R C and Woods R E.** (2002). *Digital Image Processing*,Upper Saddle River NJ Prentice-Hall.
150. **S. Chan, R. Khoshabeh, K. Gibson, P. Gill and T. Nguyen.** (2011). An augmented Lagrangian method for total variation video restoration. *IEEE Transactions on Image Processing.* 20(11). 3097-3111.
151. **Strong, D. and Chan, T.** (2003). Edge-preserving and scale-dependent properties of total variation regularization. *Inverse Problems.* 19. S165–S187. doi:10.1088/0266-5611/19/6/059
152. **L. Rudin, S. Osher, and E. Fatemi.** (1992). Nonlinear total variation based noise removal algorithms. *Physics D.* 60(1–4). 259–268.

153. **A. K. Jain.** (1989). *Fundamentals of Digital Image Processing*, Prentice Hall, NJ.
154. **Pierre Gravel, Gilles Beaudoin, and Jacques A. De Guise.** (2004). A Method for Modeling Noise in Medical Images. *IEEE Transactions on Medical Imaging.* 23(10). 1221-1232.
155. **Li L., Kasabov N., Yang J., Yao L. and Jia Z.** (2015). Poisson Image Denoising Based on BLS-GSM Method. *Neural Information Processing. Lecture Notes in Computer Science.* 9492. 513-522.
156. **Yang S and Lee B-U** (2015). Poisson-Gaussian Noise Reduction Using the Hidden Markov Model in Contourlet Domain for Fluorescence Microscopy Images. *PLOS ONE* 10(9): e0136964. doi:10.1371/journal.pone.0136964
157. **P Shanmuga Sundaram and S Padma,** (2009). Role of myocardial perfusion single photon emission computed tomography in pediatric cardiology practice. *Annals of pediatric cardiology.* 2(2). 127-139.
158. **Pizer S. M. and Todd-Pokropek A. E.** (1978). Improvement of scintigrams by computer processing. *Seminars in Nuclear Medicine.* 8 (2). 125–146.
159. **Al Bovik,** (2000). *Handbook of Image and Video Processing*, Academic Press, Orlando, FL.
160. **P. Hannequin and J. Mas.** (2002). Statistical and heuristic image noise extraction (SHINE): a new method for processing

- Poisson noise in scintigraphic images. *Physics in Medicine and Biology*. 47(24). 4329–4344.
161. **D. L. Donoho.** (1995). Denoising and soft-thresholding. *IEEE Transactions on Information Theory*. 41. 613-627.
162. **D. L. Donoho, and I. M. Johnstone.** (1994). Ideal spatial adaptation via wavelet shrinkage. *Biometrika*. 81. 425-455.
163. **Noubari H. A., Fayazi A. and Babapour F.** (2009). Denoising of SPECT images via optimal thresholding by wavelets. *IEEE Annual International Conference Engineering in Medicine and Biology Society*. 3-6 September, Minneapolis, MN. 352 – 355.
164. **Anscombe F. J.** (1948). The transformation of Poisson, binomial and negative binomial data. *Biometrika*. 15. 246-254.
165. **N. Khelifa, K. Hamrouni, and N. Ellouze.** (2005). Scintigraphic image denoising using Fisz transformation and redundant wavelet packets. *Actes du Colloque GRETSI: Traitement du Signal et des Images*, Louvain-la-Neuve, Belgique, September. 663–666.
166. **N. Khelifa, K. Hamruoni, and N. Ellouze.** (2006). Image denoising using wavelets: a powerful tool to overcome some limitations in nuclear imaging. *Proceedings of the 2nd IEEE International Conference on Information and Communication Technologies*, 24-28 April, Damascus, Syria, 1114–1118.

167. **N. Khelifa, Najla Gribaa, Imen Mbazaa, and Kamel Hamruoni.** (2009). A Based BayesianWavelet Thresholding Method to Enhance Nuclear Imaging”, International Journal of Biomedical Imaging, Hindawi Publishing Corporation, Article ID 506120, 10 pages
168. **B. Zhang, J. M. Fadili, and J.-L. Starck.** (2008). Wavelets, ridgelets, and curvelets for Poisson noise removal. *IEEE Transactions on Image Processing.* 17. 1093–1108.
169. **Paul Rodríguez.** (2013). Total Variation Regularization Algorithms for Images Corrupted with Different Noise Models: A Review. *Journal of Electrical and Computer Engineering,* Hindawi Publishing Corporation, Article ID 217021, 18 pages
170. **Lim J. S.** (1990). *Two-Dimensional Signal and Image Processing.* Prentice Hall, Englewood Cliffs, NJ
171. **J. M. Links, R. W. Jeremy, S. M. Dyer, T. L. Frank, and L. C. Becker.** (1990). Wiener filtering improves quantification of regional myocardial perfusion with thallium-201 SPECT. *Journal of Nuclear Medicine.* 31(7). 1230–1236.
172. **Massimo Filippi.** (2015). *Oxford Textbook of Neuroimaging.* Oxford university press, United Kingdom.
173. **P. Fryzlewicz and G.P. Nason.** (2004). A Haar-Fisz algorithm for Poisson intensity estimation. *Journal of Computational and Graphical Statistics.* 13(3). 621-638.

174. **Wang, Z. and Bovik, A. C.** (2002). A Universal Image Quality Index. *IEEE Signal Processing Letter.* 9 (3). 81-84.
175. **K. Dabov, A. Foi, V. Katkownik, and K. Egiazarian.** (2007). Image Denoising by Sparse 3D Transform-Domain Collaborative Filtering. *IEEE Transactions on Image Processing.* 16(8). 2080-2095.
176. **Goldstein and Osher.** (2009). The split Bregman method for L1 regularized problems. *SIAM Journal on Imaging Sciences.* 2(2). 323-343.
177. **Tali Sharir, Guido Germano, Paul B. Kavanagh, Shenhan Lai, Ishac Cohen, Howard C. Lewin, John D. Friedman, Michael J. Zellweger and Daniel S. Berman.** (1999). Incremental Prognostic Value of Post-Stress Left Ventricular Ejection Fraction and Volume by Gated Myocardial Perfusion Single Photon Emission Computed Tomography. *Circulation-American Heart Association*, September 7. 1035-1042.
178. **Lena Johansson, Milan Lomsky, Jens Marving, Mattias Ohlsson, Sven-Eric Svensson and Lars Edenbrandt.** (2011). Diagnostic evaluation of three cardiac software packages using a consecutive group of patients. *EJNMMI Research.* 1(22). 1-7.
179. **M R A Gani, F Nazir, S A Pawiro and D S Soejoko.** (2016). Assessment of cardiac function using myocardial perfusion imaging technique on SPECT with ^{99m}Tc sestamibi. 13th

South-East Asian Congress of Medical Physics, *Journal of Physics: Conference Series* 694. 1-5.

180. **M. Minoves, A. Garcia, J. Magrina, J. Pavia, R. Herranz and J. Setoain**, (1993). Evaluation of Myocardial Perfusion Defects by Means of Bull's Eye Images. *Clinical Cardiology*. 16. 16-22.
181. **Ahmed Fathala**. (2011). Myocardial Perfusion Scintigraphy: Techniques, Interpretation, Indications and Reporting, *Annals of Saudi Medicine*, 31(6). 625–634.
182. **Sheenum Marwaha, Himanshu Monga and Shelza**. (2012). Automatic Diagnosis Systems Using Image Processing: A systematic Study. *International Journal of Computer Science and Information Technology & Security*. 2(2). 388-391.
183. **Emmanuel Itti, Gregory Klein, Jean Rosso, Eva Evangelista, Jean-Luc Monin, Pascal Gueret, Michel Meignan, and Jean-Philippe Thirion**. (2004). Assessment of Myocardial Reperfusion After Myocardial Infarction Using Automatic 3-Dimensional Quantification and Template Matching. *The Journal of Nuclear Medicine*. 45(12). 1981-1988.
184. **Cios K.J., Goodenday L.S., Shah K.K. and Serpen G.** (1996). A novel algorithm for classification of SPECT images of a human heart. *Proceedings of Ninth IEEE Symposium on Computer-Based Medical Systems*, 17-18 June, Ann Arbor, MI, 1-5.

185. **Quinlan J. R.** (1993). *C4.5 Programs for Machine Learning*, Morgan Kaufmann Publishers Inc. San Francisco, CA, USA.
186. **Quinlan J. R.** (1979). Discovering Rules by Induction from Large Collection of Examples, *Knowledge-base systems in the Micro Electronic Age*, Edinburgh University Press.
187. **Lindahl D, Palmer J, Ohlsson M, Peterson C, Lundin A and Edenbrandt L.** (1997). Automated interpretation of myocardial SPECT perfusion images using artificial neural networks. *Journal of Nuclear Medicine*. 38(12). 1870-1875.
188. **Rumelhart D. E. And McClelland J. L.** (1986). *Parallel distributed processing. Vols. 1 and 2* Cambridge. MA: MIT Press; 1986:318-362.
189. **Kurgan L A, Cios K J, Tadeusiewicz R, Ogiela M and Goodenday L.** (2001). Knowledge discovery approach to automated cardiac SPECT diagnosis. *Artificial Intelligence in Medicine*. 23(2). 149-169.
190. **Cunha A G.** (2010). Feature selection using multi-objective evolutionary algorithms: application to cardiac SPECT diagnosis. *Advances in bioinformatics*. 74. 85-92.
191. **Szewczyk P. and Baszun M.** (2011). The learning system by the least squares support vector machine method and its application in medicine. *Journal of telecommunications and information technology*. 3. 109-113.

192. **Rafaie S., Salem A. B. M. and Revett K.** (2012). On the use of SPECT imaging datasets for automated classification of ventricular heart disease. *8th international conference on informatics and systems proceedings*, 14-16 May, Cairo 195-198.
193. **Arsanjani R., Xu Y., Dey D., Fish M., Dorbala S., Hayes S., Berman D., Germano G., and Slomka P.** (2013). Improved accuracy of myocardial perfusion SPECT for the detection of coronary artery disease by utilizing a support vector machines algorithm. *Journal of Nuclear Medicine*. 54(4). 549–555.
194. **Alves R. S., Borges F. D., Campos D. and Tavares J. M. R. S.** (2015). Analysis of gated myocardial perfusion spect images based on computational image registration. *IEEE 4th Portuguese meeting on Bioengineering*, 26-28 February, Porto, 1-2.
195. **Anna Plachcińska, Michał Włodarczyk, Katarzyna Kovacevic-Kuśmierk, Małgorzata Bieńkiewicz, Jarosław Drożdż, Krzysztof Chiżyński, Jarosław D. Kasprzak, Jan Z. Peruga and Jacek Kuśmierk.** (2016). Diagnostic performance of myocardial perfusion single-photon emission computed tomography with attenuation correction, *Kardiologia Polska (Polish heart journal)*. 74(1). pp. 32-39.
196. **Vanessa Go, Mehul R. Bhatt and Robert C. Hendel.** (2004). The Diagnostic and Prognostic Value of ECG-Gated SPECT Myocardial Perfusion Imaging. *The Journal of Nuclear Medicine*. 45(5). 912-921.

197. **Rafael C. Gonzalez, Richard E. Woods and Steven L. Eddins.** (2004). Digital Image Processing Using MATLAB, Pearson Education Ptd. Ltd, Singapore.
198. **Shilpa Kamdi and R.K.Krishna,** (2012). Image Segmentation and Region Growing Algorithm. *International Journal of Computer Technology and Electronics Engineering*. 2(1). 103-107.
199. **Haralick R. M., Shanmugan K., and Dinstein I.** (1973). Textural Features for Image Classification. *IEEE Transactions on Systems, Man, and Cybernetics*. SMC-3. 610-621.
200. **Mallat S.** (1989). Theory for multiresolution signal decomposition: the wavelet representation. *IEEE Transactions on Pattern Analysis and Machine Intelligence*. 11(7). 674-693.
201. **Mandelbrot B. B.** (1997). *Fractals in Scaling and Finance-Discontinuity, Concentration, Risk*, Springer, New York.
202. **Mandelbrot B. B.** (1982). *The Fractal Geometry of Nature*. San Francisco, CA: Freeman.
203. **Ke Deng,** (2009). *Fractal, Encyclopedia of database systems*, Editors: Ling Liu, M. Tamer Özsu, pp. 1168-1169, ISBN: 978-0-387-35544-3 (Print) 978-0-387-39940-9 (Online), 2009, Springer Science-Business Media, LLC (USA).
204. **Rumelhart, David, E. Hinton, Geoffrey E., and Williams, Ronald J.** (1986). Learning representations by back-propagating errors. *Nature*. 323(6088). 533-536.

205. **K. Levenberg.** (1944). A method for the solution of certain problems in least squares. *Quarterly of Applied Mathematics.* 5. 164–168.
206. **D. Marquardt.** (1963). An algorithm for least-squares estimation of nonlinear parameters. *SIAM Journal on Applied Mathematics.* 11(2). 431–441.
207. **McCulloch, W.S. and Pitts, W.H.** (1943). A Logical Calculus of the Ideas Immanent in Nervous Activity. *Bulletin of Mathematical Biophysics.* 5. 115–133.
208. **Hao Yu, Bogdan M. Wilamowski.** (2011). Levenberg–Marquardt Training. *Intelligent systems.* 12(1)-12(16).
209. **Hanley, J, A. and McNeil, B. J.** (1982). The meaning and use of the area under a receiver operating characteristic (ROC) curve. *Radiology.* 143(1). 29-36.
210. **M. H. Zweig., and G. Campbell.** (1993). Receiver – operating characteristic (ROC) plots: a fundamental evaluation tool in clinical medicine. *Clinical Chemistry.* 39(4), 561-577.
211. **Marcin Ciecholewski.** (2011). Support Vector Machine Approach to Cardiac SPECT Diagnosis. *14th International Workshop, IWCIA 2011, Madrid, Spain, May 23-25,* 432-443.

LIST OF PAPERS SUBMITTED ON THE BASIS OF THIS THESIS

I. International Journals

1. **Neethu M. Sasi, Kuruvila Varkey and V. K. Jayasree** (2017) A pixel based approach for classification of cardiac single photon emission computed tomography images. *Signal, image and video processing*, Springer, 11(5). 889-896. DOI 10.1007/s11760-016-1036-9.
2. **Neethu M. Sasi and Jayasree V. K.** (2017) An Adaptive Neighbourhood Structuring Element Based Enhancement Technique for Nuclear Images. *International journal of computer theory and engineering*, 9(1). 62- 68.
3. **Neethu M. Sasi and Jayasree V. K.** (2016) Reduction of Blur in Image by Hybrid De-convolution using Point Spread Function. *International journal of image graphics and signal processing*, 8(6). 21-28.
4. **Neethu M. Sasi and Jayasree V. K.** (2016) De-blurring single photon emission computed tomography images using wavelet decomposition. *ICTACT journal on image and video processing*, 6(3). 1180-1184.

II. International Conferences

1. **Neethu M. Sasi, Geethu M. Sasi and Jayasree V. K.** (2018). Pixel Intensity Based Noise Reduction Method for Single Photon Emission Computed Tomography Images. *4th IEEE Middle East Conference on Biomedical Engineering*, Tunis, Tunisia, March 28-30.
2. **Neethu M. Sasi and Jayasree V. K.** (2016). A Regularized Constrained Least Square De-blurring Method for SPECT Images. *International conference on computational intelligence and informatics*, Hyderabad, May 28-30.

- Published in Springer proceedings: Advances in intelligent systems and computing
3. **Neethu M. Sasi and Jayasree V. K.** (2013). Contrast limited adaptive histogram equalization for the qualitative enhancement of myocardial perfusion images. *International conference on bioinformatics and biomedical engineering*, Beijing, China, Sep 26th-28th.
 - Published in the International journal by scientific research publishing: Engineering

III. National Conference

1. **Neethu M. Sasi and Jayasree V. K.** (2017). Performance comparison of classifiers on cardiac SPECT image data. *National conference on power, control, communication and computing (NPCCC'17)* , Kerala, February 1-3.

CURRICULUM VITAE

1. **Name** : Neethu M.Sasi
2. **Date of birth** : 11-09-1979
3. **Educational qualifications**

1997: Higher Secondary, Kerala State Board with first rank and gold medal

Institution: Govt. Higher Secondary School, Kodungallur

2001: Bachelor of Technology (B. Tech) with distinction.

Institution: University College of Engineering,
Thodupuzha

Specialization: Electronics and Communication

2010: Master of Technology (M. Tech) with first rank and gold medal.

Institution: National Institute of Technology, Calicut

Specialization: Signal Processing

Doctor of Philosophy (Ph. D)

Institution: Model Engineering College

University: Cochin University of Science and Technology

Registration date: 09-01-2013